To the Graduate Council:

I am submitting herewith a dissertation written by Russell Scott Becker entitled "An Investigation of Dissipative Forces Near Macroscopic Media." I recommend that it be accepted in partial fulfillment of the requirements for the degree of Doctor of Philosophy, with a major in Physics.

Rufus H. Ritchie

Rufus H. Ritchie, Major Professor

We have read this dissertation and recommend its acceptance:

T. A. Callcott

Harold C. Schweinler

F. C. Hume

Accepted for the Council:

L. Evans Roth

Vice Chancellor
Graduate Studies and Research

AN INVESTIGATION OF DISSIPATIVE FORCES
NEAR MACROSCOPIC MEDIA

A Dissertation

Presented for the

Doctor of Philosophy

Degree

The University of Tennessee, Knoxville

Russell Scott Becker

August 1982

ACKNOWLEDGMENTS

I would like to acknowledge the assistance of Dr. R. H. Ritchie in providing guidance and expertise in all phases of this project. I am grateful for the advice and contributions of Drs. R. D. Birkhoff and T. A. Callcott during the laboratory phase of the work and of Dr. H. H. Hubbell, without which this work would have met with small success. Appreciation is expressed to Sally Stockstill and Waldean Richardson for their support during the typing phase.

The assistance of the Health and Safety Research Division of ORNL in providing laboratory facilities and the financial support of Oak Ridge Associated Universities through a fellowship during part of this project are gratefully acknowledged. I would also like to acknowledge the use of the computer facilities at The University of Tennessee Computing Center for some of the calculations in this work.

Finally, I would like to mention the contributions from my un- and soon-to-be-lettered colleagues for many stimulating discussions over beverages whose constituents will not be divulged on subjects covering the gamut from physics (only occasionally) to metaphysics to politics and women.

ABSTRACT

The interaction of classical charged particles with the fields they induce in macroscopic dielectric media is investigated. For 10- to 1000-eV electrons, the angular perturbation of the trajectory by the image potential for surface impact parameters of 50 to 100 Å is shown to be of the order of 0.001 rads over a distance of 100 Å. The energy loss incurred by low-energy particles due to collective excitations such as surface plasmons is shown to be observable with a transition probability of 0.01 to 0.001 (Becker, *et al.*, 1981b). The dispersion of real surface plasmon modes in planar and cylindrical geometries is discussed and is derived for pinhole geometry described in terms of a single-sheeted hyperboloid of revolution.

An experimental apparatus for the measurement of collective losses for medium-energy electrons translating close to a dielectric surface is described and discussed. Data showing such losses at electron energies of 500 to 900 eV in silver foils containing many small apertures are presented and shown to be in good agreement with classical stopping power calculations and quantum mechanical calculations carried out in the low-velocity limit. The data and calculations are compared and contrasted with earlier transmission and reflection measurements, and the course of further investigation is discussed.

TABLE OF CONTENTS

LIST OF FIGURES

FIGURE PAGE

I. INTRODUCTION

Historical Background

For more than 50 years, work has been done on the interaction of charged particles and solid surfaces. In 1930, Rudford bombarded crystalline material with slow electrons and observed energy losses of the order of 10 eV that were independent of the incident beam energy and crystal orientation. Further studies were carried out by Ruthmann (1948) using fast electrons (of the order of several tens of keV) transiting thin metal foils which indicated similar low-lying losses that could not be identified with atomic core excitations due to their low energy and large half-widths. In 1951, Bohm and Pines showed that collective excitations of the conduction electrons in a metal could account for some of the experimentally observed low-lying energy losses. They suggested that the conduction electrons could be considered a free electron gas; the conduction electrons would then have a characteristic angular frequency of

$$\omega_p = \sqrt{\frac{4\pi n e^2}{m}}$$

where n is the number density of free charge carriers, e is their charge, m is their effective mass, and ω_p is called the plasma frequency and is generally some 5 to 30 eV/$\hbar$. Ritchie (1957) extended the work of Bohm and Pines by considering the depolarization effects of the boundaries. Ritchie employed linearized Bloch hydrodynamic equations and characterized the response of the dielectric with a momentum-, $\vec{k}$, and frequency-,

ω, dependent function $\tilde{\varepsilon}(\vec{k},\omega)$. Within this formalism, he showed three things for thin films:

1. The probability of losses due to excitation $\hbar\omega_p$ are lowered, compared with that for the same thickness in the bulk.
2. Additional losses occur at $\hbar\omega_p/\sqrt{2}$.
3. The total probability of losses to collective excitations increases compared with the loss probability in the same thickness of bulk material.

Energy losses at the lowered frequency $\omega_p/\sqrt{2}$ were observed by Powell and Swan (1959a and b) in thin films of aluminum and magnesium using reflected electrons of energy 750 to 2000 eV. Similar losses for aluminum films using transmission of fast, 34-keV electrons were obtained by Kunz in 1966. The dielectric response approach of Ritchie was extended (Stern and Ferrell, 1960) to include the effect of nonnormal incidence and oxide surface boundaries. They found that the effect of oxides or other surface contaminants was to decrease the low-lying losses to $\omega_p/\sqrt{1 + \varepsilon_0}$, where ε_0 is the static dielectric constant of the boundary media. This was observed both in reflection (Powell, 1960) and transmission (Kunz, 1966) for thin aluminum films.

In the above treatments and measurements, plasma oscillations in both the bulk and surface modes were stimulated by either reflecting slow electrons from the surfaces of the media or transmitting fast electrons through thin foils of the media. Both classes of measurement probe the plasmon fields from infinity down to the surface, providing little direct information about the effects of the plasmon fields in regions near, but not including, the surface. Ritchie (1972) has shown that the "classical" image force acting on a charged particle translating near a metal surface can be attributed to the excitation and decay of virtual surface plasmons; indeed a simple analysis shows that the electromagnetic fields due to the surface plasmons extend into the vacuum. Consider a dielectric slab characterized by response function $\tilde{\varepsilon}(\omega)$ occupying the lower half-space ($-\infty < x < \infty$, $-\infty < y < \infty$, $z < 0$). Solving Laplace's equation for the fields gives:

$$\Phi_{>} = A(x,y)e^{-kz} \tag{I-1a}$$

$$\Phi_{<} = A'(x,y)e^{+k'z} , \tag{I-1b}$$

with A and A' described as solutions of:

$$\left(\frac{\partial^2}{\partial x^2} + \frac{\partial^2}{\partial y^2} + k^2\right) A(x,y) = 0 \tag{I-2a}$$

$$\left(\frac{\partial^2}{\partial x^2} + \frac{\partial^2}{\partial y^2} + k'^2\right) A'(x,y) = 0 . \tag{I-2b}$$

These are identified as the equations for harmonic oscillators with wavelengths $2\pi/k$ and $2\pi/k'$ for k and k' real, since solutions for non-damped waves are desired. The solutions for the electric potential in and out of the slab are given by:

$$\Phi_{>} = Ae^{i\vec{k}\cdot\vec{\rho}}\, e^{-|\vec{k}|z} \tag{I-3a}$$

$$\Phi_{<} = A'\, e^{i\vec{k}'\cdot\vec{\rho}}\, e^{+|\vec{k}'|z} , \tag{I-3b}$$

where $\vec{\rho}$ is $x\hat{e}_x + y\hat{e}_y$ and $\vec{k}$ is $k_x\hat{e}_x + k_y\hat{e}_y$, with a similar expression for $\vec{k}'$. Applying the boundary conditions for the electric potential and the electric displacement at an interface requires $\vec{k} = \vec{k}'$ and $A = A'$. Continuity of the electric displacement results in

$$\tilde{\varepsilon}(\omega)\ |\vec{k}| \quad = \quad -|\vec{k}| \quad \rightarrow \quad \tilde{\varepsilon}(\omega) \quad = \quad -1 \ . \tag{I-4}$$

This may be taken to be the requirement for surface plasma oscillations; the real part of the dielectric response must be equal to -1. Modeling the slab as a Drude metal, with dielectric response $\tilde{\varepsilon}(\omega) = 1 - \omega_p^{\,2}/\omega^2$, we find that $\omega = \omega_p/\sqrt{2}$, the Ritchie frequency (Ritchie, 1957). Thus it can be seen that the plasmon fields extend a characteristic distance 1/k into the vacuum; for slow electrons this distance is typically 50 to 200 Å.

An attempt to probe the vacuum plasmon field was made using a parabolic nontouching trajectory (Lecante, *et al.*, 1977). The apparatus consisted of a pair of oriented, single-crystal, molybdenum plates, biased to provide a normal electric field causing a beam of 2-keV electrons to follow a parabolic trajectory passing the order of 100 Å above the lower plate. An observed 0.95-eV loss was attributed to excitation of molybdenum surface plasmons by the electrons as they transited the nadir of the parabola. Here the surface plasmon field was probed from infinity to 100 Å from the surface. It has been suggested (Rahman and Maradudin, 1980) that the consequent integration over impact parameter z does not yield much useful information about the plasmon field.

In this work, an attempt to localize the surface impact parameter was made by transmitting medium energy electrons through small, submicron holes in a thin silver foil. The exiting beam was then energy analyzed; losses were observed at 3.5 eV, increasing exponentially with the reciprocal square root of the incident energy in accordance with predictions (Otto, 1967; Becker, *et al.*, 1981b; Ferrell, 1981) and are attributed to the aloof excitation of real surface plasma oscillations on the walls of the holes. Chapter II elucidates the classical conservative and non-conservative interactions between slow electrons and dielectric surfaces in geometries described by semi-infinite slabs, small holes in thin sheets, cylindrical cavities in infinite slabs, and surfaces containing apertures characterized by single-sheeted hyperboloids of revolution. Chapter III describes the experimental apparatus used and the technique employed in measuring the aloof scattering of the electrons, and Chapter IV compares the results of the experimental investigation with the various theoretical calculations of Chapter II.

Scope of Work

The scope of this work is to study the forces acting on a charged particle near macroscopic media. In pursuing this, primary emphasis has been placed on measuring energy losses on slow electrons transiting submicron apertures in silver foils and measuring the plasmon excitation probability for this process as a function of energy. Secondary emphasis has been placed on the theoretical development of the aloof scattering process.

II. ELECTRICAL IMAGE FORCES BETWEEN CHARGES AND SURFACES

In this chapter the dynamic interaction of a charged particle with the conservative and nonconservative components of the image force will be investigated. Section A will treat the conservative interactions for a plane slab, a hole in a thin sheet, and a cylindrical void in perfectly conducting media. Section B will examine the classical nonconservative interaction for a charged particle translating near a dielectric media in plane slab and cylindrical void geometries. Section C develops the surface plasmon dispersion relation for a thick hole described by a hyperboloid of one sheet, and limiting cases are discussed with bearing on transitions and interactions involving the plasmon field.

A. Classical Motion of Charged Particles in Conservative Fields

Plane slab. We consider a charge q with mass m, translating with velocity $\vec{v} = v_x \hat{e}_x$ a distance z above a plane conducting slab. The charge q moves under the influence of the image potential, which for a plane conducting sheet is given by:

$$\Phi(z) = -\frac{q}{4z} . \qquad \text{(II-1)}$$

The equations of motion for x and z components are:

$$\ddot{z} = -\frac{q^2}{4mz^2} \qquad \text{(II-2a)}$$

and

$$\ddot{x} = 0 \, . \tag{II-2b}$$

Equations (II-2a) and (II-2b) can be solved by quadratures giving for the equation of motion:

$$\frac{dx}{dz} = \left(\frac{E_x}{E_z + q^2/4z}\right)^{\frac{1}{2}} , \tag{II-3a}$$

where

$$\begin{aligned} E_x &= \frac{1}{2} m\dot{x}^2 \\ E_z &= \frac{1}{2} m\dot{z}^2 - \frac{q^2}{4z} \end{aligned} \tag{II-3b}$$

at time $t = 0$. Integrating (II-3) gives:

$$\begin{aligned} x - x_o = \left(\frac{E_x}{E_z}\right)^{\frac{1}{2}} \Bigg[& (z^2 + Az)^{\frac{1}{2}} + i \, \frac{A}{2} \sin^{-1} \, (1 + \frac{2z}{A}) \\ & - (z_o{}^2 + Az_o)^{\frac{1}{2}} - i \, \frac{A}{2} \sin^{-1} \, (1 + \frac{2z_o}{A}) \Bigg] , \end{aligned} \tag{II-4}$$

where $A = q^2/4E_z$.

The generalized equation of motion can be specialized to the case of a charge q initially translating parallel to the plane slab

$$x - x_o = \left(\frac{4E_x z_o}{q^2}\right)^{\frac{1}{2}} \left\{ \frac{z_o}{2} \cot^{-1} \left[\frac{1 - z_o/2z}{(z_o/z - 1)^{\frac{1}{2}}} \right] - z(z_o/z - 1)^{\frac{1}{2}} \right\} . \tag{II-5}$$

If z is set to zero, the expression for the range $x - x_o$ traversed by an electron is:

$$x - x_o = \frac{\pi}{2}\left(\frac{4E_x z_o}{\hbar c\alpha}\right)^{1/2} z_o , \tag{II-6}$$

where α is approximately 1/137. For initial energies of 10 eV and impact distances z_o = 50 Å, the range before impact is 925 Å; for 500-eV electrons, a range of about 6500 Å is indicated. It can be seen that for medium energies, path lengths of the order of several thousand angstroms must be traversed in order to produce significant deflection for closely approaching electrons.

Hole in thin sheet. A more realistic and interesting case for this investigation is the motion of a charged particle in the vicinity of a hole in a thin conducting sheet. We consider a point charge q at position x_o, y_o a distance z_o above a thin conducting sheet that contains a hole of radius a. Transforming to toroidal coordinates, we have for x, y, and z in terms of toroidal coordinates η, ξ, and ϕ (Arfkin, 1970, p. 112):

$$x = \frac{a \sinh\eta \cos\phi}{\cosh\eta - \cos\xi}, \quad y = \frac{a \sinh\eta \sin\phi}{\cosh\eta - \cos\xi}, \quad z = \frac{a \sin\xi}{\cosh\eta - \cos\xi}$$

$$\rho = (x^2 + y^2)^{1/2} = \frac{a \sinh\eta}{\cosh\eta - \cos\xi} . \tag{II-7}$$

The Laplacian in this coordinate system is:

$$\nabla^2 = \frac{(\cos\eta - \cos\xi)^3}{a^2 \sinh\eta}\left[\frac{\partial}{\partial\eta}\left(\frac{\sinh\eta}{\cosh\eta - \cos\xi}\frac{\partial}{\partial\eta}\right) + \frac{\partial}{\partial\xi}\left(\frac{\sinh\eta}{\cosh\eta - \cos\xi}\right)\frac{\partial}{\partial\xi}\right]$$

$$+ \frac{(\cosh\eta - \cos\xi)^2}{a^2 \sinh^2\eta}\frac{\partial^2}{\partial^2\phi} \tag{II-8}$$

with scale factors h_ξ, h_η, h_ϕ:

$$h_\xi = h_\eta = \frac{a}{\cosh\eta - \cos\xi}\,, \quad h_\phi = \frac{a \sinh\eta}{\cosh\eta - \cos\xi} = \rho\,. \qquad \text{(II-9)}$$

In physical terms, the ξ coordinate describes a set of spheres on the z-axis with centers at $z = a \cot\xi$ and radii $a \csc\xi$; the η coordinate describes a set of toroids with cross sections described by circles centered a distance $a \coth\eta$ from the z-axis and of minor radius $a\,\mathrm{csch}\eta$. We may assign a direction to the unit vectors $\hat{\xi}$ and $\hat{\eta}$ such that $\hat{\xi}$ projects inward along the radii of the z-axis spheres and $\hat{\eta}$ projects inward along the minor radii of the toroids. Along the z-axis η is zero, and the upper surface of the xy plane is described by $\xi = 0$ for $\rho > a$ and $\xi = \pi$ for $\rho < a$; similarly, the lower surface of the xy plane is described by $\xi = 2\pi$ for $\rho > a$ and $\xi = \pi$ for $\rho < a$ (see Fig. 1). It can be seen that $\hat{\xi}$ is everywhere normal to the xy plane, allowing the surface charge density to be nicely described by:

$$\sigma = \frac{\cosh\eta - \cos\xi}{4\pi a} \left.\frac{\partial\Phi}{\partial\xi}\right|_{\xi=\xi_o} . \qquad \text{(II-10)}$$

For the conducting sheet in the x-y plane, $\cos(\xi_o) = 1$ and

$$\sigma = \frac{\cosh\eta - 1}{4\pi a} \left.\frac{\partial\Phi}{\partial\xi}\right|_{\xi=0} . \qquad \text{(II-11)}$$

If we assume the potential has the form

$$\Phi(\xi,\eta,\phi) = (\cosh\eta - \cos\xi)^{\frac{1}{2}}\, \Phi(\xi,\eta,\phi)\,, \qquad \text{(II-12)}$$

then a reasonable separation of Laplace's equation can be made, giving

ORNL-DWG 81-16048

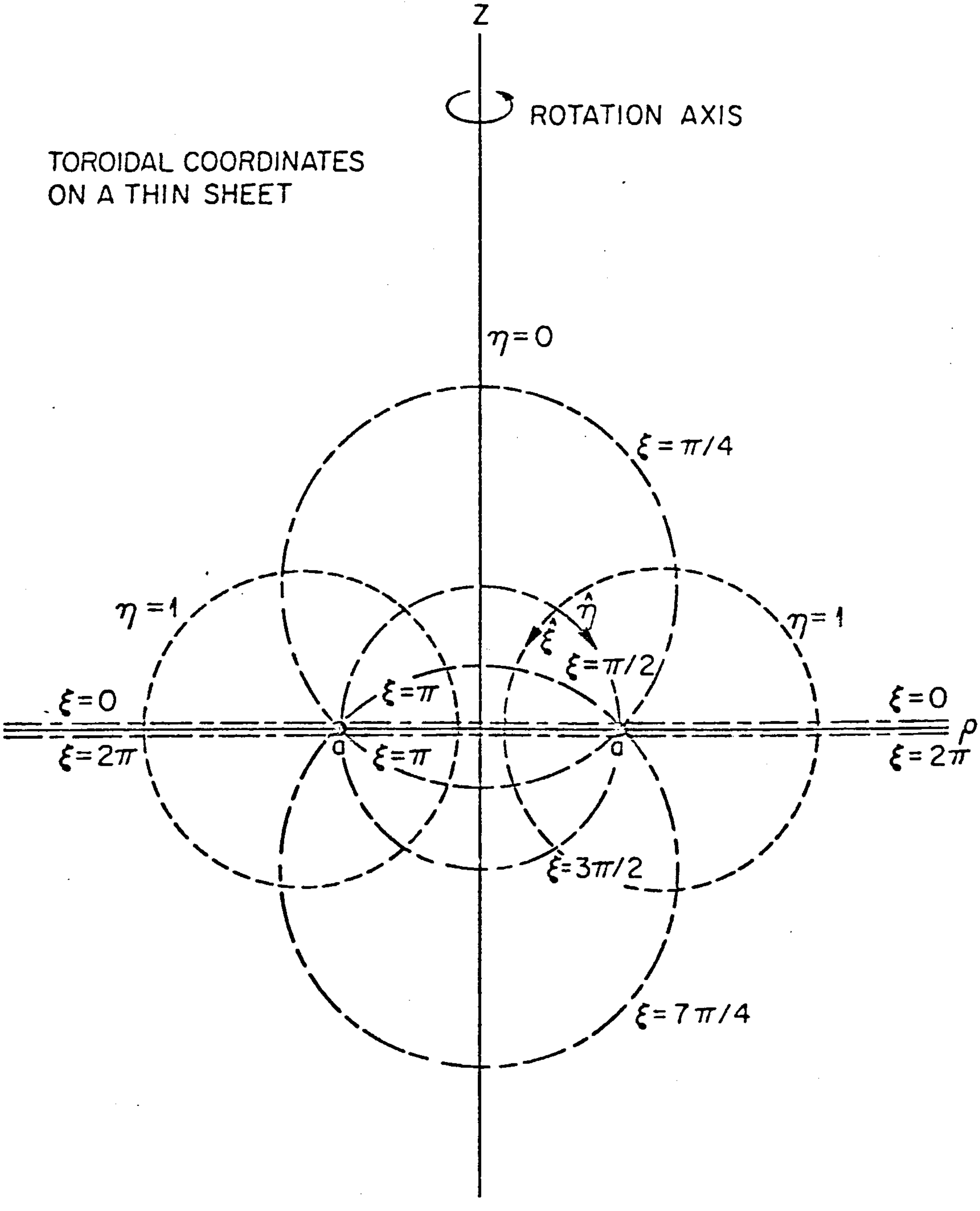

Figure 1. Toroidal Coordinates Describing a Hole in a Thin Sheet. The quantity η describes a torus of major diameter $a\coth\eta$ and minor radius $a\,\mathrm{csch}\,\eta$, co-axial with the z-axis. The quantity ξ describes sets of spheres centered at $z = a\cot\xi$ with radii $a\csc\xi$.

$$\frac{1}{\sinh\eta}\frac{\partial}{\partial\eta}\left(\sinh\eta\frac{\partial\Phi}{\partial\eta}\right)+\frac{\partial^2\Phi}{\partial\xi^2}+\frac{1}{\sinh^2\eta}\frac{\partial^2\Phi}{\partial\phi^2}+\frac{1}{4}\Phi = 0 . \tag{II-13}$$

Employing standard separation of variables, we let $\Phi(\xi,\eta,\phi) = R(\eta)S(\xi)H(\phi)$. Then it is immediately seen that $H(\phi)$ and $S(\xi)$ can be separated in Eq. (II-13) as

$$\frac{1}{S}\frac{d^2S}{d\xi^2} = -n^2 , \qquad S(\xi) = S_n e^{in\xi} \tag{II-14a}$$

$$\frac{1}{H}\frac{d^2H}{d\phi^2} = -m^2 , \qquad H(\phi) = H_m e^{im\phi} \tag{II-14b}$$

where m is an integer, since H is required to be continuous at 0 and 2π. The differential equation for η is then:

$$\frac{1}{\sinh\eta}\frac{d}{d\eta}\left(\sinh\eta\frac{dR}{d\eta}\right)+\left(\frac{1}{4}-n^2-\frac{m^2}{\sinh^2\eta}\right)R = 0 . \tag{II-15}$$

This is Legendre's equation for $\underline{P}_\nu^\mu(x)$ and $Q_\nu^\mu(x)$ with $x = \cosh\eta$, $\nu = -1/2 + n$, and $\mu = m$. These are referred to as toroidal or ring functions (Abramowitz and Stegun, 1970).

$$R(\eta) = A_n^m \underline{P}_{n-\frac{1}{2}}^m (\cosh\eta) + B_n^m Q_{n-\frac{1}{2}}^m (\cosh\eta) . \tag{II-16}$$

The oscillator product functions for the potential can then be written as:

$$\Phi_n^m = \sqrt{\cosh\eta - \cos\xi}\, e^{in\xi} e^{im\phi}\Big[A_n^m \underline{P}_{n-\frac{1}{2}}^m (\cosh\eta) + B_n^m Q_{n-\frac{1}{2}}^m (\cosh\eta)\Big] . \tag{II-17}$$

The potential in the half-space above and below the x-y plane can be described in terms of the generalized surface harmonics as expressed in Eq. (II-17). For the immediate problem of a charged particle q at x_o, y_o, z_o near the hole in the sheet, we require Green's function for toroidal geometry. This can be shown to be (Ferrell, 1978) as:

$$G(\vec{r}:\vec{r}_o) = -\frac{2^{-5/2}}{\pi^2 a}\left[(\cosh\eta - \cos\xi)(\cosh\eta_o - \cos\xi_o)\right]^{\frac{1}{2}}$$

$$\times \left\{ \left[\cosh\alpha - \cos(\xi - \xi_o)\right]^{-\frac{1}{2}} \left[\frac{\pi}{2} + \sin^{-1}\left(\frac{\cos\frac{\xi-\xi_o}{2}}{\cosh\alpha/2}\right)\right] \right.$$

$$\left. - \left[\cosh\alpha - \cos(\xi + \xi_o)\right]^{-\frac{1}{2}} \left[\frac{\pi}{2} + \sin^{-1}\left(\frac{\cos\frac{\xi+\xi_o}{2}}{\cosh\alpha/2}\right)\right] \right\}$$

where $\cosh\alpha = \cosh\eta\,\cosh\eta_o - \sinh\eta\,\sinh\eta_o\,\cos(\phi - \phi_o)$. Denoting D and D' by the following expressions:

$$D^2 = (x - x_o)^2 + (y - y_o)^2 + (z - z_o)^2$$

$$= 2a^2\,\frac{\cosh\alpha - \cos(\xi - \xi_o)}{(\cosh\eta - \cos\xi)(\cosh\eta_o - \cos\xi_o)} \tag{II-19a}$$

$$D'^2 = (x - x_o)^2 + (y - y_o)^2 + (z + z_o)^2$$

$$= 2a^2\,\frac{\cosh\alpha - \cos(\xi + \xi_o)}{(\cosh\eta - \cos\xi)(\cosh\eta_o - \cos\xi_o)}\ ; \tag{II-19b}$$

then at all points in space the electric potential due to the charge q and the induced charge on the sheet is given by:

$$\Phi(\vec{r},\vec{r}_o) = -\frac{q}{4\pi D}\left[\frac{1}{2}+\frac{1}{\pi}\sin^{-1}\left(\frac{\cos\frac{\xi-\xi_o}{2}}{\cosh\alpha/2}\right)\right] + \frac{q}{4\pi D'}\left[\frac{1}{2}+\frac{1}{\pi}\sin^{-1}\left(\frac{\cos\frac{\xi+\xi_o}{2}}{\cosh\alpha/2}\right)\right]. \qquad \text{(II-20)}$$

It may be noted that the potential can be separated into contributions from the charge in the first term and its image in the second term. Evaluating the homogeneous portion of Eq. (II-20) at the position of the charge q, (x_o, y_o, z_o) and multiplying by $-q/2$ gives the potential energy for the interaction between the conducting sheet and the test charge. For this Ferrell finds:

$$W(\xi_o,\eta_o,\phi_o) = -\frac{q^2}{4\pi a}\frac{\cosh\eta_o - \cos\xi_o}{\sin\xi_o}(\sin\xi_o - \xi_o + \pi) \qquad \text{(II-21)}$$

and using relations (II-7) for z gives:

$$W(z,\xi) = -\frac{q^2}{4\pi z}(\sin\xi - \xi + \pi) , \qquad \text{(II-22a)}$$

where

$$\cos\xi = \frac{r^2 - a^2 + z^2}{\{[z^2 + (a+r)^2][z^2 + (a-r)^2]\}^{\frac{1}{2}}} \qquad \text{(II-22b)}$$

$$\sin\xi = \frac{2za}{\{[z^2 + (a+r)^2][z^2 + (a-r)^2]\}^{\frac{1}{2}}} \qquad \text{(II-22c)}$$

and $r^2 = x^2 + y^2$.

Note that for very large values of z (z >> a), $\sin(\xi)$ is approximately ξ and the interaction energy is $-q^2/4z$, the planar image energy;

at large distances from the hole its influence is negligible; this same relation holds if $r \gg a$. Equipotentials for the hole in the thin sheet are shown in Fig. 2 in units of the system scaling factor, $q^2/4a$.

The forces acting on the charge q can be calculated by taking the gradient of the potential energy. Doing so and converting to cylindrical coordinates (r, ϕ, z) gives for the r and z components:

$$F_r = -\frac{q^2 ra}{\pi A^4}\left(1 - \frac{z^2 + r^2 - a^2}{A^2}\right) \qquad \text{(II-23a)}$$

$$F_z = -\frac{q^2}{2\pi z^2}\left[\frac{2z^3 a(z^2 + a^2 + r^2)}{A^6} - \frac{az(z^2 + a^2 + r^2)}{A^4} + \tan^{-1}\left(\frac{2az}{A^2 - r^2 + a^2 - z^2}\right)\right] \qquad \text{(II-23b)}$$

where $A^4 = [z^2 + (a+r)^2][z^2 + (a-r)^2]$.

As z approaches zero, it can be shown that the last two terms cancel each other and the first term vanishes; therefore F_z vanishes for $r < a$.

To illustrate the strength of the image force, Eqs. (II-23a) and (II-23b) were used for holes of diameters 1000 and 10,000 Å in a perfect conductor. Monte Carlo calculations for electrons of low to medium energies projected normal to the sheet were carried out by numerically integrating the equations of motion from a starting point ten hole diameters in front of the sheet to ten hole diameters beyond the sheet. The distribution of final electron trajectories for energies of 10, 100, and 1000 eV on a 1000 Å hole is shown in Fig. 3 and of 10 and 1000-eV

ORNL-DWG 80-14690

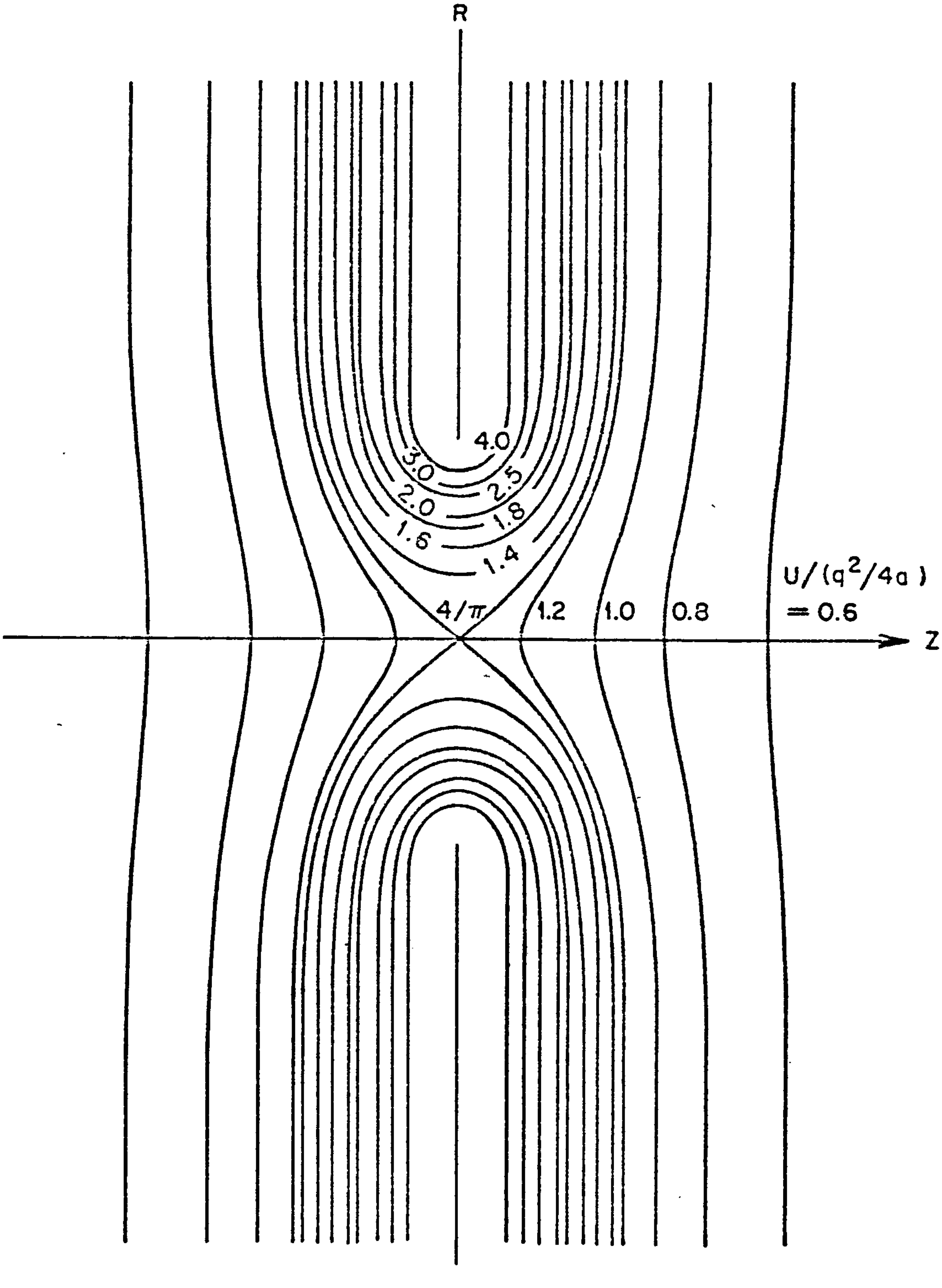

Figure 2. Equipotentials for the Image Energy for a Hole in a Thin Sheet in Units of the Scaling Parameter $q^2/4a$.

ORNL-DWG 81-16049

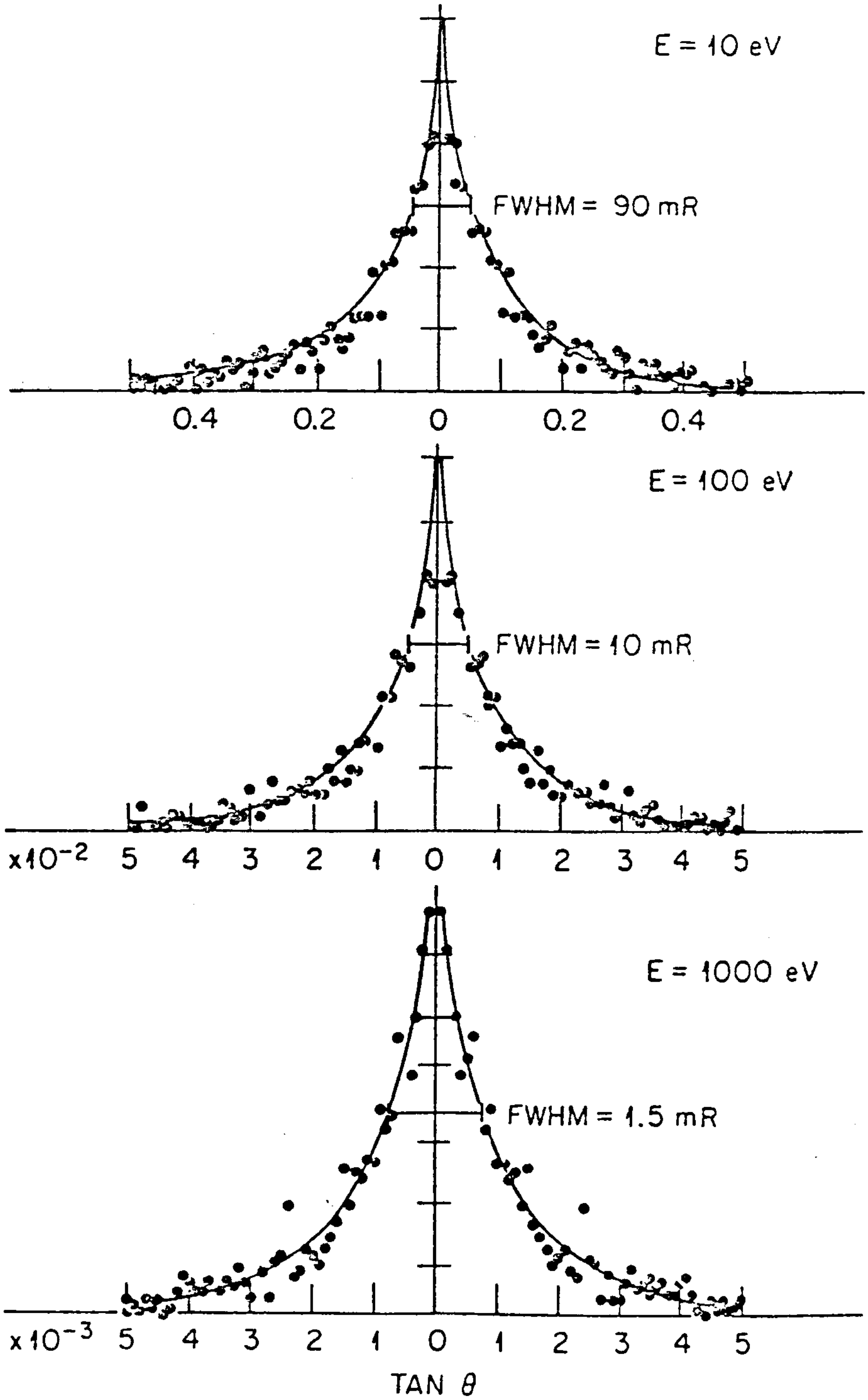

Figure 3. Monte Carlo Calculations of the Scattered Distribution of Electrons Projected Normally on a 1000 Å Thin Hole with Energies of 10, 100, and 1000 eV.

electrons on a 10,000 Å hole in Fig. 4. The deflection is seen to be small, of the order of 100 μrad to 100 mrad full widths at half maximum.

<u>Conservative forces on a charge in a cylindrical void</u>. Finally, we consider the geometry of the cylindrical void. A charge q is at r_o, ϕ_o, z_o in an infinite cylindrical void surrounded by a perfect conductor. As this problem has been previously treated (Becker, *et al.*, 1980), only pertinent aspects of the derivation will be given.

The Green's function for a point charge in an infinitely long, cylindrical cavity in a conductor is given by Smythe (1968) as:

$$\Phi(\vec{r},\vec{r}_o) = \frac{2q}{a^2} \sum_{n=0}^{\infty} \sum_{\ell=1}^{\infty} (2 - \delta_n^o) e^{in(\phi-\phi_o)} e^{-k_{n\ell}|z-z_o|} \frac{J_n(k_{n_\ell} r) J_n(k_{n_\ell} r_o)}{k_{n\ell} J_{n+1}^2 (k_{n\ell} a)} ; \tag{II-24}$$

the charge q is located at $\vec{r}_0 = (r_o, \phi_o, z_o)$, and the field point $\vec{r} = (r, \phi, z)$. The quantity $k_{n\ell}$ is such that the Bessel functions of the first kind satisfy $J_n(k_{n\ell} a) = 0$, a being the radius of the cylinder. The expression for $\Phi(\vec{r},\vec{r}_o)$ gives the electric potential at $\vec{r}$ due to the charge at $\vec{r}_o$ and the induced charges on the cylinder walls. The derived image potential will be the homogeneous portion of $\Phi(\vec{r},\vec{r}_o)$ evaluated at $\vec{r}_o$.

The inhomogeneous portion of the potential is given by:

$$\Phi_{inhomo} = \frac{q}{|r - r_o|} = \frac{q}{(r^2 + r_o^2 + z^2 - 2rr_o \cos\phi)^{\frac{1}{2}}} , \tag{II-25}$$

ORNL-DWG 81-16050

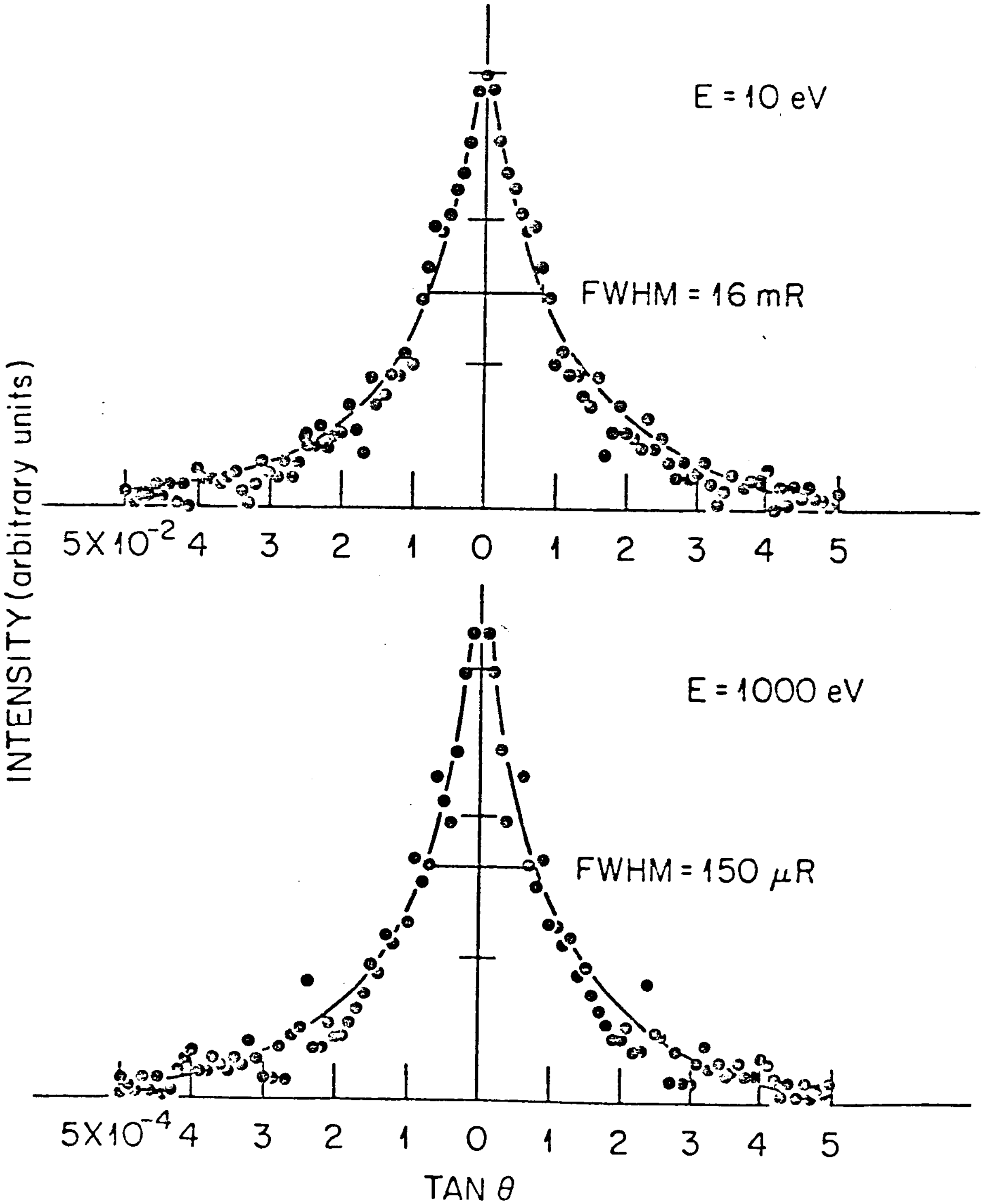

Figure 4. Monte Carlo Calculations of the Scattered Distribution of Electrons Projected Normally on a 1.0-μ Thin Hole with Energies of 10 and 1000 eV.

where z_o and ϕ_o have been set to zero with no loss of generality. Expanding Eq. (II-25) as (Morse and Feschbach, 1953):

$$(r^2 + r_o^2 + z^2 - 2rr_o \cos\phi)^{-\frac{1}{2}} = \sum_{n=0}^{\infty} (2 - \delta_n^0) \cos n\phi \times \int_o^{\infty} dk\, e^{-k|z|} J_n(kr) J_n(kr_o) \; ; \tag{II-26}$$

and using the identity (Buchholz, 1947):

$$\frac{J_n(kr_o)}{J_n(ka)} = -\frac{2}{a} \sum_{a=1}^{\infty} \frac{k_{n\ell}}{k^2 - k_{n\ell}^2} \frac{J_n(k_{n\ell} r_o)}{J_{n+1}(k_{n\ell} a)} \tag{II-27}$$

gives for the homogeneous potential:

$$\Phi_{homo} = \frac{2q}{a^2} = \sum_{n=0}^{\infty} \sum_{\ell=1}^{\infty} (2 - \delta_n^o) \frac{J_n(k_{n\ell} r_o)}{k_{n\ell} J_{n+1}(k_{n\ell} a)} \cos n\phi \; f_{n\ell} \; , \tag{II-28}$$

where

$$f_{n\ell} = \frac{e^{-k_{n\ell}|z|}}{J_{n+1}(k_{n\ell} a)} - k_{n\ell}^2 a \int_o^{\infty} \frac{dk}{k^2 - k_{n\ell}^2} \; e^{-k|z|} \; J_n(ka) J_n(kr) . \tag{II-29}$$

Using various Bessel function identities and noting that $W(r) = 1/2 \int \rho \Phi_o d\tau$ where $\rho(r') = q\delta(\vec{r} - \vec{r}_o)$ gives for the interaction image energy:

$$W(r) = -\frac{q^2}{a} \sum_{n=0}^{\infty} \sum_{\ell=1}^{\infty} (2 - \delta_n^o) \frac{J_n(k_{n\ell} r)}{J_{n+1}(k_{n\ell} a)} \int_o^{\infty} \frac{dk}{k + k_{n\ell}} \times J_n(kr) \; J_n(ka) \tag{II-30}$$

which simplifies to

$$W_o = -\frac{q^2}{a}\sum_{\ell=1}^{\infty}\frac{\int_0^{\infty}\frac{dk}{k+k_\ell}J_o(ka)}{J_1(k_\ell a)} \qquad \text{(II-31)}$$

on the z-axis.

A plot of (II-30) is shown in Fig. 5 along with the planar image potential energy and an approximate expression (Yu, 1978) with all energies normalized to zero at $r = 0$. The dots correspond to the cylinder image energy calculated using relaxation methods.

B. Classical Motion of Charged Particles in Nonconservative Fields

In this section the motion and frictional energy losses for a charged particle translating in the vicinity of media characterized by a frequency dependent dielectric response $\tilde{\varepsilon}(\omega)$ will be discussed. The first part will treat motion above and parallel to a planar slab; the second part will discuss paraxial motion in a cylindrical void surrounded by dielectric media.

Planar slab. The geometry of Eq. (II-1) is utilized; a charge q is moving with velocity v a distance z above a planar slab characterized by dielectric response $\tilde{\varepsilon}(\omega)$ occupying the lower half-space (Fig. 6). v is parallel to the surface and in the x direction. The charge density at time t is given by:

$$\rho(\vec{r},t) = q\delta(x - vt)\delta(y - y_o)\delta(z - z_o) \ . \qquad \text{(II-32)}$$

The following calculation invokes classical electrodynamics and is valid for frequency regimes where the media may be characterized by its

ORNL-DWG 79-14233

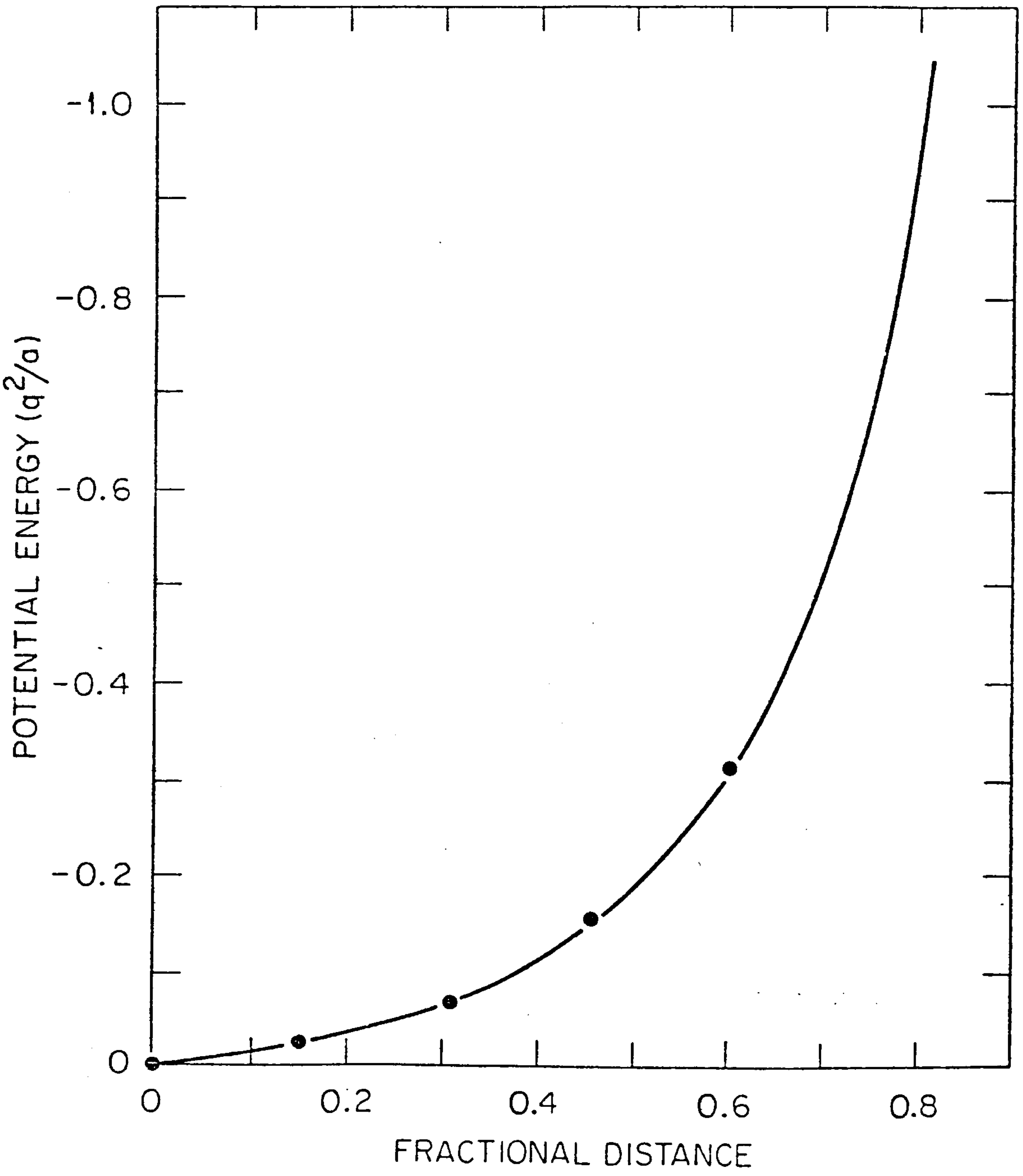

Figure 5. Cylinder Image Potential Energy. The cylinder image potential energy as a function of radius is shown in units of q^2/a. The dots indicate the potential as calculated by relaxation methods, while the solid line shows the results of calculation with Eq. (II-30).

ORNL-DWG 81-11647

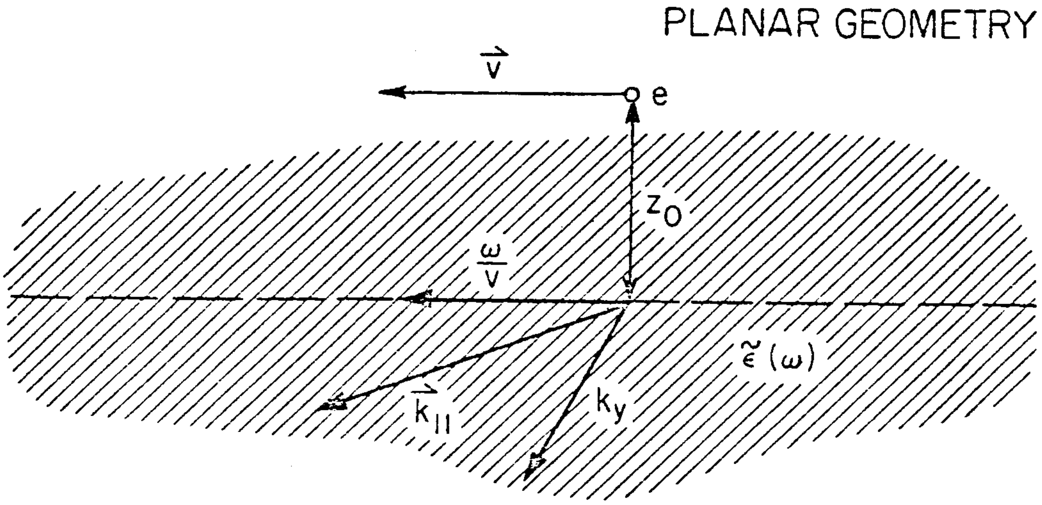

Figure 6. Diagram of the Image Interaction in Planar Geometry Showing the Impact Parameter z_o, the Electron Velocity $\vec{v}$, and the Components of the Surface Momentum, $\vec{k}_{\parallel} = \omega/v\ \hat{e}_x + k_y \hat{e}_y$.

optical response. The time interval during which the fields due to the translating charge are strongly felt by the metal surface are of the order of z/v. Optical periods are $\sim 10^{-15}$ seconds, and typical metal relaxation times are of the order of $\sim 10^{-16}$ to 10^{-18} seconds; for 100-eV electrons an impact parameter z of 60 Å produces an optical driving field. For a metal, the relaxation time is sufficiently short so as to produce the effect of a static charge distribution translating over the planar surface in step with the charge q.

Inside the metal, $z < 0$, the electric potential is described by:

$$\nabla^2 \Phi_< (\vec{r},t) = 0 \tag{II-33a}$$

and outside

$$\nabla^2 \Phi_> (\vec{r},t) = -4\pi\rho = -4\pi q \delta(y - y_o)\delta(z - z_o)\delta(x - vt) \; . \tag{II-33b}$$

These equations can be solved simply by taking the Fourier transform over the x and y coordinates, giving:

$$\left(\frac{d^2}{dz^2} - k_\parallel^2\right)\tilde{\Phi}_> = 0 \tag{II-34a}$$

$$\left(\frac{d^2}{dz^2} - k_\parallel^2\right)\tilde{\Phi}_> = -8\pi^2 q \; \delta(z - z_o) \; \delta(\omega - k_x v) \tag{II-34b}$$

where $k^2 = k_x^2 + k_y^2$, and $\tilde{\Phi}_{\lessgtr}$ denotes the transformed potential.

The general solutions for the transformed potentials are:

$$\tilde{\Phi}_< = Ae^{k_\parallel z} \; , \qquad z < 0 \tag{II-35a}$$

$$\tilde{\Phi}_{>} = \frac{4\pi^2 q}{k_{\parallel}} \delta(\omega - k_x v)\, e^{-k_{\parallel}|z-z_o|} + Be^{-k_{\parallel}z}, \quad z > 0 \, . \tag{II-35b}$$

The first term in Eq. (II-35b) is the inhomogeneous Coulomb field due to the charge q at (x - vt, y_o, z_o), and the second term is the homogeneous induced field. The usual boundary conditions requiring continuity of the electric potential and normal component of the electric displacement are applied at the interface, z = 0. The coefficients A and B are found to be:

$$A = \frac{8\pi^2 q\, \delta(\omega - k_x v)}{k_{\parallel}(1 + \tilde{\varepsilon})} e^{-k_{\parallel}z_o} \tag{II-36a}$$

$$B = \frac{4\pi^2 q}{k_{\parallel}} \delta(\omega - k_x v) \left(\frac{1 - \tilde{\varepsilon}}{1 + \tilde{\varepsilon}}\right) e^{-k_{\parallel}z_o} \, . \tag{II-36b}$$

Classical charges cannot interact with themselves (they have already done so through the work done in assembly). The interaction energy between the charge and the slab is due to the homogeneous potential given by:

$$\tilde{\Phi}_{>} = \frac{4\pi^2 q}{k} \delta(\omega - k_x v) \left(\frac{1 - \tilde{\varepsilon}}{1 + \tilde{\varepsilon}}\right) e^{-k_{\parallel}(z+z_o)} \tag{II-37}$$

evaluated at the position of the charge.

$$W_{int} = \frac{1}{2}\int \rho(\vec{r})\, \Phi_{o>}(\vec{r})\, d\tau = \frac{1}{2} q\, \Phi_{o>}(\vec{r}_o)\big|_{x=vt,\; y-y_o,\; z=z_o} \tag{II-38}$$

where $\Phi_{o>}$ is derived through the inverse Fourier transform

$$\Phi_{o>} = \frac{1}{2\pi}^{3} \int_{-\infty}^{+\infty} dk_x \int_{-\infty}^{+\infty} dk_y \int_{-\infty}^{-\infty} d\omega \; e^{i(k_x x + k_y y - \omega t)} \; \tilde{\Phi}_{o>}(k_{\parallel}, \omega, z) . \qquad \text{(II-39)}$$

The classical energy of interaction is then:

$$W = \frac{q^2}{4\pi} \int_{-\infty}^{+\infty} dk_y \int_{-\infty}^{+\infty} dk_x \int_{-\infty}^{+\infty} d\omega \; e^{i(k_x x + k_y y - \omega t)}$$

$$\times \; \delta(\omega - k_x v) \left(\frac{1 - \tilde{\varepsilon}}{1 + \tilde{\varepsilon}} \right) \frac{e^{-2k_{\parallel} z_o}}{k_{\parallel}} \qquad \text{(II-40)}$$

which reduces upon integration over k_x to:

$$W = \frac{q^2}{2\pi v} \int_{-\infty}^{+\infty} dk_y \int_{o}^{+\infty} d\omega \; \frac{e^{-2z\sqrt{k_y^2 + \frac{\omega^2}{v^2}}}}{\sqrt{k_y^2 + \frac{\omega^2}{v^2}}} \; \mathrm{Re} \left(\frac{1 - \tilde{\varepsilon}}{1 + \tilde{\varepsilon}} \right) . \qquad \text{(II-41)}$$

The integration over k_y can be done immediately, giving:

$$W = \frac{q^2}{\pi v} \int_{o}^{+\infty} d\omega \; K_o \left(\frac{2z\omega}{v} \right) \mathrm{Re} \left(\frac{1 - \tilde{\varepsilon}}{1 + \tilde{\varepsilon}} \right) , \qquad \text{(II-42)}$$

ignoring for the moment the existence of a maximum propagation momentum, k_{cutoff}, in the dielectric response.

Several interesting features can be obtained from (Eq. II-42). First, frequency ω_s, where $\varepsilon_1 = -1$ and ε_2 is small but finite, will produce large contributions to the classical image interaction. It is of no surprise that this condition, $\varepsilon_1 = -1$, is the general requirement for the existence of surface plasma oscillations--the classical image force can be expressed quantum mechanically in terms of the surface plasmon field (Ritchie, 1972). Second, since the dielectric response function $\tilde{\varepsilon}(\omega)$ has the property that $\tilde{\varepsilon}(-\omega) = \tilde{\varepsilon}^*(\omega)$ (Ziman, 1972), only the real part of the integrand in Eq. (II-42) contributes to the conservative interaction energy. Third, the contribution to the image energy is small for large values of ω since the asymptotic form of the $K_o(x)$ modified Bessel function is $e^{-x}/x^{\frac{1}{2}}$, where ω/v may be thought of as the planar wave vector k coupling to excitation $E = \hbar\omega$ at particle velocity v--the phase velocity of the response is matched to the horizontal component of the electron's velocity. Fourth, the strength of the interaction is also damped exponentially in z; the particle must be a distance of the order of v/ω from the slab to experience much coupling at energy $\hbar\omega$, a requirement outlined in the opening discussion.

We can consider the dielectric to consist of electrons tied to equilibrium positions by springs (a Lorentz solid). Fourier analysis of such a classical oscillator yields (Ehrenreich, 1965):

$$\tilde{\varepsilon}(\omega) = 1 - \frac{\omega_p^2}{\omega^2 + i\omega\gamma - \omega_o^2}, \tag{II-43}$$

where ω is the driving frequency, γ the damping of the oscillations, ω_p the classical plasma frequency, and ω_o the free period of the oscillators. For a metal, $\omega_o = 0$, the electrons are considered a free electron gas, and Eq. (II-43) becomes the Drude simple metal:

$$\tilde{\varepsilon}(\omega) = 1 - \frac{\omega_p^2}{\omega(\omega + i\gamma)}. \tag{II-44}$$

For a perfect conductor $\omega_p \to \infty$, $\varepsilon \to -\infty$. Introducing this into (II-42) and integrating over ω gives

$$W = \frac{q^2}{4z} , \tag{II-45}$$

the classical planar image potential energy.

Going back to (II-41), the Drude dielectric response for $\tilde{\varepsilon}(\omega)$, Eq. (II-44), can be used. This gives for the real and imaginary parts of $(1 - \tilde{\varepsilon})/(1 + \tilde{\varepsilon})$

$$\mathrm{Re}\left(\frac{1 - \tilde{\varepsilon}}{1 + \tilde{\varepsilon}}\right) = \frac{\omega_p^2 (\omega^2 - \omega_p^2)}{(\omega^2 - \omega_p^2)^2 + \gamma^2\omega^2} \tag{II-46a}$$

$$\mathrm{Im}\left(\frac{1 - \tilde{\varepsilon}}{1 + \tilde{\varepsilon}}\right) = - \frac{\omega_p^2 \gamma\omega}{(\omega^2 - \omega_p^2)^2 + \gamma^2\omega^2} . \tag{II-46b}$$

Using Eq. (II-46a) and observing that the contribution to the conservative interaction energy is identical for $-\infty < \omega <= 0$ as for $0 <= < \infty$, we find for the energy of interaction:

$$W = \frac{q^2}{4z} + \frac{q^2v^2}{16\omega_p^2 z^3}\left(1 - \frac{\gamma^2}{\omega_p^2}\right) + \frac{9q^2v^4}{32\omega_p^4 z_o^3} + \cdots ; \tag{II-47}$$

and employing a cutoff wave vector,

$$W = \frac{q^2}{4z}\left(1 - e^{-2k_c z}\right) + \frac{q^2v^2}{16\omega_p^2 z^3}\left(1 - \frac{\gamma^2}{\omega_p^2}\right) \left[1 - e^{-2k_c z}(2z^2k_c^2 + 2zk_c + 1)\right] + \ldots \tag{II-48}$$

Examining (II-47), it can be seen that the primary effect of the finite response time, $1/\omega_p$, of the metal is to increase slightly the attractive force of the image potential. The additional interaction is primarily that of a dipole, is proportional to the electron energy, and is inversely proportional to the square of the plasma frequency (the more the dielectric behaves like a perfect conductor, the less the deviation from the ideal image force). The rationale for imposing a finite cutoff momentum is as follows: the phase velocity v_p of the plasma oscillations is given by ω_p/k_p; as k_p increases the phase velocity drops down to v_{fermi}, the velocity of electrons in the top of the conduction band, at which point it is somewhat facetious to speak of a collective propagation as opposed to single particle trajectories, and the plasma oscillation breaks up.

Equation (II-48) shows the effect of invoking a maximum plasmon momentum. As the quantity $zk_c = z\omega_p/v_{fermi}$, decreases to zero, the term $1 - e^{-2zk_c}$ decreases the strength of the image interaction. As z approaches zero, a case not strictly valid for this analysis, the image interaction converges to $W = 1/2\ q^2 k_c \approx \alpha/2\ E_p\ (v_F/c)^{-1}$.

Of more interest are the frictional losses due to the motion of a charge above the planar slab. The classical stopping power is given by:

$$-\frac{dw}{dx} = -q\vec{E}_x\hat{x} = +q\left.\frac{\partial\Phi_{o>}}{\partial x}\right|_{z=z_o,y=y_o,x=vt} . \qquad \text{(II-49)}$$

Using the properties of the Fourier transform, this gives for the x component of the induced electric field

$$\frac{\partial \Phi_{o>}}{\partial x} = \frac{iq}{2\pi} \int_{-\infty}^{+\infty} dk_x \int_{-\infty}^{\infty} dk_y \int_{-\infty}^{\infty} d\omega \, e^{i(k_x x + k_y y - \omega t)} \, k_x \delta(\omega - k_x v) \tag{II-50}$$

$$\times \left(\frac{1 - \tilde{\varepsilon}}{1 + \tilde{\varepsilon}}\right) \frac{e^{-2k_{\parallel} z}}{k_{\parallel}} .$$

Due to the presence of the additional factor of k_x in the integrand, only the imaginary part of the integrand contributes to the stopping power. For the stopping power, after integrating over k_x:

$$\frac{dW}{dx} = \frac{q^2}{2\pi v^2} \int_{-\infty}^{+\infty} dk_y \int_{-\infty}^{+\infty} d\omega \, \omega \, \frac{e^{-2z\sqrt{k_y^2 + \frac{\omega^2}{v^2}}}}{\sqrt{k_y^2 + \frac{\omega^2}{v^2}}} \, \mathrm{Im}\left(\frac{1 - \tilde{\varepsilon}}{1 - \tilde{\varepsilon}}\right) . \tag{II-51}$$

As on (II-42), this can be integrated immediately, giving:

$$\frac{dW}{dx} = \frac{2q^2}{\pi v^2} \int_{o}^{\infty} d\omega \, \omega \, K_o \, \frac{2z\omega}{v} \, \mathrm{Im}\left(\frac{1 - \tilde{\varepsilon}}{1 + \tilde{\varepsilon}}\right) . \tag{II-52}$$

This expression shares similar features with Eq. (II-42). Again, it is noted that the maximum contribution to the integrand from the dielectric response is at $\varepsilon_1 = -1$ and ε_2 small, classic hallmarks of a strong surface plasmon resonance. As in the case of the image interaction energy (II-42), it can be seen that the stopping power is damped exponentially with impact parameter z and for increasing frequency ω.

With a suitable change of variables and the use of the imaginary part of the Drude response function (II-46b), Eq. (II-51) can be integrated analytically, giving:

$$\frac{dW}{dx} = \frac{q^2 \gamma v}{4\omega_p^2 z^3} + \frac{9q^2 \gamma v^3}{8\omega_p^4 z^5} \left(1 - \frac{\gamma^2}{\omega_p^2}\right) + \ldots \tag{II-53a}$$

For comparison, the stopping power in the limit $v >> z\ \omega_p$ is given by (Ritchie, 1981):

$$\frac{dW}{dx} = \frac{q^2 \omega_p^2}{v^2} K_o \left(\frac{2\omega_p z}{v}\right) . \tag{II-53b}$$

Using a cutoff wave vector, k_c, in (II-51) gives a stopping power of:

$$\frac{dW}{dx} = \frac{q^2 \gamma v}{4\omega_p^2 z^3} \left[1 - e^{-2k_c z} \left(2k_c^2 z^2 + 2k_c z + 1\right)\right] + \ldots \tag{II-54}$$

The energy losses due to classical oulomb fields are proportional to the square root of the electron energy and to the internal plasmon damping as well as being inversely proportional to the cube of the impact parameter z, a dipole interaction. The damping frequency γ can be thought of as a restriction on the ability of the translating static charge distribution to relax; it lags the ground point of the translating charge somewhat and to this extent resembles a tidal friction.

If we let $\omega_p \to \infty$, the metal becomes a perfect conductor; then the imaginary part of $(1 - \tilde{\varepsilon})/(1 + \tilde{\varepsilon})$ becomes zero in (II-46b), and there is no frictional force. This can also be seen by letting $\omega_p \to \infty$ in Eqs. (II-53a and b) and (II-54).

It is of interest to note that the above treatment for a classical dielectric may be extended to include a momentum dependent dielectric response which takes into account interactions due to electron-hole excitations as well as interactions due to collective motions (Ferrell, *et al.*, 1979). The expression for the imaginary part of $(1 - \tilde{\varepsilon})/(1 + \tilde{\varepsilon})$ in (II-51) is replaced by:

$$\mathrm{Im}\left(\frac{1 - \tilde{\varepsilon}}{1 + \tilde{\varepsilon}}\right) \geq -\mathrm{Im}\left(\frac{1 - I}{1 + I}\right) , \tag{II-55}$$

where

$$I(\omega) = \frac{k_{\parallel}}{\pi} \int_{-\infty}^{+\infty} \frac{dk_z}{k^2 \tilde{\varepsilon}(\vec{k},\omega)} \tag{II-56}$$

and

$$\vec{k} = \vec{k}_{\parallel} + \vec{k}_z = k_y \hat{e}_y + \frac{\omega}{v} \hat{e}_x + k_z \hat{e}_z .$$

$I(\omega)$ is termed the surface dielectric response. Using for $\tilde{\varepsilon}(\vec{k},\omega)$ a hydrodynamical dielectric response,

$$\tilde{\varepsilon}(\vec{k},\omega) = 1 + \frac{\omega_p^2}{k^2 \frac{v_f^2}{3} \left[1 - i\pi H\ (2k_f - k)/2kv_f\right] - \omega(\omega + i\gamma)} \tag{II-57}$$

where

$$H(x) = \frac{1}{2}\left[1 + \frac{x}{|x|}\right],$$

the stopping power is found to break into two parts upon expansion in ω:

$$\left.\frac{dW}{dx}\right|_{\substack{\text{electron}\\ \text{hole}}} \cong \frac{(qe)^2 m^2 v_f^4 v}{\pi h^3 \omega_p^4} \frac{\ln\left(1.1966 \frac{\omega_p z}{v_f}\right)}{z^4} \tag{II-58a}$$

and

$$\left.\frac{dW}{dx}\right|_{\substack{\text{surface}\\ \text{plasmon}}} \cong \frac{q^2 \gamma v}{4\omega_p^2 z^3} \; . \qquad \text{(II-58b)}$$

The contribution due to collective excitations is identical to (II-53) in the asymptotic limit of $z \gg v/\omega_p$. The contributions due to electron-hole excitations (single-particle) are also proportional to the square root of the incident energy but are damped more strongly in z than (II-58b) and are dominated by the collective effects for large values of the impact parameter z. Single particle contributions to the long-range stopping power vary as $(v_f/z\omega_p)^4$; for a good conductor Fermi energies are a few eV, and values of ω_p are in the optical range or short UV; hence the characteristic distance, z_c, where single-particle excitations begin to dominate collective excitations is about 1-10 Å.

Charge moving paraxially in a cylindrical void. In this section we utilize the geometry of Eq. (II-24), that of a charge q translating with velocity v paraxially in a cylindrical void of radius a surrounded by a dielectric medium characterized by response function $\tilde{\varepsilon}(\omega)$ (Fig. 7). The standard method of solution is followed; low velocities $v \ll c$ are considered, and impact parameters $z_c = a - r_o$ are kept sufficiently large to satisfy the noncirculation conditions of Eq. (II-32), namely, a/v is much greater than the relaxation time of the dielectric, of the order of $\sim 10^{-18}$ s for a good conductor.

Solving for the electrostatic potential inside and outside the cylinder gives:

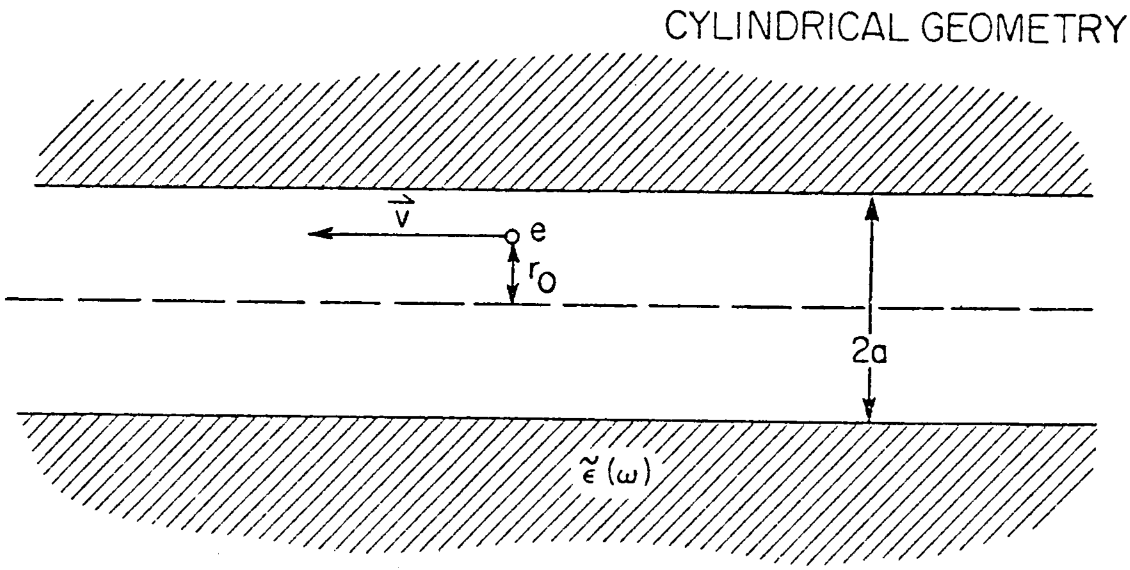

Figure 7. Diagram of the Image Interaction in Cylindrical Geometry Showing the Impact Radius r_o and the Electron Velocity $\vec{v}$. The diameter of the cylinder is taken as 2a.

$$\nabla^2\Phi_<(\vec{r},t) = -4\pi\rho(\vec{r}) = -\frac{4\pi q}{r}\,\delta(r - r_o)\,\delta(\phi - \phi_o)\,\delta(z - vt) \qquad \text{(II-59a)}$$

and

$$\nabla^2\Phi_>(\vec{r},t) = 0\ , \qquad \text{(II-59b)}$$

where the solutions $\Phi_<$ and $\Phi_>$ are subject to the usual requirements for the continuity of the potential at the boundaries and continuity of the normal component of the displacement field. We use Fourier transforms on the ϕ, z, and t coordinates of the expressions for $\Phi_{\substack{<\\>}}$ as

$$\Phi_{\substack{<\\>}}(\vec{r},t) = \left(\frac{1}{2\pi}\right) \sum_{m=0}^{\infty} e^{im(\phi-\phi_o)} \int_{-\infty}^{+\infty} d\omega \int_{-\infty}^{+\infty} dk\; e^{i(kz-\omega t)} \times \tilde{\Phi}^m_{\substack{<\\>}}(r,k,\omega) \qquad \text{(II-60)}$$

where the delta function in ϕ is expanded as $\delta(\phi - \phi_o) = 1/2\pi \sum_m e^{im(\phi-\phi_o)}$. With no loss of generality, the angle ϕ_o can be set to zero. The transformed potentials then satisfy:

$$\left[\frac{1}{r}\frac{d}{dr}\left(r\frac{d}{dr}\right) - \left(\frac{m^2}{r^2} + k^2\right)\right]\tilde{\Phi}^m_< = \frac{4\pi q}{r}\,\delta(r - r_o)\,\delta(\omega - kv) \qquad \text{(II-61a)}$$

and

$$\left[\frac{1}{r}\frac{d}{dr}\left(r\frac{d}{dr}\right) - \left(\frac{m^2}{r^2} + k^2\right)\right]\tilde{\Phi}^m_> = 0\ . \qquad \text{(II-61b)}$$

The homogeneous equations in (II-61a) and (II-61b) are seen to be satisfied by the modified Bessel functions of integer order $I_m(kr)$ and

$K_m(kr)$. The $I_m(kr)$ are bounded at $r = 0$ and divergent as $r \to \infty$, while the $K_m(kr)$ are bounded at infinity and unbounded as r approaches zero. The interior solutions are thus expanded in terms of the I_m and the exterior solutions in terms of the K_m.

A complete solution for the interior inhomogeneous Eq. (II-61b) can be expressed as:

$$\begin{aligned} {}^{m}\Phi^{m}_{<p} &= - I_m(kr) \int d(kr) \frac{4\pi q}{r} \delta(r - r_o)\delta(\omega - kv) \frac{K_m(kr)}{W(I_m,K_m)} \\ &\quad + K_m(kr) \int d(kr) \frac{4\pi q}{r} \delta(r - r_o)\delta(\omega - kv) \frac{I_m(kr)}{W(I_m,K_m)} \end{aligned} \qquad \text{(II-62)}$$

where

$$W(I_m,K_m) = I_m(kr)K_m{}'(kr) - I_m{}'(kr)K_m(kr) = \frac{1}{kr}$$

is the Wronskian for the modified Bessel functions. The complete solutions interior and exterior to the cylinder can be written as:

$$\tilde{\Phi}^{m}_{<} = A_m I_m(kr) - 4\pi q\ \delta(\omega - kv)\ I_m(kr\overset{<}{:}r_o)\ K_m(kr\overset{>}{:}r_o) \qquad \text{(II-63a)}$$

and

$$\tilde{\Phi}^{m}_{>} = B_m K_m(kr) \qquad \text{(II-63b)}$$

where the symbol $r\overset{<}{:}r_o$ denotes the lesser of r and r_o, and $r\overset{>}{:}r_o$ denotes the greater of r and r_o, and the coefficients A_m and B_m are to be determined.

Applying the boundary conditions on the interior and exterior potentials and solving for A_m and B_m gives:

$$A_m = \frac{4\pi q\ \delta(\omega - kv)(\tilde{\varepsilon} - 1)\ I_m(kr_o)\ K_m(ka)\ K_m'(ka)}{(\tilde{\varepsilon} - 1)\ I_m(ka)\ K_m'(ka) - 1/ka} \tag{II-64}$$

$$B_m = \frac{4\pi q}{ka} \frac{\delta(\omega - kv)\ I_m(kr_o)}{(\tilde{\varepsilon} - 1) I_m(ka)\ K_m'(ka) - 1/ka}\ . \tag{II-65}$$

The complete solution for the transformed potential is then given by:

$$\tilde{\Phi}^m_< = \frac{4\pi q\ \delta(\omega - kv)\ (\tilde{\varepsilon} - 1)\ I_m(kr_o)\ I_m(kr)\ K_m(ka)\ K_m'(ka)}{(\tilde{\varepsilon} - 1)\ I_m(ka)\ K_m'(ka) - 1/ka} - 4\pi q\ \delta(\omega - kv)\ I_m(kr \overset{<}{:} r_o)\ K_m(kr \overset{>}{:} r_o) \tag{II-66a}$$

$$\tilde{\Phi}^m_> = \frac{4\pi q}{ka} \frac{\delta(\omega - kv)\ I_m(kr_o)\ K_m(kr)}{(\tilde{\varepsilon} - 1)\ I_m(ka)\ K_m'(ka) - 1/ka}\ . \tag{II-66b}$$

The first term in Eq. (II-66a) is the homogeneous portion of the interior transform potential, while the second term is the inhomogeneous interior transform potential for a point charge q located at (r_o, k, ω) in transform space. The classical interaction energy between the dielectric and the slab is derived from the homogeneous potential. Using the inverse Fourier transform and evaluating the potential at $\phi = \phi_o = 0$, this is:

$$W = \frac{q}{2} \left(\frac{1}{2\pi}\right)^2 \sum_{m=o}^{\infty} \int_{-\infty}^{+\infty} dk \int_{-\infty}^{+\infty} d\omega\ e^{i(kz - \omega t)}\ \tilde{\Phi}^m_{<o}\ (r_o, k, \omega)\ . \tag{II-67}$$

Noting the properties of the dielectric response [viz. $\tilde{\varepsilon}(-\omega) = \tilde{\varepsilon}^*(\omega)$], as before, only the real part of $\tilde{\Phi}^m_{o<}$ contributes to the classical energy of interaction. Making use of $\delta(\omega - kv)$ gives:

$$W = \frac{q^2}{2\pi^2 a} \sum_m \int_o^\infty dk' \, \mathrm{Re} \left[\frac{(\tilde{\varepsilon} - 1) \, I_m^2\left(k' \frac{r_o}{a}\right) K_m(k') \, K_m'(k')}{(\tilde{\varepsilon} - 1) \, I_m(k') \, K_m'(k') - 1/k'} \right] \qquad \text{(II-68)}$$

where the argument of dielectric response $\tilde{\varepsilon}$ is $\omega = k'v/a$. Letting $r = 0$, to place the charge on the axis, gives for the minimum interaction energy:

$$W_{axis} = \frac{q^2}{2\pi^2 a} \int_o^\infty dk' \, \mathrm{Re} \left[\frac{k' \, (\tilde{\varepsilon} - 1) \, K_o(k') \, K_1(k')}{k' \, (\tilde{\varepsilon} - 1) \, I_o(k') \, K_1(k') + 1} \right] . \qquad \text{(II-69)}$$

It is of interest to consider the case of a perfect conductor and compare this result to Eq. (II-31). In this limit of $\omega_p \to \infty$ we have:

$$W\Big|_{\omega_p \to \infty} = \frac{q^2}{2\pi^2 a} \sum_{m=0}^{\infty} \int_o^\infty dk' \, \mathrm{Re} \left[\frac{I_m^2\left(k' \frac{r_o}{a}\right) K_m(k')}{I_m(k')} \right] \qquad \text{(II-70)}$$

and axially

$$W_{axis}\Big|_{\omega_p \to \infty} = \frac{q^2}{2\pi^2 a} \int_o^\infty dk' \, \frac{K_o(k')}{I_o(k')} . \qquad \text{(II-71)}$$

For small values of r/a, Eqs. (II-70) and (II-71) are much easier to evaluate than (II-30) and (II-31).

In a fashion similar to Eq. (II-32), the dielectric media can be considered a Drude metal with response specified by Eq. (II-44). Dividing up $\tilde{\varepsilon}(\omega)$ into $\varepsilon_1 + i\varepsilon_2$, the real component of the integral in

(II-68) is

$$W = \frac{q^2}{2\pi^2 a} \sum_m \int_0^\infty dk'\; k' I_m^2\left(k' \frac{r_o}{a}\right) K_m(k')\; K_m'(k') \qquad \text{(II-72)}$$

$$\times \frac{\left[k' I_m(k')\; K_m'(k') + \dfrac{\omega^2}{\omega_p^2}\right]}{\left[k'(I_m(k')\; K_m'(k') + \dfrac{\omega^2}{\omega_p^2}\right]^2 + \dfrac{\omega^2 \gamma^2}{\omega_p^4}} ,$$

where

$$[\tilde{\varepsilon}(\omega) - 1]^{-1} = -\frac{\omega^2}{\omega_p^2} - i\,\frac{\omega\gamma}{\omega_p^2} .$$

In terms of the rescaled momentum k', the frequency ω can be expressed as $\omega = k'v/a$. The generalized expression for the image energy is:

$$W = \frac{q^2}{2\pi^2 a} \sum_m \int_0^\infty dk'\; I_m^2\left(k' \frac{r_o}{a}\right) K_m(k')\; K_m'(k') \qquad \text{(II-73)}$$

$$\times \frac{\left[I_m(k')\; K_m'(k') + k' \dfrac{v^2}{a^2 \omega_p^2}\right]}{\left[I_m(k')\; K_m'(k') + k' \dfrac{v^2}{a^2\omega_p^2}\right]^2 + \dfrac{v^2\gamma^2}{a^2\omega_p^4}} .$$

For large values of k', $I_m(k')K_m'(k')$ become $-1/2k'$ and $I_m^2(k'\, r_o/a)$ $K_m(k')K_m'(k')$ becomes $a/4k'^2 r_o\; e^{-2(k'/a)z_c}$. For low velocities and good conductivity ($\gamma << \omega_p$), the integral in (II-73) can be expressed as:

$$\underset{\text{asymptotic}}{\overset{k' \gg 1}{\sim}} \quad \frac{v^2}{4r_o a\omega_p^2} \; \frac{e^{-2k'(z_c/a)}}{k'} \left(1 + \frac{a^2\omega_p^2}{2k'^2 v^2}\right)$$

which is damped exponentially in $k'(z_c = a - r_o)$. Since the response is exponentially damped and proportional to v^2 where $v \ll c$, the contribution in the asymptotic regime can be neglected. For very small arguments, the integral in Eq. (II-73) expands as:

$$\underset{k' \ll 1}{\sim} \quad -\ln k' \; 1 + \left(1 - \frac{\gamma^2}{\omega_p^2}\right) \frac{v^2}{a^2\omega_p^2} \; k'^2 + \ldots$$

$$+ \sum_m \frac{m}{2} \left(\frac{r_o}{a}\right)^{2m} \left[1 + 2\, \frac{v^2}{a^2\omega_p^2} \left(1 - 2\, \frac{\gamma^2}{\omega_p^2}\right) k'^2 + \ldots\right.$$

retaining only terms through k'^2 and $(v/a\omega_p)^2$. This can be compared to the small argument expansion of (II-70):

$$-\ln k' + \sum_{m=o}^{\infty} \frac{m}{2} \left(\frac{r_o}{a}\right)^{2m} .$$

It can be seen that the effect of finite conductivity is to slightly increase the image energy by a factor proportional to the energy of the incident charged particle, exactly the same as for the plane slab. Indeed, the cylindrical walls can be considered planar for impact parameters where z_c is much less than the cylinder radius a.

Of interest in the present work is the aloof stopping power of the cylindrical void. This is given classically by:

$$\frac{dW}{dz} = q\vec{E}\cdot\hat{z} = -q \left.\frac{\partial \Phi_{o<}}{\partial z}\right|_{z=vt,\, r=r_o,\, \phi=o} \tag{II-74}$$

where

$$\frac{\partial \Phi_{o<}}{\partial z} = (1/2\pi)^2 \sum_{m=o}^{\infty} \int_{-\infty}^{+\infty} dk(ik)e^{i(kz-\omega t)} \tilde{\Phi}^m_{<o}(r_o k,\omega) \; . \qquad \text{(II-75)}$$

Using the properties of the dielectric response, it can be shown that, as in the case of the slab, the real parts of the integrand make a net nonzero contribution. The additional factor of ik makes this the imaginary component of $\tilde{\Phi}^m_{<o}$. This yields:

$$\frac{dW}{dz} = -\frac{2q^2}{\pi^2 a^2} \sum_m \int_o^{\infty} dk' \; \mathrm{Im}\left[\frac{k'^2(\tilde{\varepsilon}-1)I_m^2\left(k'\frac{r_o}{a}\right)K_m(k')K_m'(k')}{k'(\tilde{\varepsilon}-1)I_m(k')K_m'(k') - 1}\right] . \qquad \text{(II-76)}$$

Using a Drude model for the dielectric as given by Eq. (II-44) gives a stopping power of

$$\frac{dW}{dz} = -\frac{2q^2 v\gamma}{\pi\omega_p^2 a^3} \sum_m \int_o^{\infty} dk' \; \frac{k'^2 I_m^2\left(k'\frac{r_o}{a}\right) K_m(k')K_m'(k')}{D_R^2 + D_I^2} \qquad \text{(II-77)}$$

where D_R and D_I are given by

$$D_R = k'I_m(k')K_m'(k') - \frac{k'^2 v^2}{a^2\omega_p^2} \qquad \text{(II-78a)}$$

$$D_I = \frac{k'v\gamma}{a\omega_p^2} \qquad \text{(II-78b)}$$

and

$$D_R^{\,2} + D_I^{\,2} = k'^2 \left\{ I_m^{\,2}(k')\, K_m'^{\,2}(k') + \frac{v^2}{a^2\omega_p^{\,2}} \left[\frac{k'^2 v^2}{a^2\omega_p^{\,2}} - 2k' I_m(k')\, K_m'(k') + \frac{\gamma^2}{\omega_p^{\,2}} \right] \right\} . \qquad \text{(II-78c)}$$

For small values of $v/a\omega_p$, the stopping power can be expressed as

$$\left.\frac{dW}{dz}\right|_{r_o} (v \ll a\omega_p) = -\frac{2q^2 v\gamma}{\pi\omega_p^{\,2} a^3} \sum_m \int_o^\infty dk' \, \frac{k' I_m^{\,2}\left(k'\frac{r_o}{a}\right) K_m(k')}{I_m^{\,2}(k') K_m'(k')} \qquad \text{(II-79a)}$$

and axially

$$\left.\frac{dW}{dz}\right|_{axis} (v \ll a\omega_p) = \frac{2q^2 v\gamma}{\pi\omega_p^{\,2} a^3} \int_o^\infty dk' \, \frac{k' \; K_o(k')}{I_o^{\,2}(k') K_1(k')} \qquad \text{(II-79b)}$$

It can be seen, as in the expression (II-77), that the stopping power varies with the square root of the incident energy, is proportional to the plasmon damping γ, and varies with the inverse cube of the radius, indicating a primarily dipole interaction. The definite integral in Eq. (II-79b) can be integrated numerically, with a result of 0.92; hence, to first order in the expansion in powers of $(v/a\omega_p)^2$, the stopping power for a cylinder is about twice that of a plane slab. This is not surprising since there is much more dielectric in close proximity to the charge q in the cylindrical geometry than in the planar geometry. For a 1-eV electron translating 500 Å over a silver sheet ($\hbar\gamma = 0.15$ eV, $\hbar\omega_p = 3.77$ eV), the long-range stopping power is found to be about

5×10^{-10} eV per angstrom; a 1-eV electron would have to traverse about 2 cm in order to lose 10% of its energy. At closer approaches (50 Å) and higher energies (100 eV), we find the stopping power to be about 5×10^{-6} eV per angstrom; a 100-eV electron must travel about 70 μ before losing energy of the order of 4 eV. It is shown by evaluation of the term $2q^2 v\gamma/\pi\omega_p^2 a^3$ that the classical energy loss for low to medium energy electrons is very small for a good conductor. For 1-eV electrons with 500 Å surface impact parameter, the discriminating quantity $v/a\omega_p$ is about 0.002; and for 100-eV electrons with 50 Å surface impact parameter, $v/a\omega_p$ is about 0.2. This evaluation shows that a surface impact parameter of 50 Å is the limit the classical nonretarded calculations can be pushed for electrons of the order of a few hundred electron volts in energy.

C. Dispersion Relation for Plasmons on a Sheet with a Thick Hole

The previous sections of this chapter have dealt with a classical treatment of the interactions of charged particles with conducting and dielectric surfaces. Geometries considered have included planar slabs, thin conducting sheets containing circular holes, and cylindrical voids in conducting and dielectric media. In this section the nature of surface charge oscillations for circular holes in thick sheets will be discussed.

It is of some interest to summarize surface plasmon dispersion relations for the various geometries considered and to compare and contrast them. For the case of a planar slab of thickness a, the non-retarded surface plasmon dispersion relation for surface wave vector $k_{\parallel}$ is given by (Ritchie, 1957):

$$\frac{\omega^2}{\omega_p^2} = \frac{1}{2}\left(1 \pm e^{-|\vec{k}_{\parallel}|a}\right) ; \qquad \text{(II-80)}$$

and for the case of a finite speed of light, c, the retarded dispersion relation is given by (Ritchie and Eldridge, 1962):

$$\frac{\omega^2}{\omega_p^2} = 1 - \frac{\omega^2}{\omega_p^2}\left(\frac{c^2k_{\parallel}^2 - \omega^2 + \omega_p^2}{c^2k_{\parallel}^2 - \omega^2}\right)^{\frac{1}{2}} \begin{matrix}\tanh\\ \coth\end{matrix}\left[\frac{a}{2}\left(k_{\parallel}^2 - \frac{\omega^2 - \omega_p^2}{c^2}\right)^{\frac{1}{2}}\right]. \qquad \text{(II-81)}$$

In the limit of $k_{\parallel} >> \omega/c$ (the nonretarded limit), it can be seen that Eq. (II-81) becomes (II-80). Similarly, when the quantity $|\vec{k}_{\parallel}|a$ becomes large, the exponential term describing the splitting of the plasmon into two branches becomes very small, and the limiting value of $\omega = \omega_p/\sqrt{2}$ is reached. One striking feature of both (II-80) and (II-81) is that two distinct modes of oscillation occur; the charge oscillations on the upper and lower surfaces of the slab interact with each other and produce two normal modes of oscillation as with a pair of coupled classical oscillators. The mode corresponding to the (+) sign in Eq. (II-80) and the (tanh) in Eq. (II-81) arises from an antisymmetrical charge distribution on the two sides of the slab, a positive charge density opposite a negative charge density and vice versa. The mode corresponding to the (-) sign in Eq. (II-80) and the (coth) in Eq. (II-81) is similarly due to a symmetric charge distribution on the two sides of the slab. The frequency (energy) of the oscillations is raised in the antisymmetrical case and lowered by the same amount in the symmetrical case due to the difference in electrostatic potential energy of $+(\delta q)^2/a$ which exists between opposite antinodes; and for the antisymmetric case, the electrostatic potential energy between corresponding antinodes is $(\delta q)^2/a$. Hence, the frequency is lowered for the symmetric mode and raised for the antisymmetric since the total energy is the same.

Dispersion relations in the planar case can also be obtained for the reciprocal geometry of a vacuum of width *a* between two planar slabs. For the nonretarded case we have:

$$\frac{\omega^2}{\omega_p^2} = \frac{1}{2}\left(1 \pm e^{-|\vec{k}_\parallel|a}\right) \tag{II-82}$$

and in the retarded regime

$$\frac{\omega^2}{\omega_p^2} = 1 - \frac{\omega^2}{\omega_p^2}\left(\frac{c^2k_\parallel^2 - \omega^2}{c^2k_\parallel^2 - \omega^2 + \omega_p^2}\right)^{\frac{1}{2}} \begin{matrix}\tanh\\ \coth\end{matrix}\left[\frac{a}{2}\left(k_\parallel^2 - \frac{\omega^2}{c^2}\right)^{\frac{1}{2}}\right] . \tag{II-83}$$

It can be seen that the classical nonretarded modes are identical in the reciprocal geometry, whereas the retarded modes are somewhat different, the wave vector in the argument of the (tanh) and (coth) being vacuum retarded as opposed to dielectric retarded.

Likewise, the surface plasmon dispersion relation in the infinite cylinder geometry has been calculated (Ashley and Emerson, 1974). In the case of no retardation, the dispersion relation for the m^{th} mode on a dielectric cylinder in a vacuum is:

$$\frac{\omega_m^2}{\omega_p^2} = kaI_{m+1}(ka)\ K_m(ka) + mI_m(ka)\ K_m(ka) \tag{II-84}$$

where I_m and K_m are the modified Bessel functions of the first and second kinds, respectively. The retarded dispersion relation is given by:

$$\kappa^2\kappa_o^2 \left[\kappa \frac{I_m'(\kappa_o a)}{I_m(\kappa_o a)} - \kappa_o \varepsilon(\omega) \frac{K_m'(\kappa a)}{K_m(\kappa a)}\right] \times \left[\kappa \frac{I_m'(\kappa_o a)}{I_m(\kappa_o a)} - \kappa_o \frac{K_m'(\kappa a)}{K_m(\kappa a)}\right] = \frac{m^2}{a^2}\,[\varepsilon(\omega) - 1\ {}^2 k^2 \frac{\omega^2}{c^2} \tag{II-85}$$

where $\kappa_o^2 = k^2 - \omega^2/c^2$ and $\kappa^2 = k^2 - \varepsilon(\omega)\ \omega^2/c^2$, and the ' on the Bessel function denotes differentiation with respect to the argument. For the complementary geometry of a cylindrical void in a dielectric media, the m^{th} nonretarded dispersion relation is:

$$\frac{\omega_m^2}{\omega_p^2} = kaK_{m+1}(ka)\ I_m(ka) - mK_m(ka)\ I_m(ka) \tag{II-86}$$

and the retarded plasmon dispersion is:

$$\kappa^2\kappa_o^2 \left[\kappa_o \frac{I_m'(\kappa a)}{I_m(\kappa a)} - \kappa\varepsilon(\omega) \frac{K_m'(\kappa_o a)}{K_m(\kappa_o a)}\right] \times \left[\kappa_o \frac{I_m'(\kappa a)}{I_m(\kappa a)} - \kappa \frac{K_m'(\kappa_o a)}{K_m(\kappa_o a)}\right] \tag{II-87}$$

$$= \frac{m^2}{a^2}\left[\frac{\varepsilon(\omega) - 1}{\varepsilon(\omega)}\right]^2 k^2 \frac{\omega^2}{c^2} .$$

If one goes to the $c \to \infty$ limit in Eqs. (II-85) and (II-87), the simple dispersion relations of (II-84) and (II-86) are obtained using the Wronskian for the I_m and K_m Bessel functions. Of interest is the large ka limit. If ka is taken to be much greater than 1, we find for Eqs. (II-84) and (II-86):

$$\frac{\omega_m^2}{\omega_p^2} = \frac{1}{2} \pm \frac{m}{2ka} . \qquad \text{(II-88)}$$

The second term on the RHS of II-88 vanishes for ka >> m, and we are left with the planar limit of $\omega_p/\sqrt{2}$. Dispersion relations (II-81) and (II-85) are shown in Fig. 8 for small values of $k_p a$ to contrast the mode splitting between the planar and cylindrical geometries. Figure 9 shows the dispersion relation of Ashley and Emerson for $k_p a = 0.6071$ and angular modes 0, 1, 2, and 10. Figure 10 shows the dispersion relations for a vacuum cylinder and a dielectric cylinder for values of $k_p a$ consistent with 470 Å and 200 Å diameter Ag cylinders. The dotted lines indicate the coupling wave vector for 700- and 900-eV electrons.

It is of some interest to contrast the planar and the cylindrical surface plasmons. If we let the thickness of the slab go to infinity, the nonretarded plasmons converge to $\omega_p/\sqrt{2}$, while the retarded plasmons simplify to (Raether, 1965):

$$\frac{\omega^2}{\omega_p^2} = \frac{1}{2} + \frac{k^2c^2}{\omega_p^2} - \frac{k^2c^2}{\omega_p^2}\sqrt{1 + \omega_p^4/4k^4c^4} . \qquad \text{(II-89)}$$

ORNL-DWG 81-17530

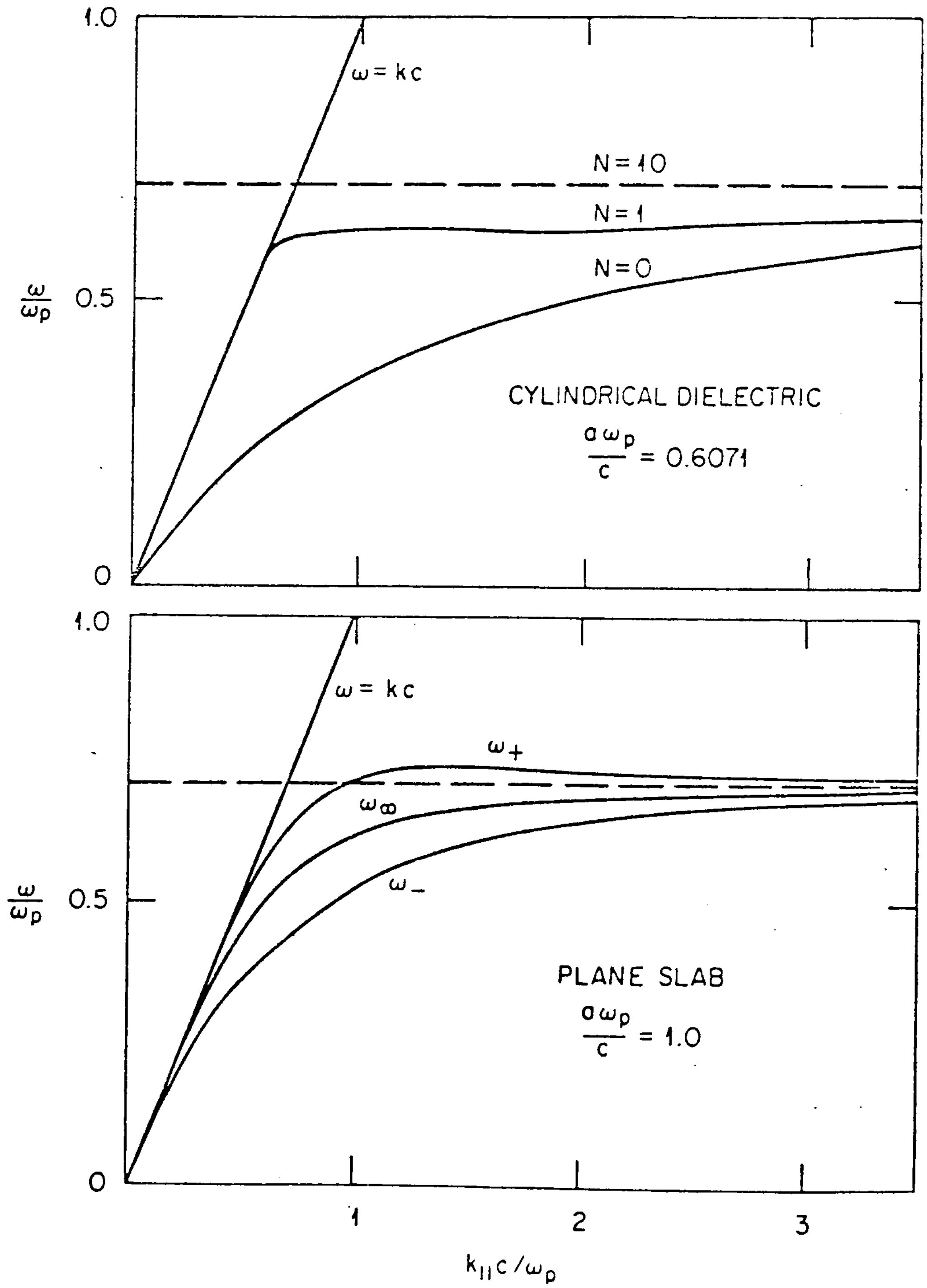

Figure 8. Retarded Surface Plasmon Dispersion Relation for a Cylindrical Dielectric of Radius a for $a\omega_p/c = 0.6071$ (Ashley and Emerson, 1974) and for a Plane Slab of Thickness a with $a\omega_p/c = 1.0$ (Ritchie and Eldridge, 1962).

ORNL–DWG 81-18234

DISPERSION RELATIONS FOR NON-RADIATIVE SURFACE PLASMONS

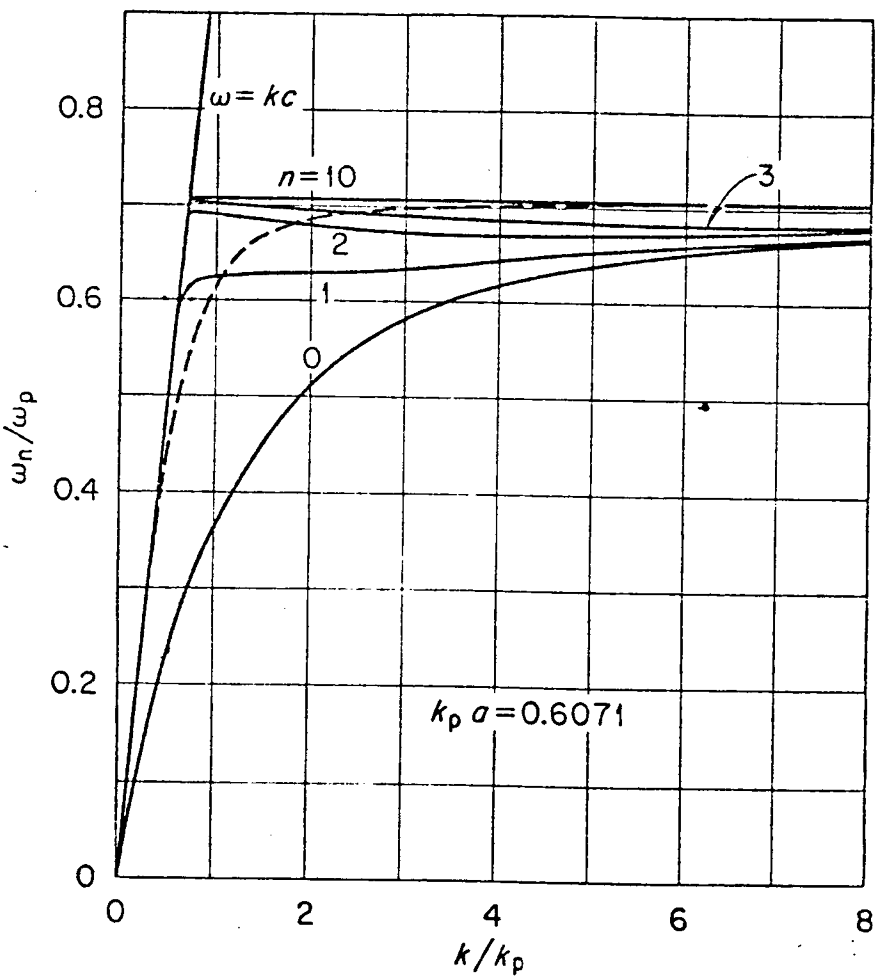

Figure 9. Retarded Surface Plasmon Dispersion Relation for a Cylindrical Dielectric of Radius a Showing Azimuthal Modes 0, 1, 2, 3, and 10 for $a\omega_p/c = 0.6071$.

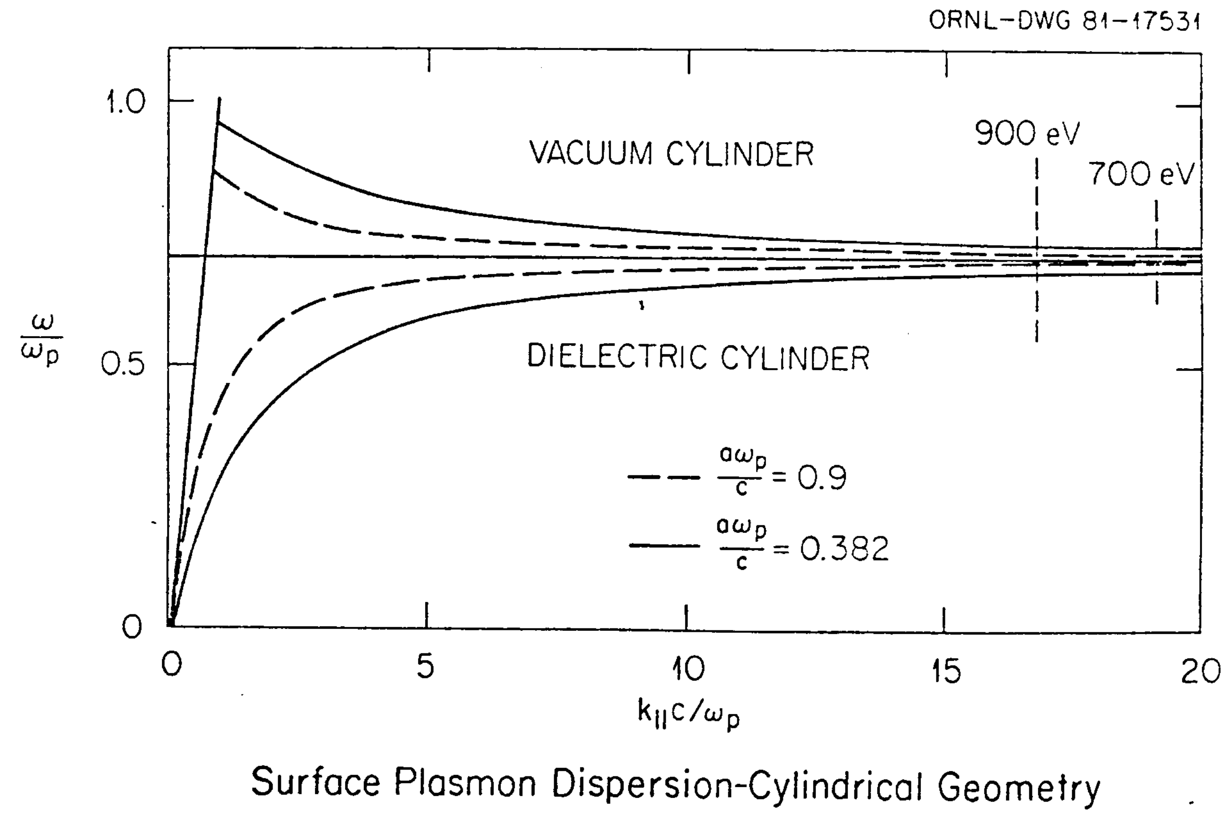

Figure 10. Retarded Surface Plasmon Dispersion Relation for a Cylindrical Void (upper) and Cylindrical Dielectric (lower) of Radius a, Azimuthal Mode 0 with $a\omega_p/c = 0.9$ (----) and 0.382 (——), Corresponding to Cylinder Diameters of 470 and 200 Å of Ag, Respectively. The dashed vertical lines denote the coupling wave vector for 700- and 900-eV electrons.

In either case, one dispersion relation remains, which for values of $kc/\omega_p = k/k_{light} > 2$ is within about 3% of the asymptotic value $\omega_p/\sqrt{2}$. Now, for the cylinder we have markedly different results. The cylindrical geometry is a partially closed surface midway between that of a plane and a completely closed surface such as that of a spheroid. On the plane we have travelling waves $\cos(\vec{k}\cdot\vec{\rho})$ and $\sin(\vec{k}\cdot\vec{\rho})$, where $\vec{\rho} = x e_x + y\hat{e}_y$ along the surface. The cylinder supports waves described by $\cos(kz)$ and $\sin(kz)$ along the axial direction of the cylinder but requires a standing wave be formed around the cylinder, since the fields must be continuous at $\phi = 0,\ 2\pi$. The total surface momentum is thus discrete in the azimuthal direction but continuous in the axial direction. Since the wavelength around the cylinder is $2\pi a/m$, the azimuthal wave vector is $k_p = m/a$, and the total wave vector:

$$\vec{k} \quad = \quad k\hat{z} + \frac{m}{a}\hat{\phi} \ . \qquad \text{(II-90)}$$

In general, the wave vector on the cylinder describes a helical propagation. For fixed values of ka, as the order m of the surface mode increases, the surface plasmon frequency ω_m approaches the asymptotic value, $\omega_p/\sqrt{2}$, more and more rapidly as shown in Fig. 7. This is in accordance with the planar plasmons; as the total surface momentum increases, the surface plasma frequency approaches the asymptotic limit.

As a further illustration of this contrast between standing and travelling waves, we may consider the surface modes on a dielectric sphere of radius *a* (Kunz and Raether, 1963). Here the surface plasma frequency is given by:

$$\frac{\omega_m^2}{\omega_p^2} = \frac{1}{2 + 1/m} \tag{II-91}$$

subject to the condition $\omega_p/c \ll m/a$ (retardation neglected). The surface modes are entirely discrete; and as m approaches infinity, the planar limit of $\omega_p/\sqrt{2}$ is reached. A common thread in all the geometries considered is that as the plasmon wavelength becomes much less than the local radius of curvature, the surface to all intents and purposes is well approximated by a plane, and the planar surface plasmon dispersion is reached.

In general, any finite range coordinate will support only standing waves with a discrete valued wave vector, and infinite range coordinates support standing waves with a continuous valued wave vector. A geometry described by a surface of revolution will contain discrete modes and in some cases, such as cylindrical geometry, a mixture of discrete and continuous modes.

We now consider the problem of surface oscillations on a hole in a thick sheet. In order to make the problem mathematically tractable, the interface between the hole and dielectric is modelled as a hyperboloid of revolution of one sheet, with the vacuum containing the region of the hole between the hyperboloid nadir circles out to infinity; while the medium characterized by frequency-dependent dielectric response $\tilde{\varepsilon}(\omega)$ lies between the hyperboloid asymptotes. The region of the vacuum is seen to contain the z-axis in its entirety. In this geometry the problem of finding the surface plasmon dispersion relation reduces to that of solving Laplace's equation (nonretarded modes) and Poisson's equation (retarded modes) in an oblate spheroidal coordinate system (Fig. 11).

The problem of solving Laplace's equation in the oblate spheroidal geometry has been examined in some detail in a previous work (Snow, 1952). The oblate spheroidal coordinates θ and β are shown in Fig. 11. The oblate spheroidal coordinate system is obtained by rotating an elliptical coordinate system consisting of confocal ellipses and hyperbolas about an axis, z, normal to the line joining the foci at $\rho = \pm a$. The β coordinate corresponds to a given oblate spheroid (rotated ellipse) and serves to measure distance along the hyperboloids of one sheet whose asymptotes are specified by the line with slope $\pm\cos(\theta)$ passing through the origin. The β coordinate can be considered a generalized radius and θ coordinate a generalized polar angle in a spherical coordinate system whose caustic has been expanded from a point at the origin to a ring centered at the origin lying in the x-y plane with radius a. The angle specifies the azimuth around the z-axis. The relation between cylindrical coordinates, (p, ϕ, z), and the oblate spheroidal coordinates is given by:

$$z = a\cos\theta \sinh\beta \ , \qquad \rho = a\sin\theta \cosh\beta \ . \tag{II-92}$$

The metric, h, is given by:

$$h = a(\cosh^2\beta - \sin^2\theta)^{\frac{1}{2}} = a(\sinh^2\beta + \cos^2\theta)^{\frac{1}{2}} \ . \tag{II-93}$$

It is noted that for large values of β, $\sinh(\beta) \approx \cosh(\beta) \approx 1/2\ e^{\beta}$. Since the distance from the origin, r, is given by $(z^2 + \rho^2)^{\frac{1}{2}}$, then for large β

ORNL-DWG 80-17820

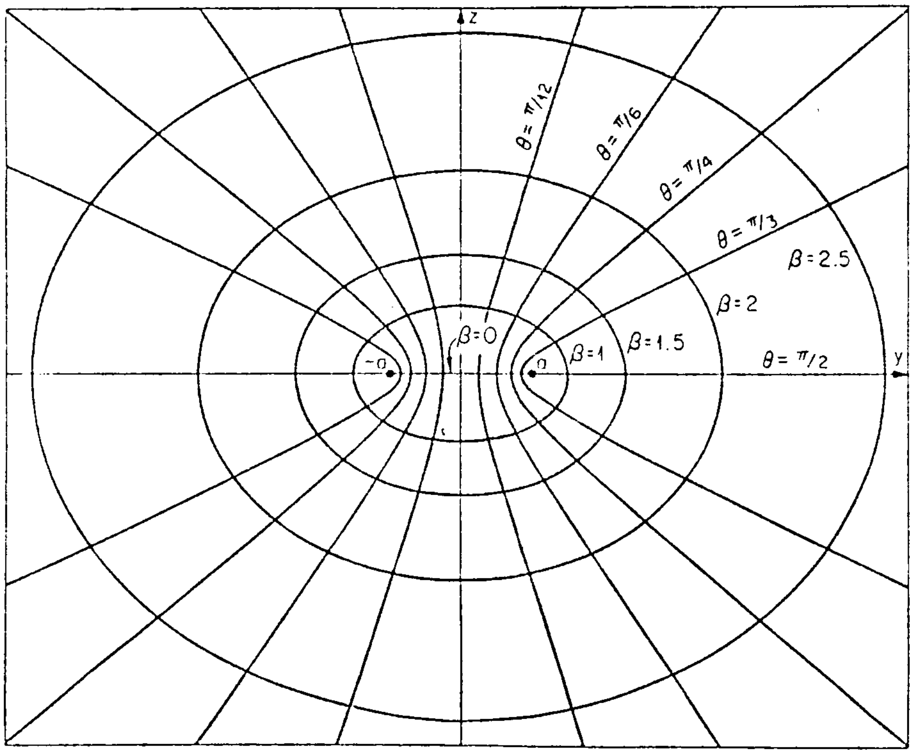

Figure 11. Oblate Spheroidal Coordinate System Section in y-z Plane. β is the generalized radius corresponding to confocal oblate spheroids with foci at $\rho = \pm a$. θ is the generalized polar angle corresponding to hyperboloids of revolution of one sheet with foci at $\rho = \pm a$.

$$r \underset{\sim}{\sim} \frac{a}{2} e^{\beta} \tag{II-94}$$

and β is proportional to the natural logarithm of the radius. The individual metric elements h_ρ, h_θ, and h_ϕ are:

$$\begin{aligned} h_\beta^{\;2} &= h_\theta^{\;2} = h^2 = a^2(\sinh^2\beta + \cos^2\theta) \\ h_\phi^{\;2} &= \rho^2 = a^2 \sin^2\theta \cosh^2\beta \; . \end{aligned} \tag{II-95}$$

The Laplacian is then:

$$\begin{aligned} \nabla^2 = \; & \frac{1}{h^2 \cosh\beta} \frac{\partial}{\partial\beta}\left(\cosh\beta \frac{\partial}{\partial\beta}\right) + \frac{1}{h^2 \sin\theta} \frac{\partial}{\partial\theta}\left(\sin\theta \frac{\partial}{\partial\theta}\right) \\ & + \frac{1}{h_\phi^{\;2}} \frac{\partial^2}{\partial\phi^2} \; . \end{aligned} \tag{II-96}$$

We shall confine this investigation to the solution of Laplace's equation; the $c \to \infty$ limit is taken, and retardation is neglected. Further comments on the effects of retardation on the conditional separation of the partial differential equation describing the electric potential $\Phi(\vec{r})$ will be given later.

Historically, the branch cut in the ρ-z plane in oblate spheroidal coordinates has been taken to be between the foci, from $-a$ to $+a$. In the present problem, this choice of branch cut would require the cut line to pass through the boundary surfaces of the dielectric. For this physical reason, the branch cut from $-a$ to $+a$ is not acceptable and has been changed to the complementary cut from $-\infty < \rho \leq a$, and $a \leq \rho < \infty$

in the ρ-z plane. Such a choice of cut line forces a change in the range of the coordinates β and θ (Snow, 1952, p. 7). The generalized radius, β, ranges over $-\infty < \beta < \infty$, while the generalized polar angle is restricted to $0 \leq \theta \leq \pi/2$. In effect, positive and negative radii are allowed, but the polar angle is restricted to ranging over the upper half-space.

The following development of the electric potential is due to Snow (pp. 300-317); an abbreviated and streamlined version can be found in the literature (Becker, *et al.*, 1981a). The older derivation will be presented here to illustrate some additional points in the development of the solution and properties of the functions involved.

Traditional separation of variables is used; the potential $\Phi(\vec{r})$ is presumed to be expandable as a linear combination of terms in $e^{im\phi}$ as:

$$\Phi(\rho,z,\phi) = \sum_{m=-\infty}^{+\infty} \Phi^m(\rho,z)\, e^{im\phi} . \qquad \text{(II-97)}$$

A transformation is then made (Snow, p. 228) to Euler's reduced potential by taking:

$$\Phi^m(\rho,z) = \frac{1}{\sqrt{\rho}}\, U^m(\rho,z) \qquad \text{(II-98)}$$

where the quantity U^m is the m^{th} coefficient in the multipole expansion of the reduced potential, $U(\beta,\theta)$, oscillator product functions. Substituting the RHS of (II-98) into Laplace's equation for oblate spheroidal coordinates gives the differential equation governing the reduced potential

$$\left[\frac{\partial^2}{\partial\beta^2} + \frac{\partial^2}{\partial\theta^2} + \left(\frac{1}{4} - m^2\right)\left(\frac{1}{\sin^2\theta} - \frac{1}{\sinh^2\beta}\right)\right] U^m(\beta,\theta) = 0. \quad \text{(II-99)}$$

Separating the reduced potential into products of functions $u(\beta)$ and $v(\theta)$ results in the following differential equations:

$$u'' + \left(\frac{m^2 - \frac{1}{4}}{\cosh^2\beta} - \mu^2\right) u = 0 \quad \text{(II-100a)}$$

$$v'' + \left(\frac{\frac{1}{4} - m^2}{\sin^2\theta} + \mu^2\right) v = 0 \quad \text{(II-100b)}$$

where μ^2 is a constant of separation for Eq. (II-99). While the separation constant m^2 is due to the azimuthal term $e^{\pm im\phi}$ and hence is restricted to integer values, the quantity μ^2 is related to the angular and radial coordinates and is as yet unspecified but will subsequently be shown to be continuous.

A final transformation is made (Snow, p. 303), where both v and u are given by:

$$x = i\cot\theta, \qquad v(\theta) = y(x) \quad \text{(II-101a)}$$

$$x = \tanh\beta, \qquad u(\beta) = y(x). \quad \text{(II-101b)}$$

After some manipulation, both Eqs. (II-100a) and (II-100b) can be put into the following form:

$$\frac{d}{dx}\left[(1 - x^2)\frac{dy}{dx}\right] + \left(m^2 - \frac{1}{4} - \frac{\mu^2}{1 - x^2}\right) y = 0. \quad \text{(II-102)}$$

This is seen to be Legendre's equation for $y(x)$ with upper index μ and lower index $m - 1/2$ and is termed (Hobson, 1965, p. 445) as the differential equation describing the solution to the angular functions in a conical geometry; the functions $y(x)$ are called cone functions. The solutions are then generalized Legendre functions

$$\underline{P}^{\mu}_{m-\frac{1}{2}}\ (i\cot\theta)\ , \qquad \underline{P}^{\mu}_{m-\frac{1}{2}}\ (\tanh\beta) \tag{II-103}$$

for the angular and radial solutions. The functions $\underline{P}^{\mu}_{m-\frac{1}{2}}(i\cot\theta)$ have been investigated by Mehler (Hobson, p. 445) and are referred to as "kegelfunctionen." Noting the restriction on the range of θ, two linearly independent solutions are generated (see appendix):

$$\sqrt{\sin\theta}\ \underline{P}^{m}_{-\frac{1}{2}+\mu}\ (+\cos\theta)\ , \qquad \sqrt{\sin\theta}\ \underline{P}^{m}_{-\frac{1}{2}+\mu}\ (-\cos\theta)\ . \tag{II-104}$$

An interesting and useful property of the kegelfunctions is that the only singularity on the real axis occurs at arg = -1; the functions $\underline{P}^{m}_{-\frac{1}{2}+\mu}(\cos\theta)$ are finite in the entire range of θ employed here, while the $\underline{P}^{m}_{-\frac{1}{2}+\mu}(-\cos\theta)$ are singular on the z-axis ($\theta = 0$).

The reduced potential of order m can be written as:

$$U^{m}(\beta,\theta) = \sqrt{\sin\theta}\ \left[A\underline{T}^{\mu}_{m-\frac{1}{2}}\ (\tanh\beta) + B\underline{T}^{\mu}_{m-\frac{1}{2}}\ (-\tanh\beta)\right] \times \left[C\underline{T}^{m}_{\mu-\frac{1}{2}}\ (\cos\theta) + D\underline{T}^{m}_{\mu-\frac{1}{2}}\ (-\cos\theta)\right] \tag{II-105}$$

where the functions $\underline{T}^{\mu}_{m-\frac{1}{2}}$ and $\underline{T}^{m}_{\mu-\frac{1}{2}}$ are related to the Legendre functions $\underline{P}^{-\mu}_{m-\frac{1}{2}}$ and $\underline{P}^{m}_{-\frac{1}{2}+\mu}$ by a complex valued constant (see appendix). The coefficients A, B, C, and D are constants to be determined by the boundary conditions.

External to the dielectric (hyperboloid), the angular solutions can only contain terms in $\underline{P}^{m}_{-\frac{1}{2}+\mu}(\cos\theta)$ since the kegelfunctions of negative argument are singular on the z-axis; the potential is then everywhere smooth and continuous in the range $0 \leq \theta \leq \theta_o \leq \pi/2$. It is found to be convenient, and results in no loss of generality, to express the angular solutions, v, in terms of even and odd parity functions:

$$v_1(\theta) = \underline{P}^{m}_{-\frac{1}{2}+\mu}(\cos\theta) + \underline{P}^{m}_{-\frac{1}{2}+\mu}(-\cos\theta) \qquad \text{(II-106a)}$$

$$v_1(\theta) = \underline{P}^{m}_{-\frac{1}{2}+\mu}(+\cos\theta) - \underline{P}^{m}_{-\frac{1}{2}+\mu}(-\cos\theta) \, . \qquad \text{(II-106b)}$$

It is apparent that under a change of variable to $\theta' = \pi - \theta$, $v_1(\theta') = v_1(\theta)$, and $v_2(\theta') = -v_2(\theta)$; hence, v_1 is an even function in θ, and v_2 is odd. In a similar fashion we may group the functions $\underline{T}^{\mu}_{m-\frac{1}{2}}(\pm\tanh\beta)$ (Snow, p. 312). Using the notation due to Snow, we have:

$$C^{\mu}_{m}(\beta) = U_1(\beta) = \frac{1}{2}\left[\underline{T}^{\mu}_{m-\frac{1}{2}}(\tanh\beta) + \underline{T}^{\mu}_{m-\frac{1}{2}}(-\tanh\beta)\right] \qquad \text{(II-107a)}$$

$$S^{\mu}_{m}(\beta) = U_2(\beta) = \frac{1}{2}\left[\underline{T}^{\mu}_{m-\frac{1}{2}}(\tanh\beta) - \underline{T}^{\mu}_{m-\frac{1}{2}}(-\tanh\beta)\right] \qquad \text{(II-107b)}$$

with similar parity properties, even for the C^{μ}_{m} and odd for the S^{μ}_{m}, under a coordinate reflection $\beta' \to -\beta$. It is shown in the appendix that the C^{μ}_{m} can be expanded as an even power series in $\tanh(\beta)$, while the S^{μ}_{m} can be expressed as an odd power series in $\tanh(\beta)$.

The complete solution to the reduced potential U^m and, therefore, the potential Φ^m itself can be expressed in terms of products of definite parity radial solutions u_1 and u_2 with definite parity polar solutions v_1 and v_2 as:

$$U^m(\beta,\theta) = \sqrt{\sin\theta}\,[au_1(\beta) + bu_2(\beta)][cv_1(\theta) + dv_2(\theta)] \ . \qquad \text{(II-108)}$$

The physically allowable solutions can be reduced considerably by considering the electric potential and electric field internal to the dielectric (hyperboloid) and the properties of the conical harmonics in the immediate neighborhood of the branch cut. At a distance $\varepsilon << 1$ above and below the cut, corresponding to polar angle $\theta = \pi/2 - \delta$, $\delta << 1$, mirror field points correspond to $+\beta$ and $-\beta$. As θ approaches $\pi/2$, v_2 vanishes while v_1 remains finite by inspection. Since physically allowable potentials must be continuous in the absence of a surface charge distribution, the even parity angular functions must be paired with the even parity radial functions, viz., $u_1(\beta)v_1(\theta)$. Turning to the electric fields in the neighborhood of the cut mirror points, we find that differentiation of the radial solutions u_1 and u_2 with respect to $\tanh(\beta)$ shows that $d/dx\ u_2(x)$ has equal but opposite values at $+\beta$ and $-\beta$. Again, physically allowable solutions for the electric field must be continuous in the absence of a surface charge distribution; and in a similar fashion as for the electric potential, the odd parity solutions $u_2(\beta)$ and $v_2(\beta)$ must be paired. The solutions for the reduced potential internal and external to the dielectric are then:

$$U_<^m = \sqrt{\sin\theta}\,[a'u_1(\beta)\ v_1(\theta) + b'u_2(\beta)\ v_2(\theta)]$$

$$U_>^m = \sqrt{\sin\theta}\,\underline{P}^m_{-\frac{1}{2}+\mu}(\cos\theta)\ [A'u_1(\beta) + B'u_2(\beta)]\ , \tag{II-109}$$

while the real potential's m^{th} coefficient is:

$$\Phi_<^m = \frac{1}{a\sqrt{\cosh\beta}}\left\{a'C_m^\mu(\beta)\left[P^m_{-\frac{1}{2}+\mu}(\cos\theta) + \underline{P}^m_{-\frac{1}{2}+\mu}(-\cos\theta)\right]\right.$$

$$\left. + b'\ S_m^\mu(\beta)\left[\underline{P}^m_{-\frac{1}{2}+\mu}(\cos\theta) - \underline{P}^m_{-\frac{1}{2}+\mu}(-\cos\theta)\right]\right\} \tag{II-110}$$

$$\Phi_>^m = \frac{1}{a\sqrt{\cosh\beta}}\ \underline{P}^m_{-\frac{1}{2}+\mu}(\cos\theta)\left[A'C_m^\mu(\beta) + B'S_m^\mu(\beta)\right]$$

in the nonretarded limit. If, instead, we had taken the speed of light to be finite, solutions of Poisson's equation $[\nabla^2 + \varepsilon(\omega^2/c^2)]\Phi = 0$ would have been required instead of solutions of Laplace's equation. The solutions to Poisson's equation would have been found to involve the spheroidal wave functions and would have added considerably to the complexity of the solution.

D. Surface Plasmon Dispersion Relation on the Hyperboloids

Recalling that the solutions for the electric potential internal and external to the dielectric are required to be physical, we consider the allowed values of the index μ for the radial and angular functions $C_m^\mu(\beta)$, $S_m^\mu(\beta)$, $\underline{P}^m_{-\frac{1}{2}+\mu}(\cos\theta)$, and $\underline{P}^m_{-\frac{1}{2}+\mu}(-\cos\theta)$. Referring to previous discussion in this section, we require a standing wave with discrete value momentum to be supported in the azimuthal coordinate ϕ (hence m is integral), and we require the radial solutions to be standing waves with continuous valued momentum and, therefore, oscillatory in the asymptotic limit. A close examination of the expansion for C_m^{μ} and S_m^{μ} in the appendix shows that when the index μ is taken to be ik, where k is continuous and real with range $0 \leq k < \infty$, the surface harmonic orthogonality condition is satisfied and radial solutions are oscillatory in the asymptotic regime:

$$C_m^{ik} \sim S_m^{ik} \rightarrow e^{ik\,ln\cos\beta} \rightarrow e^{ik\beta} \qquad \text{(II-111)}$$

since for large values of β, the hypergeometric function approaches a constant. From Eq. (II-111) the radial distance for large values of β is approximately

$$r \stackrel{\sim}{\sim} a\cosh\beta \ , \qquad \text{(II-112)}$$

and the scalar potential has the asymptotic form of

$$\Phi^m \sim \frac{e^{ik\,ln(r/a)}}{\sqrt{r}} \qquad \text{(II-113)}$$

identical to the radial solutions for conical geometries where the hyperbolas in the asymptotic limit take on the shape of their conical asymptotes (Hobson, 1965, p. 448). Conical geometries such as multiple cones are limiting cases of the hyperboloidal geometry and can be considered to be complementary.

In order to derive the nonretarded dispersion relation for surface oscillations, we employ the macroscopic method; the general boundary conditions on Maxwell's equations and the EM fields are invoked. Requiring continuity of the electric potential at the interface θ_o yields:

$$\Phi^m_< (\cos\theta_o) = \Phi^m_> (\cos\theta_o) \tag{II-114}$$

and on the normal component of the electric displacement:

$$\hat{\varepsilon}(\omega)\ \hat{\theta}\cdot\nabla\Phi^m_< \Big|_{\cos\theta_o} = \hat{\theta}\cdot\nabla\Phi^m_> \Big|_{\cos\theta_o} . \tag{II-115}$$

Now, the functions C^{ik}_m and S^{ik}_m are independent and orthogonal solutions of the radial equation in ρ; the potential can termwise be separated into even and odd parity components, giving for $\hat{\varepsilon}(\omega)$:

$$\hat{\varepsilon}(\omega) = \frac{\underline{P}^{m'}_{-\frac{1}{2}+ik}(\cos\theta_o)\left[\underline{P}^m_{-\frac{1}{2}+ik}(\cos\theta_o) \pm \underline{P}^m_{-\frac{1}{2}+ik}(-\cos\theta_o)\right]}{\underline{P}^m_{-\frac{1}{2}+ik}(\cos\theta_o)\left[\underline{P}'^m_{-\frac{1}{2}+ik}(\cos\theta_o) \pm \underline{P}'^m_{-\frac{1}{2}+ik}(-\cos\theta_o)\right]} . \tag{II-116}$$

To get a feel for the dispersion of the plasmons and to avoid ambiguity in the dispersion due to the presence of damping, the limiting case for $\tilde{\varepsilon}(\omega)$ of a Drude simple metal is taken (viz., $\tilde{\varepsilon} = 1 - \omega_p^2/\omega^2$). We denote $\underline{P}^m_{-\frac{1}{2}+ik}(\cos\theta_o)$ by $\underline{P}_+$ and $\underline{P}^m_{-\frac{1}{2}+ik}(-\cos\theta_o)$ by $\underline{P}_-$ and solve for the oscillation frequencies:

$$\frac{\omega^{m\,2}_k}{\omega_p^2} = \pm\ \frac{\underline{P}_+\ (\underline{P}_+' \pm \underline{P}_-')}{\underline{P}_+\ \underline{P}_-' - \underline{P}_+'\ \underline{P}_-} \tag{II-117}$$

evaluated at the boundary, $\theta = \theta_o$. The denominator of (II-117) is recognized to be the Wronskian of the kegelfunctions (Becker, *et al.*, 1980a)

$$W[P_+P_-] = \frac{2 \cosh k\pi}{(-1)^m \pi \sin^2\theta_o} \prod_{j=1}^{m} \left[k^2 + \frac{(2j-1)^2}{4}\right]. \tag{II-118}$$

This gives a formal dispersion relation of:

$$\frac{\omega_k^m}{\omega_p} = \sin\theta_o \left\{ \frac{(-1)^m \pi \underline{P}^m_{-\frac{1}{2}+ik}(\cos\theta_o)}{2 \cosh k\pi \prod_{j=1}^{m}} \frac{\left[\underline{P}'^m_{-\frac{1}{2}+ik}(\cos\theta_o) \pm \underline{P}'^m_{-\frac{1}{2}+ik}(-\cos\theta_o)\right]}{\left[k^2 + \frac{(2j-1)^2}{4}\right]} \right\}^{\frac{1}{2}}. \tag{II-119}$$

The (-) sign corresponds to even parity symmetric modes, and the (+) sign corresponds to odd parity antisymmetric modes, entirely analogous to the symmetric and antisymmetric modes for the surface plasmons on a thin slab [Eq. (II-80)]. Equation (II-119) is illustrated in Figs. 10-17 for m = 0,1 and various values of k and θ_o. It is to be expected, and is borne out upon calculation, that the antisymmetric modes will have higher energies than the symmetric modes for the same reasons as outlined in the opening discussion of this section involving planar geometry (Figs. 12, 13, 14, and 15). In addition, one would expect the difference between the modes to be more pronounced as θ_o goes to $\pi/2$ (thin sheet limit with maximum interaction between the upper and lower surfaces of the dielectric) and less pronounced as θ_o goes to zero (solid bulk limit with infinite distance between surfaces). Figures 16, 17, 18, and 19 show the m = 0,1 dispersion relations in the k,θ,ω space in pseudo- three-dimensional fashion.

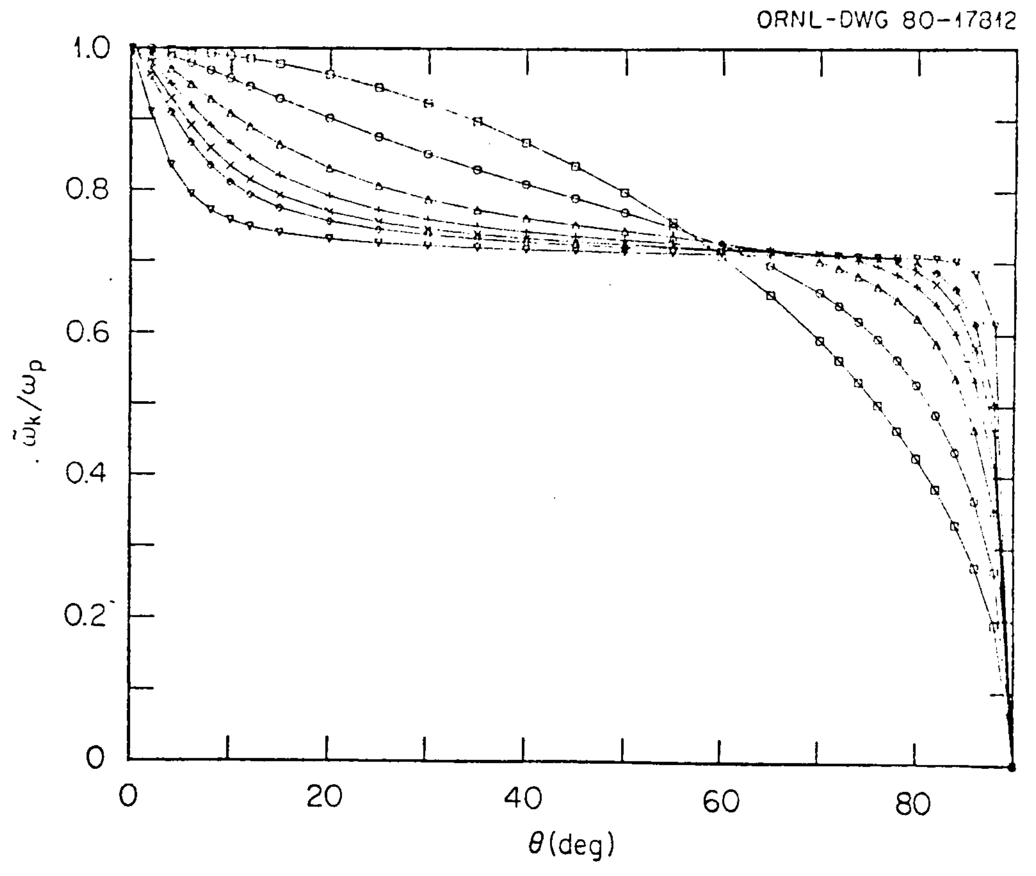

Figure 12. The Symmetric Eigenfrequency in Units of the Bulk Plasma Frequency for the Case of Azimuthal Symmetry Graphed as a Function of Theta for □: k = 0; O: k = 2; Δ: k = 4; +: k = 6; x: k = 8; ◇: k = 10; and ∇: k = 20.

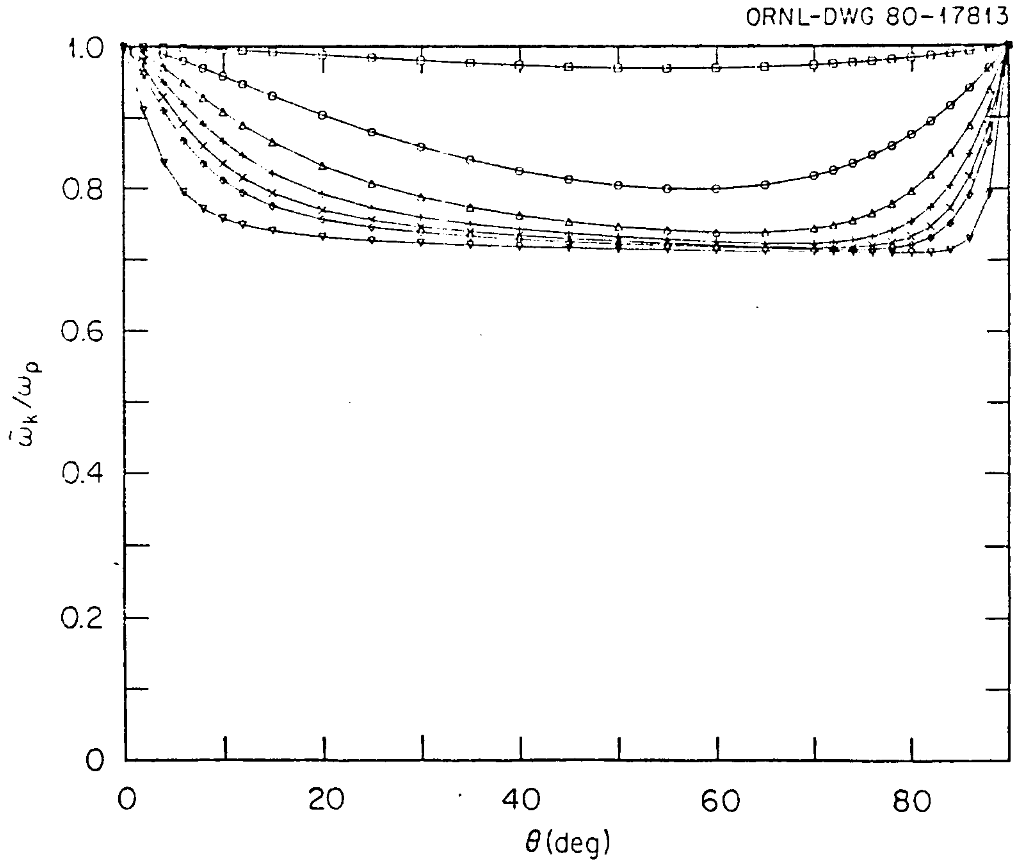

Figure 13. The Antisymmetric Eigenfrequency in Units of the Bulk Plasma Frequency for the Case of Azimuthal Symmetry Graphed as a Function of Theta for □: k = 0; O: k = 2; Δ: k = 4; +: k = 6; x: k = 8; ◇: k = 10; and ∇: k = 20.

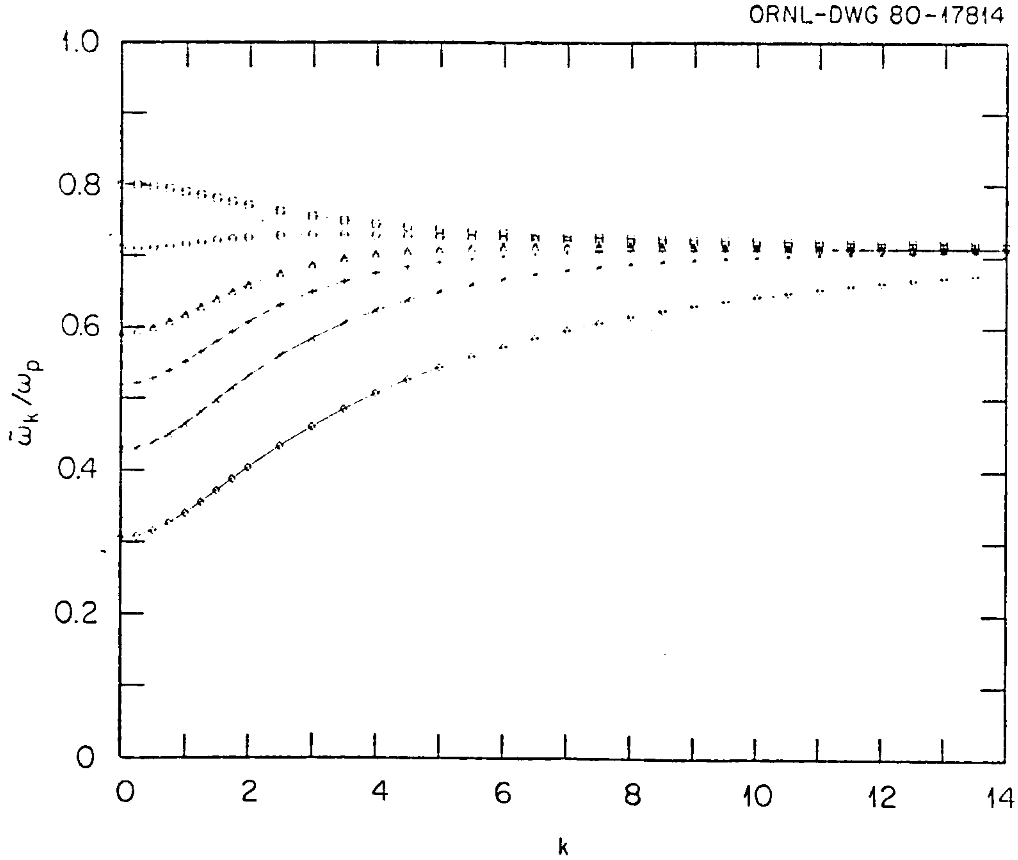

Figure 14. The Symmetric Eigenfrequency in Units of the Bulk Plasma Frequency for the Case of Azimuthal Symmetry Graphed as a Function of the Index k for □: θ = 50°; O: θ = 60°; Δ: θ = 70°; +: θ = 75°; x: θ = 80°; and ◇: θ = 85°.

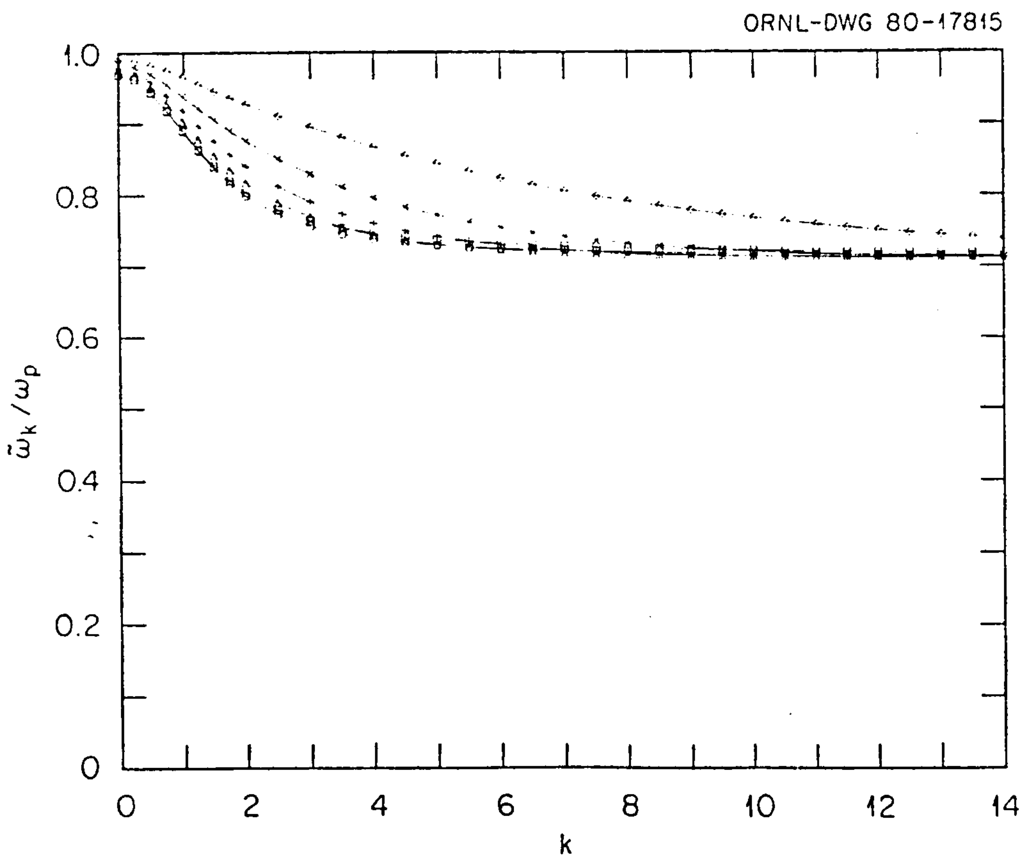

Figure 15. The Antisymmetric Eigenfrequency in Units of the Bulk Plasma Frequency for the Case of Azimuthal Symmetry Graphed as a Function of the Index k for □: θ = 50°; O: θ = 60°; Δ: θ = 70°; +: θ = 75°; x: θ = 80°; and ◇: θ = 85°.

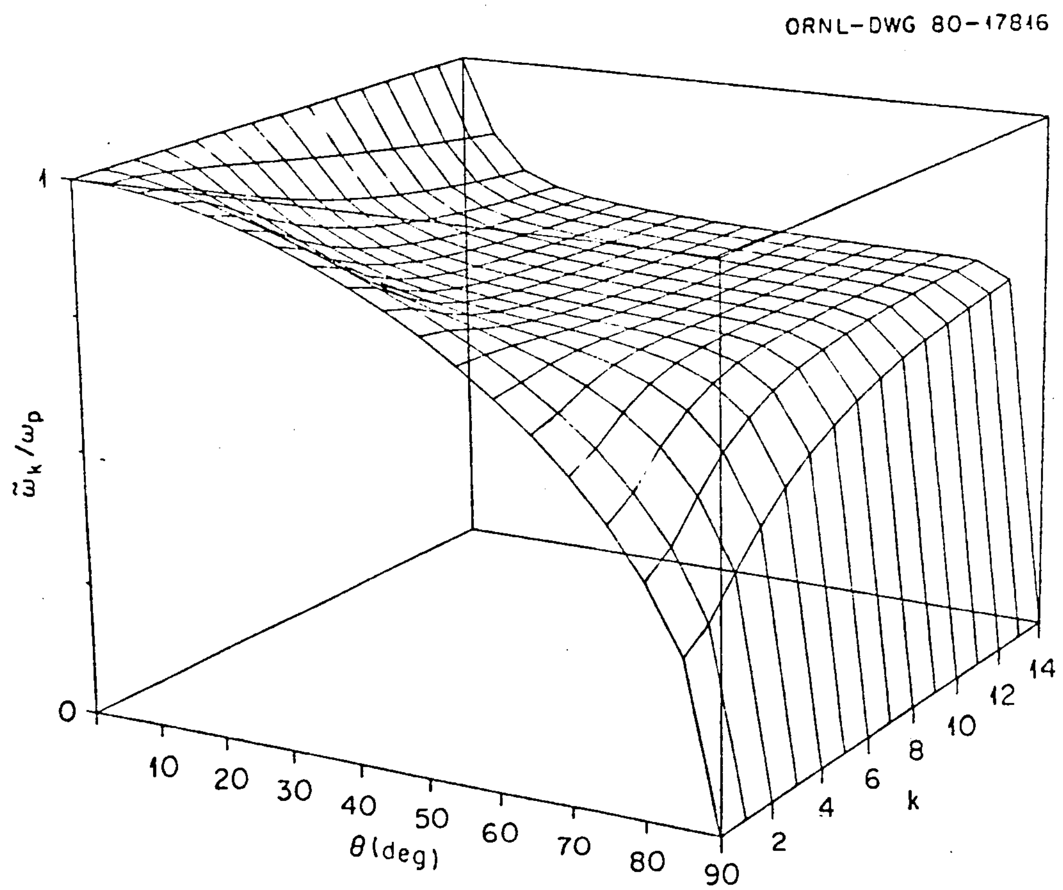

Figure 16. The Symmetric Eigenfrequency in Units of the Bulk Plasma Frequency for the Case of Azimuthal Symmetry Graphed as a Simultaneous Function of Theta and the Index k.

ORNL-DWG 80-17817

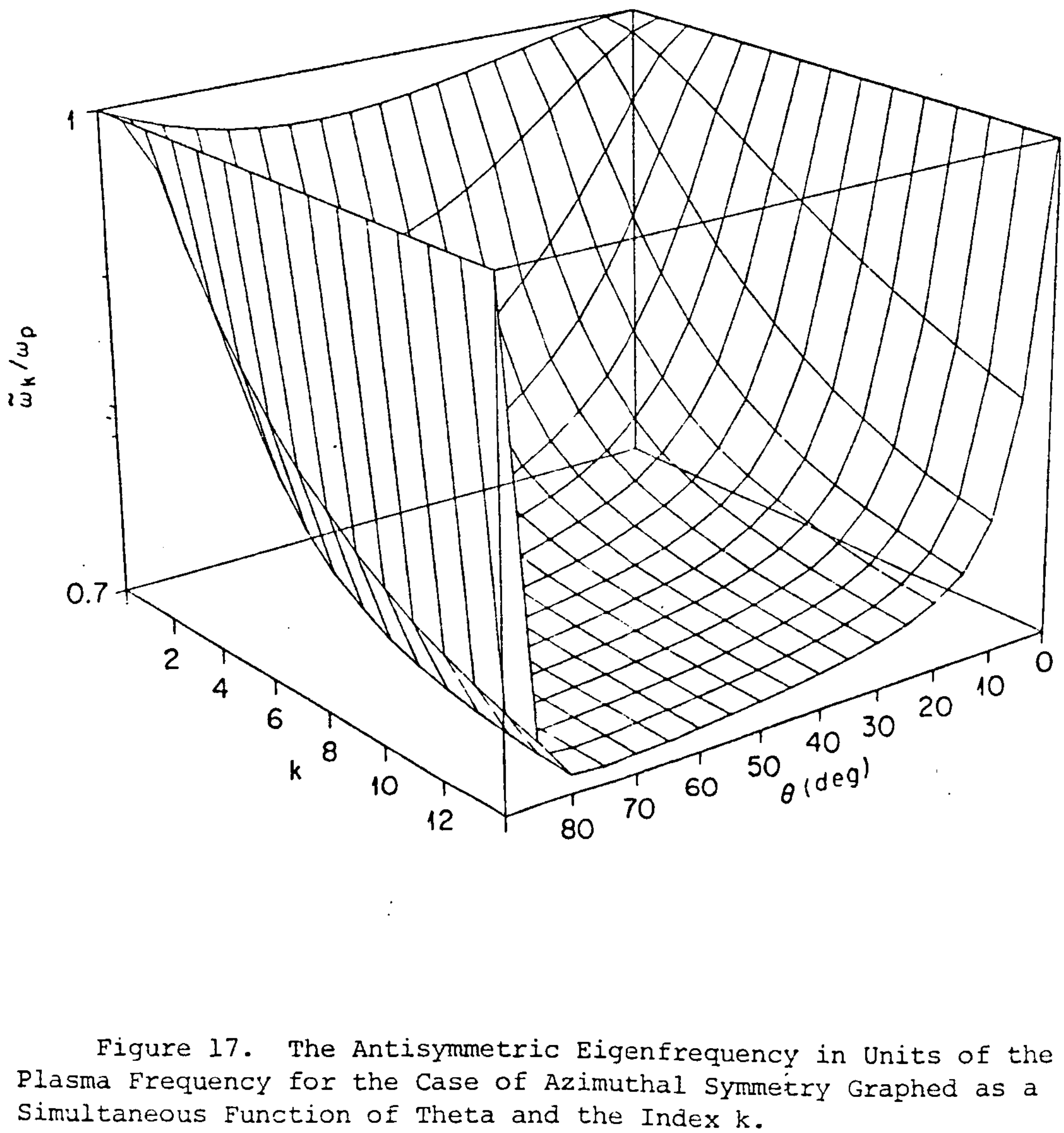

Figure 17. The Antisymmetric Eigenfrequency in Units of the Bulk Plasma Frequency for the Case of Azimuthal Symmetry Graphed as a Simultaneous Function of Theta and the Index k.

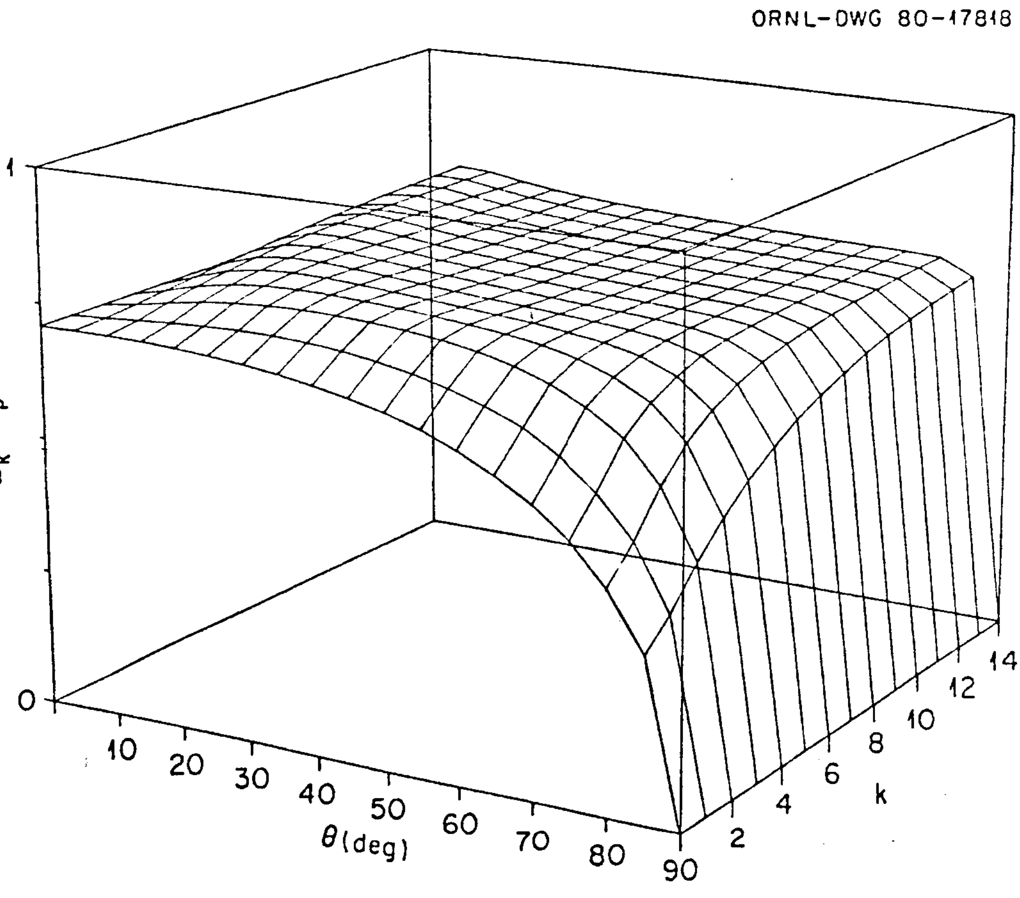

Figure 18. The Symmetric Eigenfrequency in Units of the Bulk Plasma Frequency for m = 1 Graphed as a Simultaneous Function of Theta and the Index k.

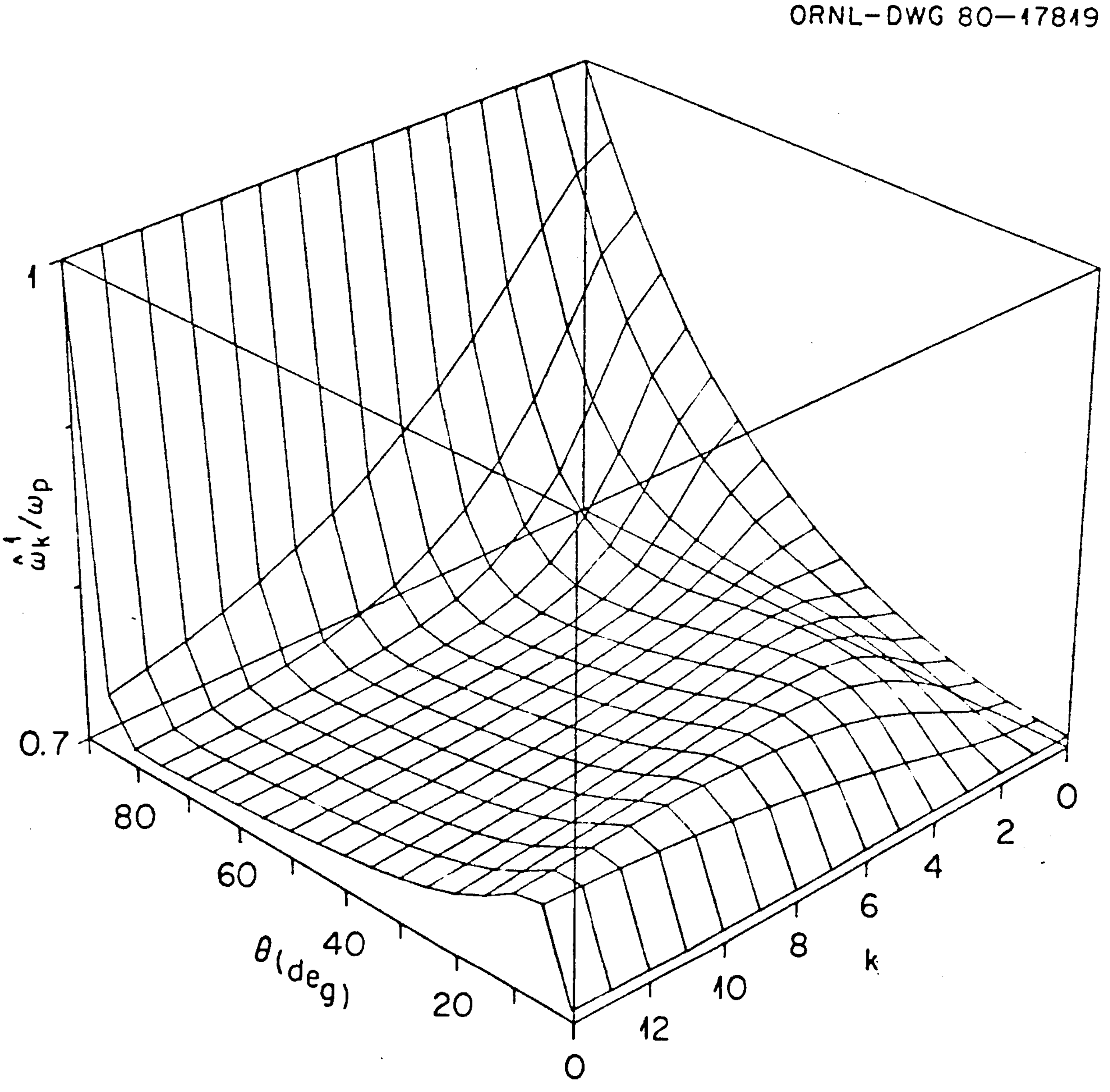

Figure 19. The Antisymmetry Eigenfrequency in Units of the Bulk Plasma Frequency for m = 1 Graphed as a Simultaneous Function of Theta and the Index k.

There are several further interesting aspects of the nonretarded dispersion relation [Eq. (II-119)] that can be gleaned from both the analytic expression and the figures. First, from Eq. (II-119), by inspection the symmetric modes must vanish at $\theta_o = \pi/2$ since the bracketed quantity in the numerator vanishes here (no even parity modes can be accommodated by an infinitely thin sheet). Also by inspection of the figures, the antisymmetric modes converge on ω_p for all values of k, exactly analogous to the planar slab in the limit of $a \to 0$. Second, in the limit $\theta_o = 0$, the hyperboloids close up to a volume and $\omega_k^m = \omega_p$; surface and volume modes cannot be distinguished. Third, in the limit of large k the surface plasmon frequency converges on $\omega_p/\sqrt{2}$, the planar limit; Figs. 14 and 15 show this very clearly. This can be further seen by taking the large k forms of the kegelfunctions (Becker, *et al.*, 1981a). One finds, for $k > m$ and $k >> 0$

$$\frac{{\omega_k^m}^2}{\omega_p^2} \sim \frac{1}{2}\left[1 \pm e^{-k(\pi-2\theta_o)}\right] \tag{II-120}$$

entirely analogous to the planar dispersion, Eq. (II-80). [Note that $\pi - 2\theta_o$ is the opening angle of the hyperboloids, 2ψ, and the cross sectional thickness of the hyperboloid $b \approx 2r \sin\psi \approx r^2\psi$ for small ψ, and we have

$$\frac{{\omega_k^m}^2}{\omega_p^2} \sim \frac{1}{2}\left(1 \pm e^{-\frac{k}{r}b}\right); \tag{II-120a}$$

the k-vector is reduced as the radius goes to infinity.] If k is proportional to the surface plasmon wave vector at point $\vec{r}$, the expression in Eq. (II-120) represents the small wavelength limit. In this limit, the local surface radius of curvature is much less than λ_{sp} and the hyperboloid resembles a plane. A fourth point to be made is that the dispersion relations group in a small cluster of eigenfrequencies near the value $\omega_p\sqrt{2}$ for nearly all values of k near $\theta_o = 60°$ (Figs. 12 and 16). In Fig. 14 it can be seen that the plot of ω vs k for $\theta_o = 60°$ is nearly flat. Since the group velocity is defined as

$$v_g = \frac{\partial\omega}{\partial k} \tag{II-121}$$

and characterizes the energy transport of the waves, the near zero slope for the dispersion relation at $\theta_o = 60°$ suggests formation of a standing wave in the wave packets and indicates a resonance phenomena may occur in this particular geometry. While it is true that the above treatment is carried out in the nonretarded limit and damping is ignored, this should introduce only a small damping term in the interaction Hamiltonian for a good free-electron material. Transitions involving the surface plasmon field can be approximated to first order as:

$$T \cong \frac{2\pi}{\hbar} \int dk_\phi \int dk_r \; |\langle f|A|i\rangle|^2 \; \delta(E_f - E_i) \tag{II-122}$$

where k_ϕ is the azimuthal moment m/r and k_r is the radial momentum, while A is the particular interaction potential with respect to the desired transitions relating initial state $|i\rangle$ and final state $|f\rangle$.

Let

$$dk_r = \frac{d\omega}{\partial\omega/\partial k_r} = \frac{d\omega}{v_g} \qquad \text{(II-123)}$$

be substituted in the radial integration. Then the transition rate T can be written as:

$$T \cong \frac{2\pi}{\hbar^2} \int dk_\phi \int d\omega \frac{|\langle f|A|i\rangle|^2}{v_g + i\gamma} \delta(\omega_f - \omega_i) \ . \qquad \text{(II-124)}$$

For small damping, γ, the vanishing of the group velocity indicates a resonance in transitions involving the surface plasmon field.

III. EXPERIMENTAL DEVELOPMENT

The apparatus used in an investigation of the forces between charged particles and macroscopic media depends on the agents used to probe the force field (electrons or ions), the method by which an interaction is to be observed (energy loss, angular or spatial deflection, photoemission, etc.), and the nature of the medium itself (solid, crystalline, liquid). In this work it was desired to probe the EM fields produced by surface plasma oscillations. Due to the relatively weak coupling between the radiation field and the surface plasmon field, it was decided to excite the plasma oscillations with the moving Coulomb field of a charged particle; electrons were chosen due to the ease of creation and manipulation of a monochromatic, monodirectional electron beam as opposed to an ion beam. By using an electron spectrometer to assess the energy distribution of the emerging electron beam, the presence of surface plasmon excitations can be ascertained; hence the method of excitation also serves as the vehicle for detection in contradistinction to detection of the relatively weak cathode luminescence imparted by the decay of the surface plasmon to the radiation field. Since the surface plasmon field extends a characteristic distance v_e/ω_p into the vacuum, for plasma energies of a few eV and electron energies of 100 to 1000 eV, the probe particle must approach the media within a distance of the order of 100 Å. It was decided to localize the particle-surface proximity by passing the incident electrons through cylindrical channels in a metal foil with diameters of the order of the plasmon field decay length. The apparatus thus consisted of an electron gun, a foil target containing the microchannels, an energy dispersive detector, a vacuum system enclosing the active devices, support electronics for data acquisition, and a Helmholtz coil cage to minimize the ambient magnetic fields (Fig. 20).

A. Environmental Control

In this section the vacuum system, its pumping, and the Helmholtz coil magnetic field compensation system will be discussed.

The vacuum system was a stainless steel bell jar, manufactured by the Perkin-Elmer corporation's Ultek Division, with an inside diameter of 17 3/4 in. and an inside height of 30 in., and was fitted with CFF-flanged ports at levels 7 and 23 in. above the base plate. Pumping was provided by a Perkin-Elmer Ultek differential ion pump with a capacity of 220 torr-ℓ/s for high vacuum, with roughing done through sequential use of two Ultek molecular sieve sorption pumps. The vacuum environment was therefore free of contamination from the pumping system. A draw-back of the ion pump is its production of medium energy (up to 5.5 keV) ions contributing to the background for detectors sensitive to charged particles. For this reason a liquid nitrogen cold trap was used to maintain the system vacuum during data acquisition while the ion pump was heavily baffled with its gate valve. Base pressure observed with this system during periods when the electron gun was inactive was 2×10^{-8} torr, while during acquisition periods the pressure ranged from 7×10^{-8} to 1.5×10^{-7} torr.

The three-axis Helmholtz coil system formed a cage 2.5 m across, providing a field-free region about 0.5 m in diameter at the center of the coil cage. This point was arranged to concide with the center of

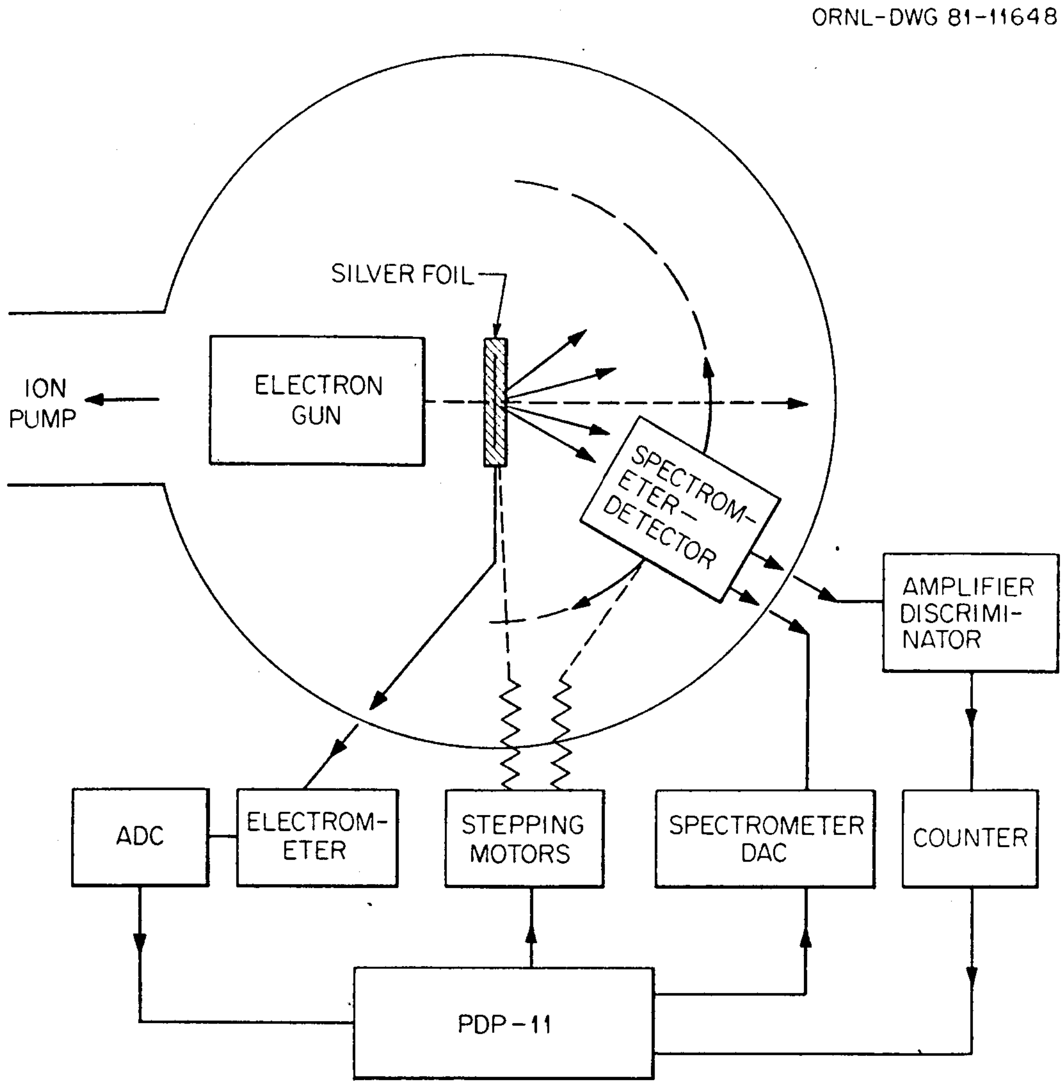

Figure 20. Diagram of the Experimental Set-Up Showing the Relative Positions of the Electron Gun, Foil Targets, and Spectrometer and the Block Schematic of the Data Acquisition System.

the electron beam line to ensure the lowest possible field fluctuations. The field at the center of the system was monitored by three RFL Industries Model 101 flux-gate magnetometers positioned at an offset of 0.3 m from the vacuum system and coil cage center line. The signals from the magnetometers were coupled to the power supplies generating the coil currents through an analog feedback circuit; this served to minimize the DC magnetic fields. The observed response time of the system was about 1 s, and the DC fields were held to 100 μG. The complete enclosure of the electron optics by the stainless steel vacuum tank provided AC magnetic shielding; the observed AC field was 150 μG at 60 Hz.

B. Electron Gun

The electron gun used on this experiment was of conventional design. It consisted of a resistively heated tungsten filament, a collector lens, an einzel lens for spatial focussing and low-energy tail minimization, a final acceleration lens, and two pair of steering plates for fine control of the beam aiming (Fig. 21).

The electron gun was supported by two glass rods sitting in grooves in a machined aluminum block cantilevered on a 6.0-in. CFF flange. Two BNC-type high-current feedthroughs and an eight-connector low-current feedthrough were mounted on the flange for electrical connection to the electron gun. Since the metal-to-metal seals were Kovar, a magnetic material, the feedthroughs were mounted on an 18-in. standoff to remove them from close proximity to the electron beam line. The aluminum support strut was configured on the flange to place the axis of the electron gun co-linear with the flange axis; this arrangement allowed the electron optics to be easily and reliably maintained in alignment with the other devices in the vacuum tank.

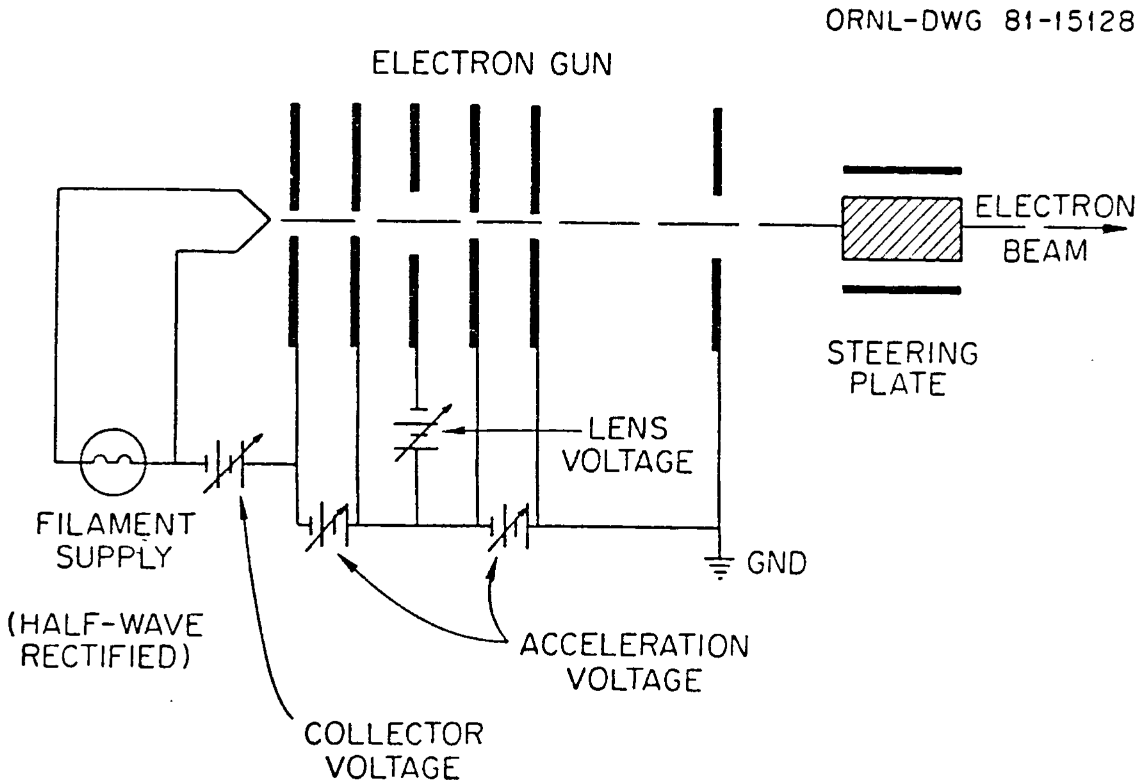

Figure 21. Diagram of the Medium Energy Electron Gun Showing Accelerating, Focussing, and Steering Elements.

In operation, a small positive potential varying from 0.5 to 2.0 V was maintained between the filament and the collector electrode to extract the thermal electrons from the filament. The emission current between the filament and the collector was monitored by the user in the course of data acquisition; for final beam energies of 100 to 1000 eV, typical emission currents were 250 to 700 μA. Once the gun reached thermal equilibrium (after about 45 min of operation), emission currents were steady to within 2%. In the second stage of acceleration, a positive potential of 22 V was maintained between the collector and the outside elements of the einzel lens, while the center element of the lens was biased at a negative potential with respect to the outer elements equal to the total acceleration through this stage minus 0.5 V. For example, for a first-stage acceleration of 2 V and second stage of 22 V, the center electrode would be biased at -23.5 V. This configuration served to both focus the emerging beam and to limit the low energy tail of the emission peak to about 0.5 eV. A final acceleration to the operating energy was made using a positive bias between the einzel lens and the final electrode. The final electrode was grounded to the body of the gun. The beam energy was then $V_C + V_L + V_A$. Operating with the filament saturated at about 3000 K°, a thermal broadening of about 0.6 V is expected. Typical beam profiles are shown in Fig. 22. Note that as the total beam energy increases beyond 500 eV, the FWHM of the energy profiles show a high side asymmetry which is believed to be due to field penetration of the einzel lens electrode to some extent and the spectrometer preretarder to a much greater extent. In his excellent treatise on electrostatics, Durand (1966) shows that field penetration of the

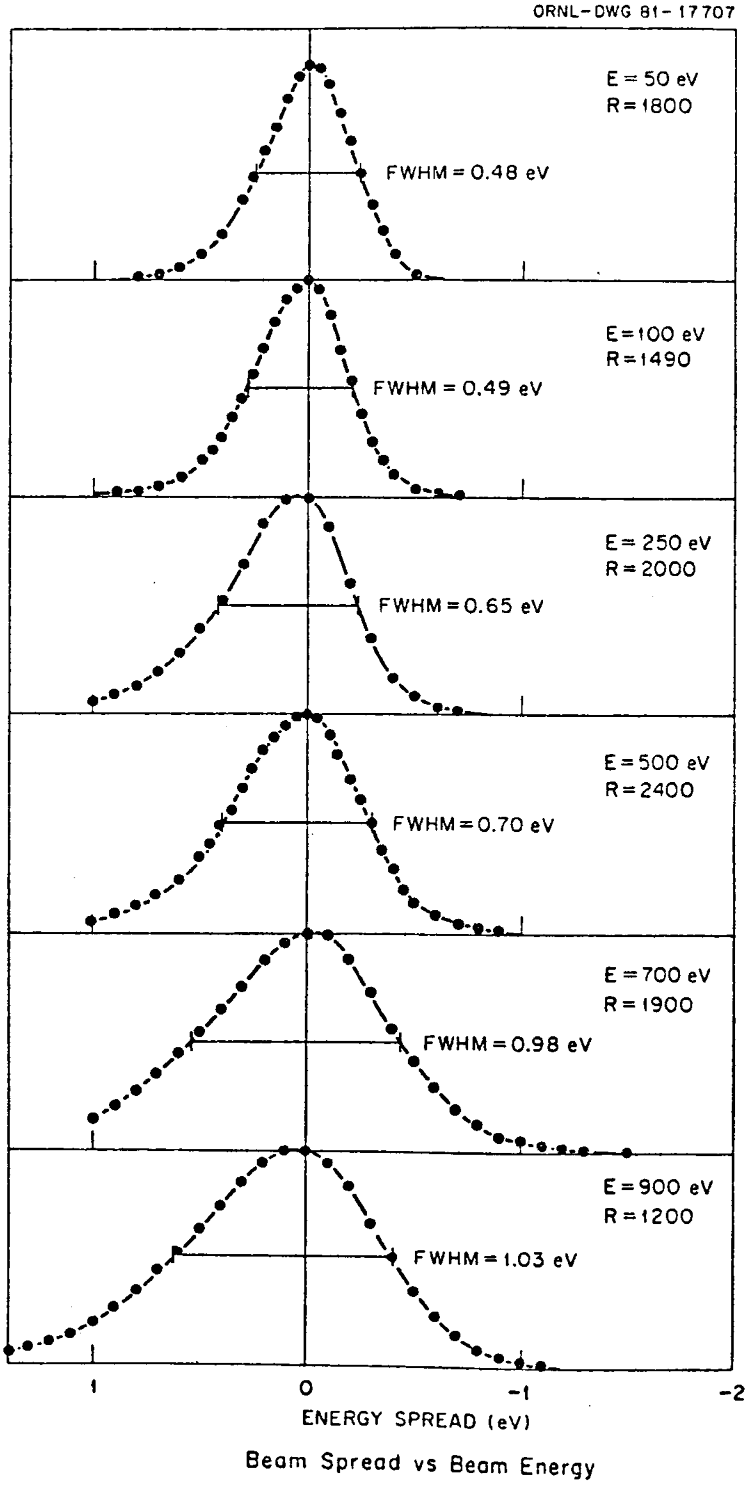

Figure 22. Incident Electron Beam Spread versus Beam Energy Showing Degradation of Line Width with Increasing Energy and the Measured Signal Rejection at the -3.5-eV Point.

order of a few percent on the center line of the apertures would not be unlikely, with extension in the direction of the electron beam of two- to three-aperture diameters (Durand, tome iii, p. 412).

In practice, angular spreads of one to three degrees were observed, decreasing with increasing beam energy approximately as 1/E.

C. Electron Spectrometer-Detector

After some intensive experimentation with several types of charged particle electrostatic spectrometers including stopping potential, cylindrical mirror, Bessel box (Allen, *et al.*, 1976), a design based on the concentric hemispherical mirror described in the literature (Warmack, *et al.*, 1978; Siegbahn, 1967) was settled on (Fig. 23). The hemispherical design was chosen for its large solid angle of acceptance, its resolution, and its superior spurious signal rejection properties. Magneto- and electromagnetostatic designs were rejected since they would introduce a magnetic field near the beam line negating much of the effort to eliminate stray fields with the Helmholtz coil cage. An inherent drawback of purely electrostatic spectrometers is their analysis of only the longitudinal component of the particle momentum; transverse momenta are unchanged and tend to decrease the rejection, limit the acceptance, and reduce the resolution of the spectrometer. The double hemisphere design provides a multiplicity of great circle trajectories in a $1/r^2$ electric field, in effect double focussing at the nadir of the trajectories and increasing the entrance solid angle of the system without drastically degrading the performance.

The relation between the potentials applied to the hemispheres and the pass energy of the orbit is

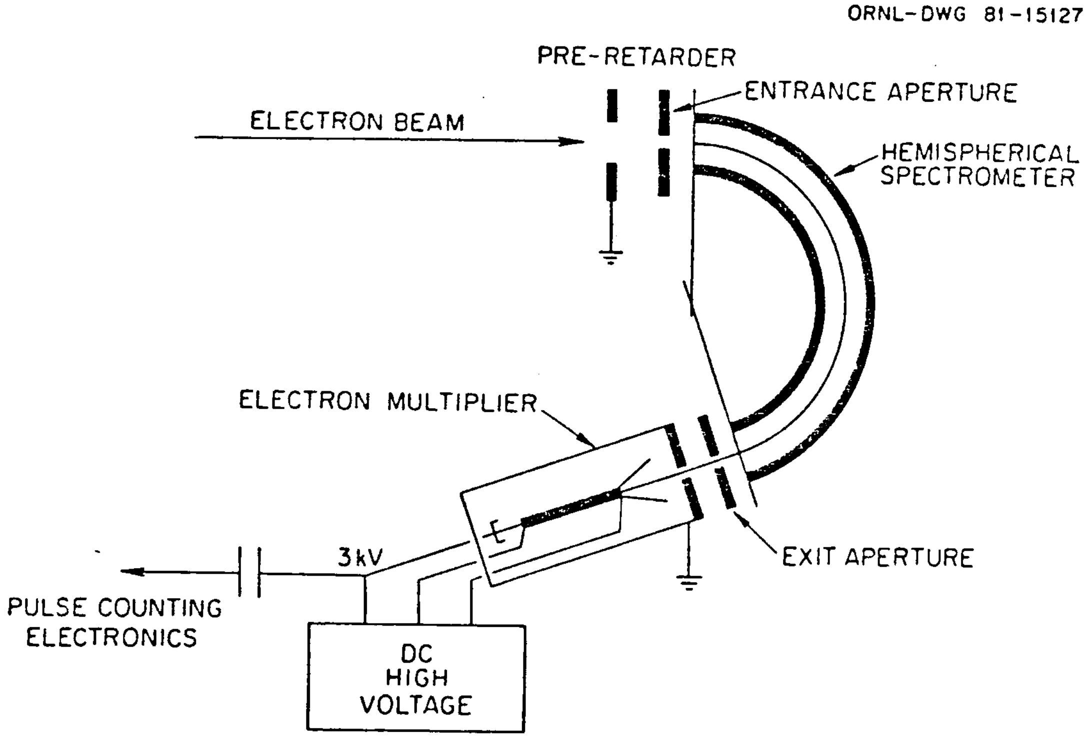

Figure 23. Schematic of the Electron Spectrometer Showing Preretarder, Focussing Electrodes, and Electron Multiplier.

$$\Phi = \frac{1}{2}\,\frac{v_2 - v_1}{r_2 - r_1}\,\frac{r_1 r_2}{r} \tag{III-1}$$

where r_1 is the radius of the inner hemisphere, r_2 the radius of the outer hemisphere, v_1 and v_2 their respective potentials, while r is the radius of the orbit in question. Taking the orbital radius to be the midline, $r = (r_1 + r_2)/2$, the pass energy is

$$\Phi = (v_2 - v_1)\,\frac{r_1 r_2}{r_2^2 - r_1^2}\ . \tag{III-2}$$

The first order energy spread as a function of radius is (Siegbahn, 1967)

$$\frac{\Delta\Phi}{\Phi} \approx \frac{\Delta r}{4r}\ . \tag{III-3}$$

Calculation of the electrostatic potential at the midline orbit and adding this to Eq. (III-2) gives for the total pass energy:

$$E_{pass/q} = \frac{v_1 r_1^2 - v_2 r_2^2}{r_2^2 - r_1^2}\ . \tag{III-4}$$

When the inner electrode is grounded, (III-4) simplifies to

$$E_{pass/q} = v_2\,\frac{r_2^2}{r_2^2 - r_1^2}\ . \tag{III-5}$$

For the hemispheres used, $r_1 = 3.25$ cm; $r_2 = 4.05$ cm; $v_1 = 0$; $v_2 = -6.2$ V; Δr, the radius of the entrance and exit aperture, = 0.10 cm. We find that $\Phi = 13.92$ V, $E_{pass/q} = 17.36$ V, $\Delta\Phi/\Phi = 0.0073$, and the energy resolution at this pass energy is about 0.1 V. The hemispheres are set with a nominal bias of 6.2 V, and the entire hemisphere assembly was floated to reach the desired energy by use of a single, 0.318-cm, preretarding aperture in front of the entrance pinhole. In practice, this arrangement produced a pass energy of 17 V, a resolution of 0.1 to 0.2 eV, and, with all electrodes coated with a graphite layer, a signal rejection ratio of 2000:1 at a distance of 3.5 V from the pass energy.

At the exit aperture of the hemispheres, the transmitted electrons were detected with a Galileo Electro-Optics Model CEM-4039 continuous dynode electron multiplier with integral anode cap, configured in the pulse counting mode. The multiplier was mounted in a grounded, aluminum compartment with an 0.254-cm entrance aperture aligned with the exit aperture of the spectrometer and three 0.635-cm holes around the anode for pumping. The signal from the anode, biased at 3200 V, was capacitively coupled through an RC network with a time constant of 10 μs and a capacity yielding a pulse height of 20 mV at a multiplier gain of 10^8.

The entire spectrometer-detector assembly was enclosed in a grounded, aluminum box, with entrance aperture for the electrons and electrical feedthroughs for the spectrometer bias and electron multiplier. This assembly, in turn, was attached to a swing arm rotating about the axis of the foil target (Fig. 20), allowing selective analysis of all parts of the scattered electron distribution.

D. Foil Target Fabrication and Mounting

The fabrication of the microchannel targets evolved from techniques developed in earlier investigations (Spears, *et al.*, 1979; Birkhoff, *et al.*, 1980) in which low energy electrons ($\lesssim$ 20 eV) were scattered from single pinholes from 2 to 20 μ in diameter. Here, the holes were made singly by vaporizing the foil with a high-powered laser beam. Several drawbacks are endemic to this method. First, it is extraordinarily time-consuming to make an array or pattern of holes since doing so necessitates repositioning either the foil or the beam for each hole, with a required precision of microns. Second, electron micrographs show that the laser vaporization strains the thin foil to the extent that it develops cracks and fissures extending through the foil from successive laser shots. Third, the laser beam can only be focussed to a spot size of the order of the radiation wavelength; for optical radiation, this is the order of several thousand angstroms. Moreover, a recent study (Boye, 1980) showed that for very small holes, the diameter is determined more by the laser power than by the beam focus, since the intensity distribution is Gaussian. It was found that the smallest holes that could be made in practice by this method were about 0.8 μ, about 20 times greater than that required to effectively probe the plasmon field.

An alternate method of fabrication is to replicate grating patterns etched in photo- or electronresists made by either holographically recombining a laser beam in a prism (Shank and Schmidt, 1973), or by using a well-focussed electron beam to expose an electron resist in a predetermined array pattern (Little, *et al.*, 1980). Using photolithography, the smallest resolvable structures are of the order of 1000 to 2000 Å, while electron lithography has reached 800 to 1000 Å. The lower limit of the electron lithography reaches the upper limit of the surface structure size required to produce a measurable surface plasmon interaction and could serve as a production method for submicron structures.

A third method available, and the one that was ultimately used, is to employ the surface replication methods of lithography on an existing material containing many small channels. Such a substrate is one of the polycarbonate membrane filters used in molecular biology studies such as recombinant DNA. These membranes, made by etching high-energy particle track damage, are commercially available under trade names such as Unipore, Nucleopore, and Millipore. They are available in channel sizes of 150 Å up to 10 μ, with aperture densities of up to $3\text{x}10^6/\text{cm}^2$. Thus, successful replication of the membrane surface could yield aperture localizing incident particles to within 75 Å of the surface. The ability to replicate very small-scale structures is limited by the minimum foil thickness required for self-support, a function of the bulk mechanical properties of the material. High malleability metals such as silver and gold are capable of much thinner foils than lighter materials such as aluminum and magnesium. Thin foils are required, since the micropores tend to be filled in by the metal deposition process. Experimentation indicated that the foil thickness had to be about one-half the aperture diameter or less in order to avoid significant fill-in problems. On the other hand, the minimum self-support thickness for crack-free silver foils is about 300 to 400 Å. The channels in the foil can then be reduced in size by evaporating additional metal at a large angle of incidence while the foil is rotated about its normal. This causes the channel walls to fill in unevenly in a conical fashion given by

$$\Delta\ell = \Delta'\ell \; \frac{\tan\Theta}{\pi} \left(1 - \frac{z^2}{4a^2} \tan^2\Theta\right)^{\frac{1}{2}} \qquad \text{(III-6)}$$

where a is the cylinder radius, Θ the angle of incidence, z the depth in the cylinder, $\Delta\ell$ the sidewall thickness, and $\Delta'\ell$ the amount evaporated. A schematic of this deposition process is shown in Fig. 24, bearing marked resemblance to actual aperture cross sections shown in the electron micrograph in Figs. 25 and 26. In principle, the holes can be filled in to an arbitrarily small diameter; in practice, the evaporated silver tends to form microstructures with lateral extents of 100 to 200 Å producing an inherent roughness limiting aperture sizes to 300 Å or so with this technique.

The sequence of fabrication is as follows: a section of polycarbonate membrane with channels 800 to 1000 Å in diameter has 500 Å of silver evaporated onto it at oblique incidence to limit the depth penetration, forming a continuous, crack-free foil; the polycarbonate base is then dissolved away with a halogenated hydrocarbon such as chloroform; a second evaporation is performed at a large angle of incidence to the foil while it is rotated; the foil is then cleaned with fresh chloroform and freon, cut into 0.5-cm sections, inspected for defects such as cracks and blisters, and then mounted on a target holder (Fig. 27).

Using the above technique, silver foils were fabricated containing microchannels of 500 ± 80 and 1000 Å ± 100 diameter in 1000-Å-thick foil. The size distribution of the holes was determined with a Zeiss Novascan 30 scanning electron microscope capable of 100 to 150 Å resolution. A micrograph of the 500 Å channels is shown in Fig. 28. It can be seen that the microchannels are relatively uniform and that the silver tends to aggregate in the foil in structures of the order of 100

ORNL-DWG 81-15130

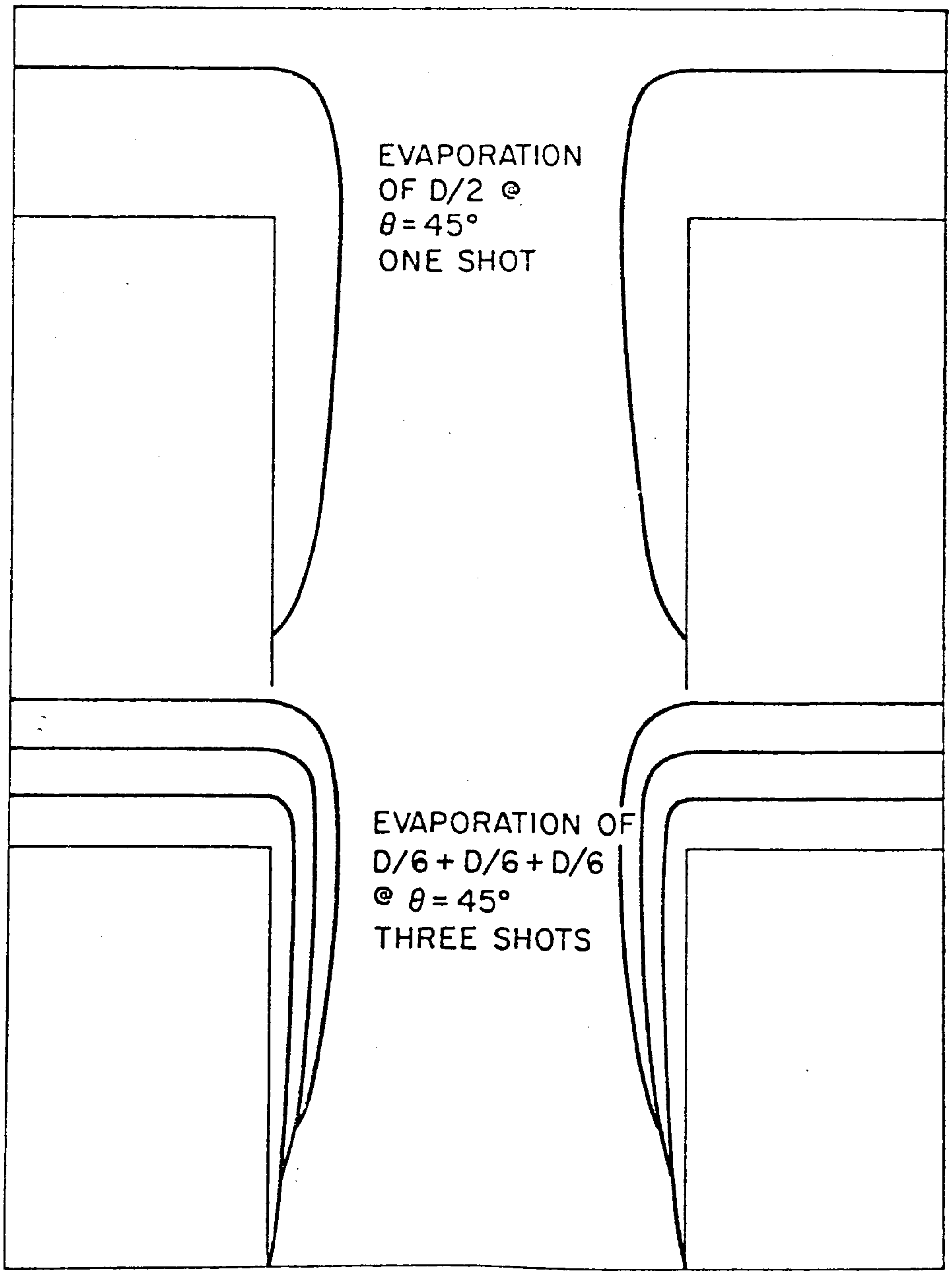

Figure 24. Cross Section of the Channel Formation Process Showing the Calculated Cross Section for One Evaporation and the More Realistic Cross Section for an Equivalent Material Thickness Spread over Three Evaporations.

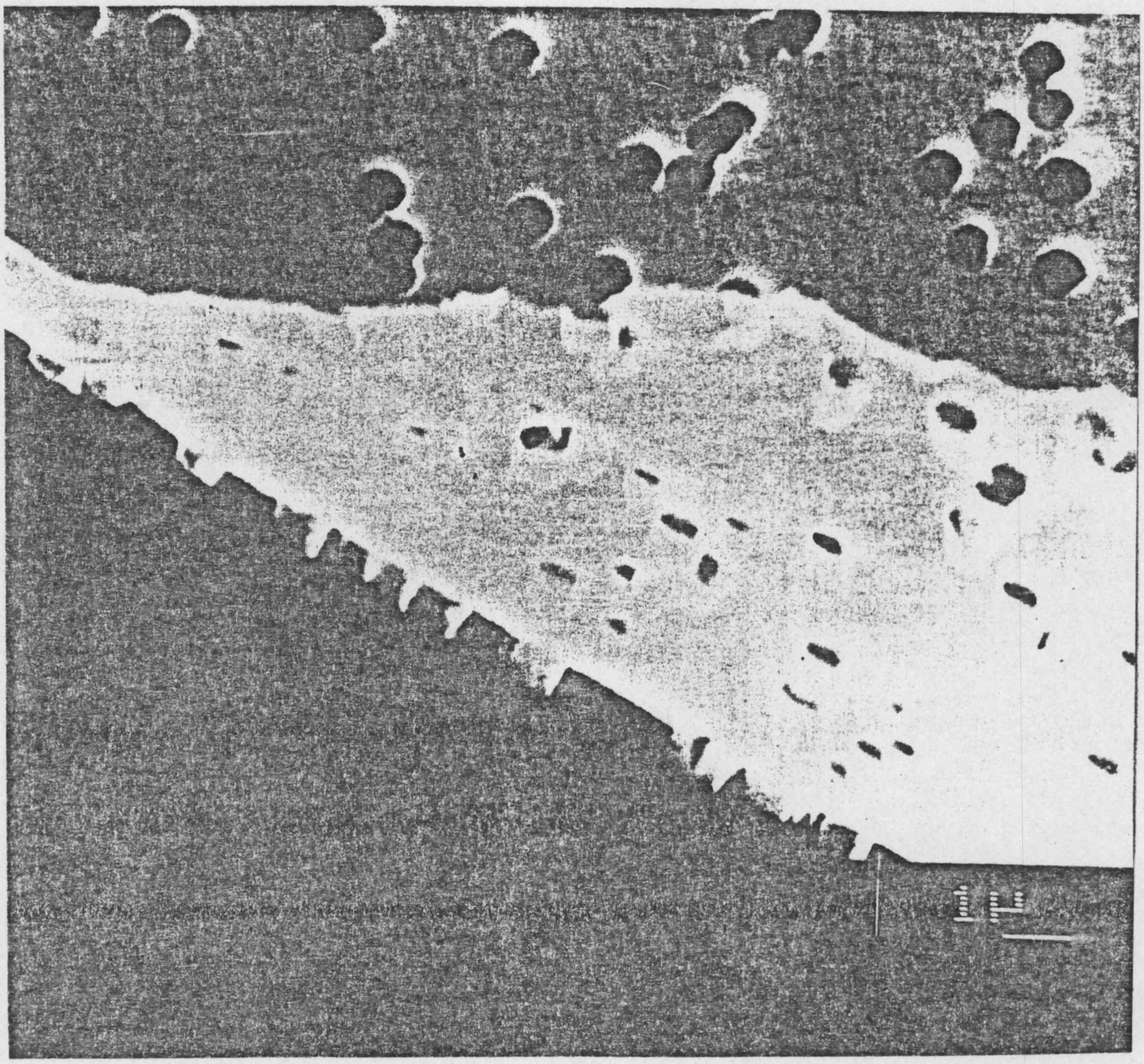

Figure 25. Scanning Electron Micrograph of a Silver Foil Replica Showing the Wall Sections Resulting from Evaporated Material Penetration on 6000 Å Apertures.

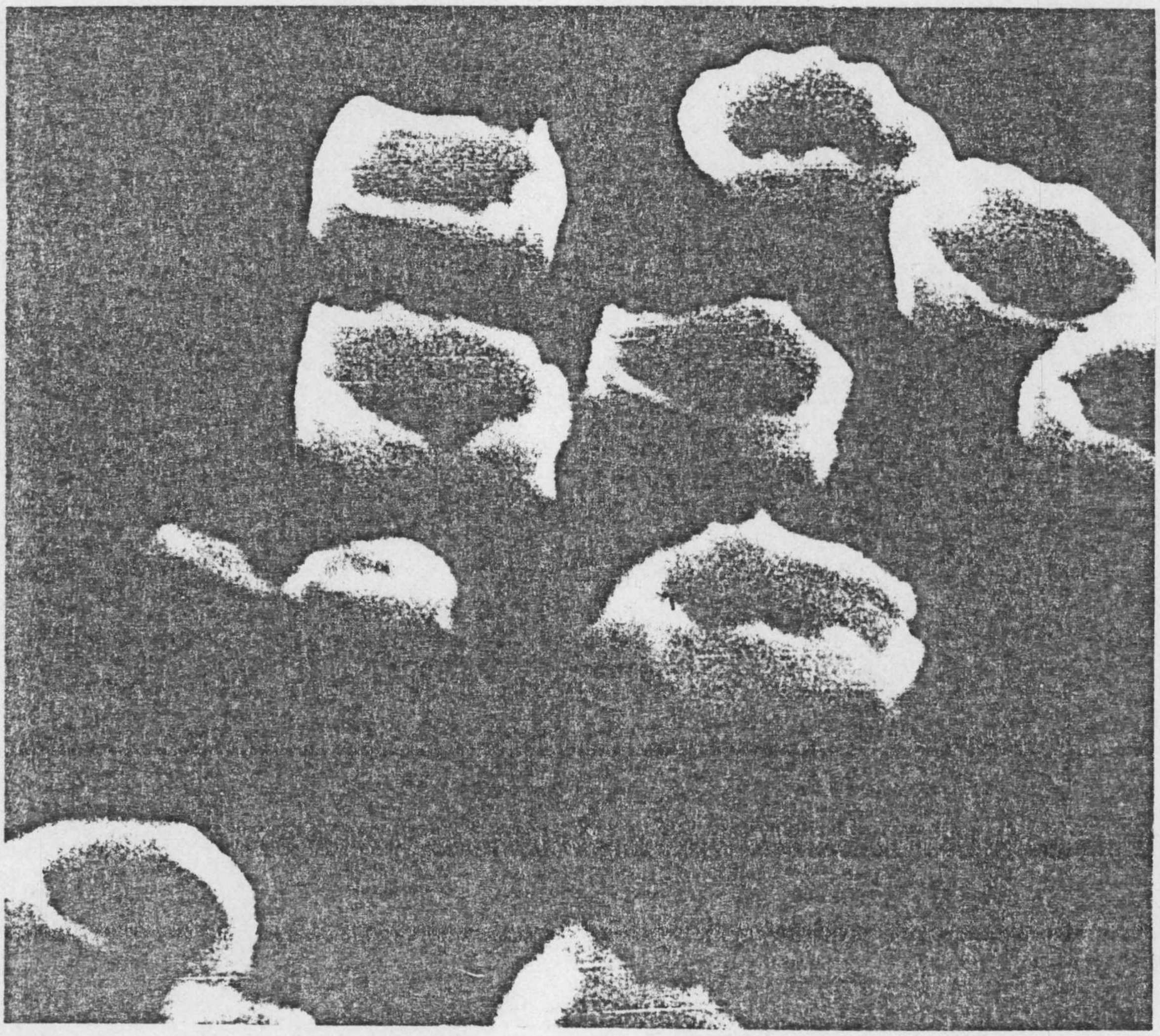

Figure 26. Scanning Electron Micrograph of the Membrane Side of a Silver Foil Replica Showing the Relative Thickness of the Wall Penetration.

ORNL-DWG 81-15129

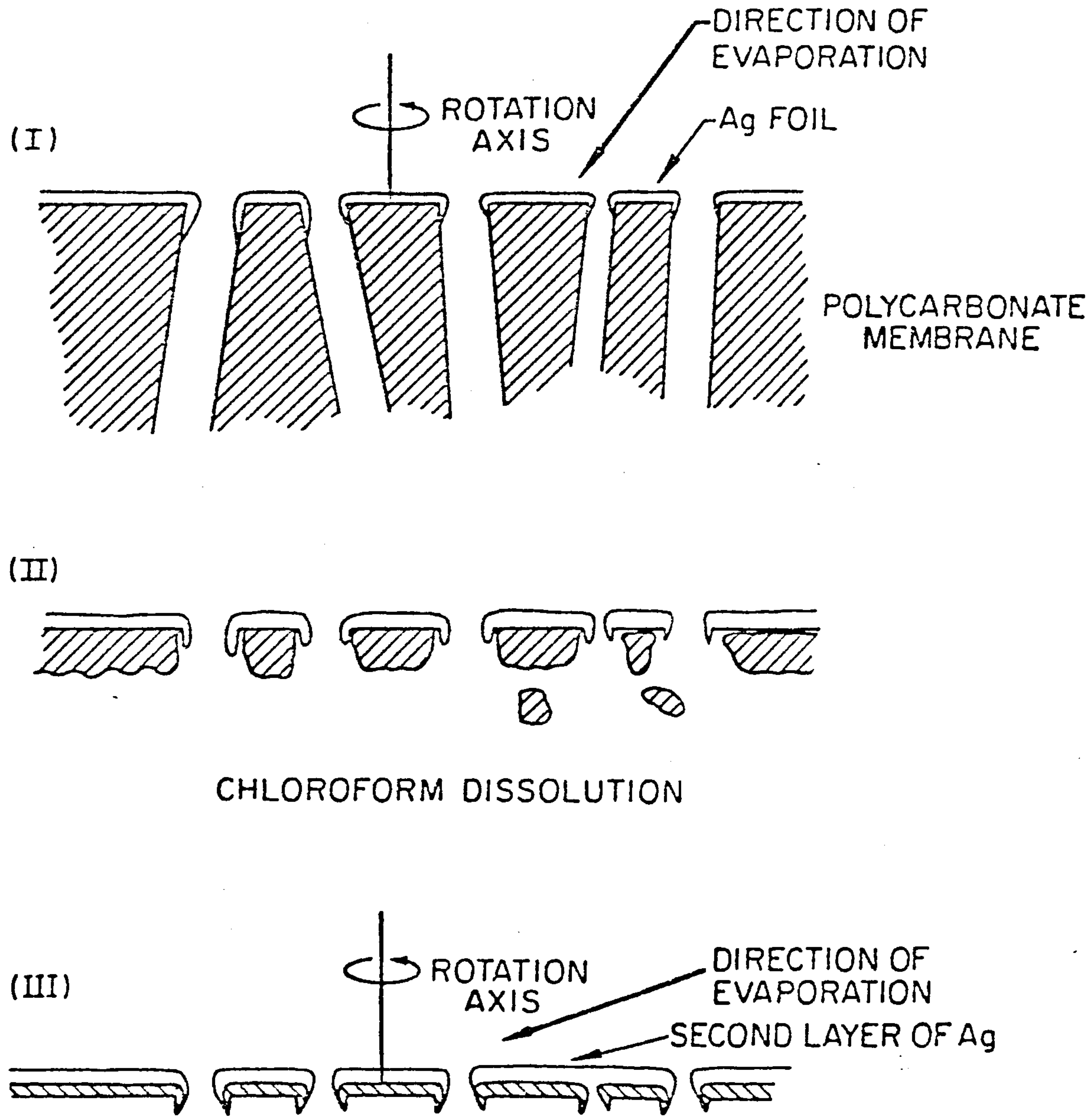

Figure 27. Schematic of the Replication Process from the Initial Support Foil Made by Rotating Evaporation (I), the Removal of the Membrane Backing (II), and Filling-In of the Apertures with a Second, High-Angle Evaporation (III).

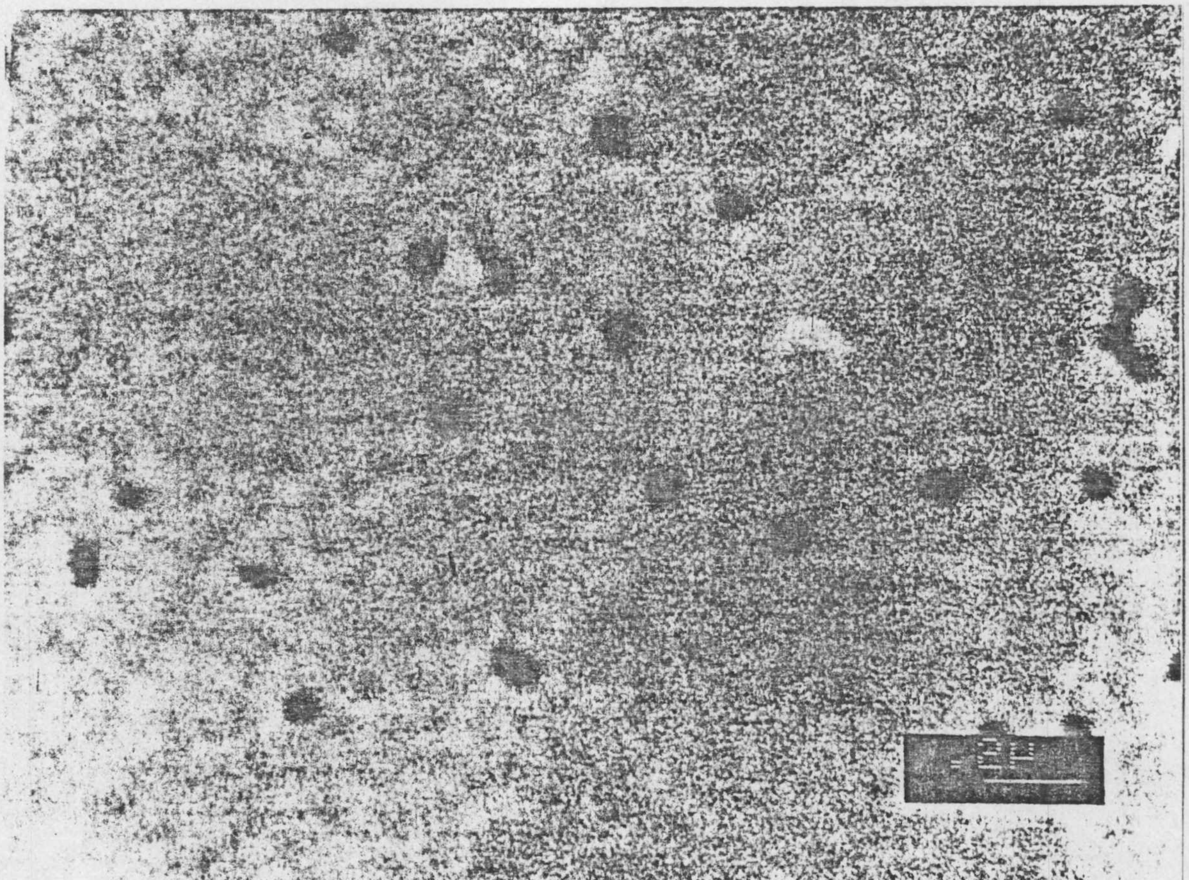

Figure 28. Scanning Electron Micrograph of the Silver Foil Targets Showing the Typical Microcrystal Grains and Representative Channels of about 500 Å in Diameter. The micrograph was taken with a Zeiss Novascan 30 using a beam energy of 15 kV and an indicated magnification of 48,000. The scale line is 2000 Å long.

to 200 Å in lateral extent. Due to the inherent roughness, it is felt that 300 Å is the limit of this technique.

The foils were supported on 100 lines per inch, 85% transmitting, copper mesh, available from Buckbee Mears; the mesh, in turn, was affixed to a copper disk containing a 1-mm aperture using conducting silver paste. The available effective area was then 0.67 mm square and contained about 20,000 holes. The copper disk was affixed to an aluminum carrier bar which was capable of supporting up to six targets in a vertical file, allowing several different sets of apertures to be analyzed without breaking vacuum. The bar was held by an electrically isolated arm, enabling the target current to be monitored by an electrometer. Mechanical feedthroughs to the bar holder were made in such a way as to allow both vertical translation of the bar holder, bringing different targets into play and allowing rotation about a vertical axis, enabling the beam incident angle to be set arbitrarily.

E. Computer Data Acquisition

The energy-loss calculations of Chapter II, Eqs. (II-53), (II-58), and (II-79), all indicate a stopping power of about 4 eV/cm for a 100-eV particle translating axially in a 500-Å-diameter silver cylinder; this gives an approximate transition rate of about 1×10^{-5} for a cylinder 1000 Å in length. Such tiny transition rates would be extremely difficult to observe directly even with very sensitive spectrometers and detectors; random environmental fluctuations in magnetic fields, beam trajectories, and beam current and energy would mask the data as long integration times would be required in order to build up reliable statistics. A method of data acquisition is required that tends to minimize competition from random sources while maintaining positive control of the active elements in the apparatus. For these reasons a small digital computer was employed to coordinate the acquisition process. For reasons of programming ease, cost, and hardware interface, a Digital Equipment Corporation PDP-11/03 with 32 k-words of memory running under DEC's RT-11 single-user operating system was selected. This machine is sufficiently fast and sophisticated to enable a large variety of computational analysis to be done on the data in addition to data acquisition.

When interfaced to devices such as analog-to-digital converters (ADCs), digital-to-analog converters (DACSs), and contact closure switches, the digital computer is capable of acting upon analog signals, communicating with analog equipment using analog signals, and detecting the occurrence of an event. The strengths of the machine are its speed, its repetitive precision, its ability to store large amounts of information, its ability to display information in a meaningful fashion, and the ease with which data acquisition procedures can be altered by reprogramming. The weakness of the machine lies in its inherent difficulty in differentiating extraneous information from meaningful information, even with the aid of quite sophisticated programs; the computer is a serial processor and acts on relatively small amounts of information at a time. It is important to arrange the computer's interface with the analog and digital real world in a fashion that plays up to the machine's strengths and plays down its weaknesses.

The experimental apparatus consisted of an electron gun, a movable foil target, a spectrometer detector with angular positioning and variable pass energy. Secondary devices included ion gauges, electrometers measuring target current, and an ammeter measuring the ion pump current. All of these devices can be controlled by the computer; in practice, several of them present operational difficulties.

The electron gun has a total of ten active signal leads controlling the filament current, lens potential, and steering plates. With the exception of the steering plates, experimentation showed that no simple algorithm existed for the simultaneous maximization of the beam intensity, line width, and signal-to-background ratio at a given set energy. It was decided to monitor the target beam current by reading the gauge of an electrometer with an ADC, alerting the user when large fluctuations were noted. Information on beam current and energy would then be recorded along with the data for later use. Field use showed the target beam current to be stable within 5% with fluctuation periods of the order of tens of seconds.

The spectrometer-detector is a much simpler device than the electron gun. For practical purposes it sinks no current; in operation, the bias across the hemispheres is fixed at 6.2 V, the resolution is independent of energy, and the pass energy is linear in the preretarding voltage. Pass energy can then be varied simply by changing the bias on the preretarder with respect to ground with a DAC. The spectrometer was mounted on a movable swing arm whose shaft was co-linear with the vertical axis of target motion; the shaft was driven with a Responsyn HDM-1600 eight-phase, stepping motor operating through a 1000:1 planetary speed reducer available from Boston Gear. The circuitry controlling the stepping motor coil firing sequence for single stepping was triggered with a negative TTL signal at one or the other of the forward or reverse inputs. Strobing one of these inputs to ground and back while the other is held high by the computer will cause the stepping motors to take one step and swing arm to move a small distance. Since the motor requires 1600 steps to complete one revolution and the motor shaft turns a 1000:1 speed reducer, 1,600,000 steps are required to move the spectrometer through 2π radians; each step is then 3.927 μrad or 0.81 s of arc. These figures are theoretical; in practice, vibration caused by stepping motor firing and the internal backlash of the drive gears did not allow such precision. Backlash upon direction reversal was found to be about 1200 steps, and homing accuracy on one limit switch or another was about 50 steps--absolute positioning for arbitrary motion was about 5 mrad. Two separate origins for the detector position were provided by establishing two electronic limit switches in the swing arm's path. These were simply two Cu electrodes insulated from the vacuum tank (ground) which were held at +5 VDC by a power supply working through an RC network for current limit purposes and switch debouncing. The electrode state was sensed by an inverter gate which was in turn read by the computer stepping motor I/O port. Contact with a switch by the swing arm shorted the gate to ground, interrupting the computer, and the swing arm's absolute position was known to within one step. Position at any given time between the switches was determined by dead reckoning; the large inherent backlash restricted usable angular scanning data acquisition to one direction at a time.

The electron detector was configured to produce a pulsed output. The pulse, about 20 mV, was amplified using a Tennelec TC 213 linear amplifier, passed through a low-level discriminator, and incremented a 12-bit, 10-MHz counter. The external counter is used both to relieve the PDP-11 from pulse counting and to enable a higher data acquisition rate. The maximum practical count rate of the computer is 10 kHz, severely limiting the dynamic range of the data rate. Twelve-bits can record a maximum of 4096 counts, upon overflow the counter interrupts the computer, the overflow is noted, and the counter is reset. Data acquisition is programmed to be terminated either by timing out or by counting out. The total number of counts along with the elapsed time is then recorded by the computer. Timing for this purpose is provided by a DEC KWV11-A programmable quartz crystal clock with speeds ranging from 100 Hz to 1 MHz.

The position and orientation of the target holder was set using two rotary feedthroughs in the vacuum system baseplate. Co-rotation of both feedthroughs gave vertical translation, and counter-rotation produced a rotation about the vertical axis. The holder was fabricated such that the rotation axis coincided with the foil front surfaces and the rotation axis of the spectrometer detector. Both feedthroughs were driven by stepping motors and could be controlled in a fashion similar to the control sequence of the spectrometer. In practice, target position and orientation were not varied during energy loss data acquisition, and target position/orientation was set by the user.

The energy loss signals ultimately measured by the apparatus were fairly weak, approximately one-thousandth of the elastic peak intensity. In addition, the very small pinholes cover only a fractional area of 5×10^{-5} of the target foil; total transmitted intensities were thus small, being of the order of 100 to 400 counts/s in the elastic peaks. Since inherent electron multiplier dark current was 0.1 to 0.5 count/s, random background from the ion pump and other sources contributed about 0.1 to 0.2 count/s, along with the spectrometer rejection of 2000:1; the inelastic signal could claim at best only a 1:1 signal-to-noise ratio with true events accumulating very slowly. Since any window-type spectrometer observes a small part of the loss spectrum at any given time, the real time taken for data acquisition is proportional to the number of channels and resolution required. The result of these factors is that data acquisition periods were of the order of hours in length, but beam current and magnetic field fluctuations occurred on the order of tens of seconds. To eliminate data washout by these fluctuations, the precision and speed of the computer were utilized by dividing the energy window of interest into suitable resolution channels in memory; this window was repetitively scanned, spending only a few milliseconds on each channel, completing a sweep in the order of a second, until sufficient data were accumulated for reliable statistics on the elastic peak, inelastic peaks, and background levels. This information, along with a running monitor of the beam parameters, time of day, position of the spectrometer, and elapsed time, was then recorded on a disk file by the computer as well as being displayed real time in a histogram plot on the console CRT. The machine also kept a running log of all operations and signal levels during the running of the program for later reference and correlation with the data.

IV. DATA AND COMPARISON WITH THEORY

Measurement of the surface plasmon production probability for aloof electrons required careful acquisition procedures in order to render the data unambiguous. These procedures fall into broad categories--elimination of random noise, differential measurement of the signal, minimization of competing processes. Noise levels were limited chiefly through enclosure of the spectrometer detector in a grounded, conducting box, operating the multiplier at the minimum bias (determined to be about 2800 V) to get a consistent cascade, and baffling the ion pump when data were being acquired. In order to maintain the system vacuum when the ion pump was baffled, a liquid nitrogen cold trap was employed; this kept the vacuum at 8×10^{-8} to 1.5×10^{-7} Torr during acquisition. Taking these precautions, the observed background intensity was 0.2 to 0.5 count/s.

It has been previously mentioned that the energy loss data were acquired using a multiple sweeping technique designed to remove anomalies that might arise due to short period fluctuations in the beam current and other random environmental factors. The signal degradation would then result primarily from the system dark current of 0.2 to 0.5 count/s and the 2000:1 signal rejection of the spectrometer. In principle, since the random interference tends to accumulate as $\sqrt{N}$, where N is the number of events, while the true signal builds up linearly in N, a true signal smaller than the dark current can eventually be pulled from the noise by a long period integration. In practice, signals are limited by the ability to keep the electron gun from drifting in energy and smearing the energy loss data and by similar long period secular drifts in the magnetic field compensation system. The practical combination of these factors limits signal detection to signal-to-noise ratios of about 1:1 and inelastic/elastic peak areas to about 0.0005. These parameters give, for a transition probability of 0.001, a minimum signal of 0.2 count/s and an inelastic peak of 200 counts/s. With the low areal coverage of the 470-Å holes of $5x10^{-5}$, the beam current on the foil target should be at least $4x10^{6}$ counts/s, approximately a pico-ampere. The observed target currents were 1 to 4 nA, but the elastic intensities were only 100 to 500 counts/s. The probable reason for this is that the electrometer monitoring target current measures the flux incident on the holder rather than the foil itself and, consequently, has a much higher collecting area than the 0.7 mm^2 of the foil.

In order to ascertain the reality of the energy loss, data were taken on the incident electron beam without foil, the foils were then moved into position, and loss data in the band from 0 to 5 eV were acquired; the same band was used in coverage of the incident beam. In this manner, the FWHM and position of the elastic peak before and after scattering from the foils could be compared, providing a check on voltage drift and focussing drift, and an accurate measurement of the electron beam's tail would be available for subsequent baseline fitting and subtraction. As all of the transition probabilities indicated rates of less than one percent, this was necessary in order to make an accurate measurement of the absolute transition probability.

Using these techniques, energy loss data were accumulated at energies ranging from 50 to 900 eV at stops of 50, 100, 250, 500, 700, and 900 eV. All but the 50- and 100-eV data are shown in Fig. 29 and Table

ORNL-DWG 81-11650

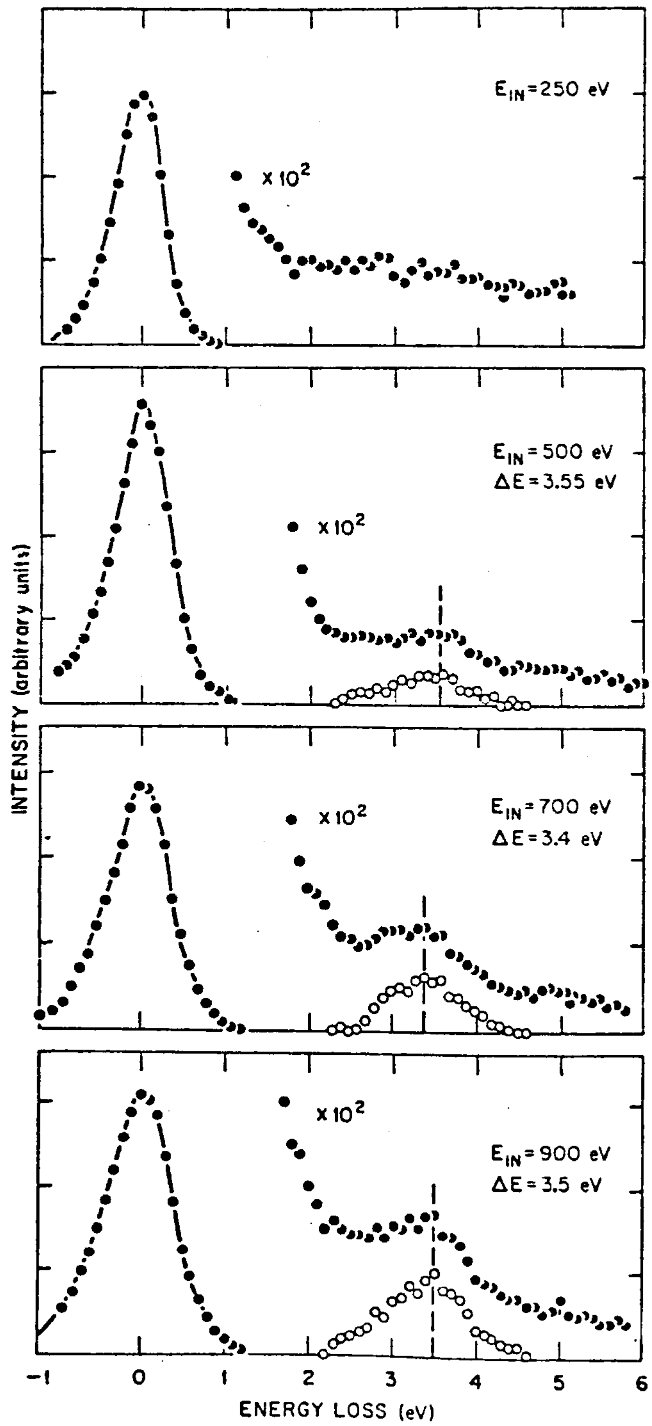

Figure 29. Electron Energy Loss Data for Incident Energies of 250, 500, 700, and 900 eV. The elastic peak is shown on the left for comparison, and the loss points on the right are plotted at 100 times the scale of the elastic peak. The 250-eV data are shown for comparison, since no energy loss can be unequivocably discerned. The open circles are the raw data with spectrometer background subtracted.

I; the 50- and 100-eV data were similar to the 250-eV data which are shown in comparison with the 500-, 700-, and 900-eV data. No discernible losses could be seen in the data at 50, 100, and 250 eV; losses increasing in strength with incident energy were seen at 500, 700, and 900 eV. This can clearly be seen in Fig. 29 where the solid dots are the raw data, while the open circles are the baseline-subtracted data; the elastic peaks are shown for comparison. The calculated transition probabilities in the table are gotten by taking the ratio of the area under the baseline-subtracted peaks to the area under the corresponding elastic peak.

TABLE I

ENERGY LOSS DATA

Energy	FWHM	E-Loss	FWHM	T
100	0.55	-	-	-
250	0.60	-	-	-
500	0.80	3.55	0.90	1.4×10^{-3}
700	0.90	3.40	1.00	2.7×10^{-3}
900	0.90	3.50	0.90	3.5×10^{-3}

This can be compared with the expressions of Chapter II concerning the classical stopping power for charged particles translating near dielectric media and to a similar calculation by Otto (1967) for charged particles translating near a dielectric plane slab. Further comparison can be made to a quantum mechanical calculation (Ferrell, 1981) for the probability per unit length for surface plasmon excitation for a charge translating near a plane slab. All of the theoretical treatments are carried out in the limit of $v \ll c$ and neglecting any hydrodynamical response of the dielectric (single-particle electron-hole excitations are ignored also).

In the case of the semiclassical calculations of Otto, the stopping power for an electron translating with velocity v at distance z above a plane slab characterized by dielectric response $\tilde{\varepsilon}(\omega)$ is

$$\frac{\Delta W}{\Delta X} = \int_{-\infty}^{-\infty} dky \int_{o}^{\infty} d\omega\omega \; \frac{\Delta \underline{P}}{\Delta X} \; (k_y,\omega) \;, \tag{IV-1}$$

where

$$\begin{aligned} \frac{\Delta \underline{P}}{\Delta X} &= \frac{\alpha\hbar c}{\pi v^2} \, \frac{e^{-2k_{\parallel} z}}{k_{\parallel}} \, \mathrm{Im}\left(\frac{\tilde{\varepsilon} - 1}{\tilde{\varepsilon} + 1}\right) \\ k_{\parallel}^2 &= k_y^2 + \frac{\omega^2}{v^2} \;. \end{aligned} \tag{IV-2}$$

Removing the weighting in energy, $\hbar\omega$, in (IV-1) and limiting the energy (frequency) integration to a small domain $(E_<:E_>)$ about E_{sp}, the classical probability of losing energy E_{sp} in a region $(E_<:E_>)$ in a distance dx is

$$\underline{P}_{\Delta X}(z,v) = \frac{2\alpha c}{\pi h v^2} \int_{E_<}^{E_>} dE \; K_o\left(\frac{2Ez}{hv}\right) \mathrm{Im}\left(\frac{\tilde{\varepsilon} - 1}{\tilde{\varepsilon} + 1}\right), \tag{IV-3}$$

where the integration in the transverse component of the surface momentum,

k_y, has been performed. $K_o(x)$ is the modified Bessel function of the second kind, $\tilde{\varepsilon}(E)$ is the complex dielectric response at energy $E = \hbar\omega$, and α is the fine structure constant. This is to be compared with (II-21) for the classical stopping power. By inspection of (IV-3), it can be seen that the probability of plasmon excitation is damped exponentially in Ez/v from the asymptotic form of the Bessel function and is strongly peaked whenever $\varepsilon_2(E)$ is small and $\varepsilon_1 = -1$, traditional characteristics of a strong surface plasmon response.

We can also take the expression for the collective excitation stopping power in (II-27b). Dividing by the plasma energy gives an approximate expression for the surface plasmon excitation per unit length. This gives

$$\frac{P}{\Delta X}(z,v) = \frac{\alpha\hbar^2 cv}{4E_p^3} \frac{\hbar\gamma}{z^3}, \qquad \text{(IV-4)}$$

where $\hbar\gamma$ is the damping (lifetime) of the plasmon resonance. When a Drude dielectric response function such as (II-13) is used for $\tilde{\varepsilon}(\omega)$, (II-3) can be integrated directly, and the expression (IV-4) will be recovered as the leading term--this is a consequence of the fact that (II-26), the $\vec{k}$- and ω-dependent response, will be dominated by the free-electron part for small values of v_F and large values of z.

Classical stopping power calculations can be made for a cylindrical void characterized by response $\tilde{\varepsilon}(\omega)$. Removing the weighting over energy ($k' = aE/\hbar v$) gives for the surface plasmon excitation probability in a region $(E_<:E_>)$ about E_{sp}

$$\underline{P}_{\Delta X}(r,v) = \frac{r\alpha c}{\pi^2 av} \sum_{m=0}^{\infty} \int_{k'_<}^{k'_>} dk' \; \mathrm{Im}\left[\frac{-k'(\tilde{\varepsilon}-1)I_m^2\left(k'\frac{v}{a}\right)K'_m(k')}{k'(\tilde{\varepsilon}-1)I_m(k') - 1}\right]. \qquad \text{(IV-5)}$$

If a Drude response is taken for $\tilde{\varepsilon}(\omega)$, we can modify (II-48a), giving

$$\underline{P}_{\Delta X}(r,v) = \frac{-\alpha\hbar^2 cv}{\pi^2 E_p^3} \frac{\hbar\gamma}{a^3} \sum_{m=0}^{\infty} \int_{o}^{\infty} dk' \; \frac{k' I_m^2\left(k'\frac{r}{a}\right) K_m(k')}{I_m^2(k')K'_m(k')} \qquad \text{(IV-6)}$$

for small values of $v \ll a\omega_p$. This expression bears marked similarity to (IV-4).

Equation (IV-5) can be expanded in regions where the modified Bessel function can be replaced by their asymptotic forms. k' for electron energies of 500 to 900 eV, $E_<, E_>$ about 3.5 eV, and 2a = 500 Å is approximately 8.5, and the asymptotic conditions hold for the Bessel functions. We find

$$\underline{P}_{\Delta X}(r,\, v \ll c) \;\approx\; \frac{i\alpha c}{2\pi^2 rv} \frac{\Delta E}{E_p} \sum_m e^{-(2\omega_{sp} z_c/v)} \; \mathrm{Im}\left(\frac{\tilde{\varepsilon} - 1}{\tilde{\varepsilon} + 1}\right) \qquad \text{(IV-7)}$$

where $\Delta E = \hbar\gamma$, $E_{sp} = \hbar\omega_{sp}$, $z_c = a - r$, and the value of $\mathrm{Im}(\tilde{\varepsilon} - 1)/(\tilde{\varepsilon} + 1)$ is approximately a constant. This expression shows the characteristic exponential damping in both plasma energy and impact parameter and an increasing cross section as the electron energy increases, since the exponential term dominates the 1/v coefficient at medium energies. Equation (IV-5) can also be approximated for small arguments of the Bessel functions; however, this regime is not reached for the micro-structures of this work until E is approximately 100 keV, where the no-retardation condition no longer is valid. Nevertheless, it is felt to be informative to make the small argument expansion of the integral ...; one finds for the excitation

$$\underline{P}_{\Delta X}(r, v \sim c) \; \stackrel{\sim}{\sim} \; \frac{i2\alpha c}{\pi^2 \hbar v^2} \; \Delta E \sum_m \left(\frac{r}{a}\right)^m . \qquad \text{(IV-8)}$$

This shows a transition rate declining as 1/E in the fast electron regime. Taken together, expansions (IV-7) and (IV-8) indicate a maximum transition rate in the neighborhood of 10 to 20 keV.

The theoretical transition probabilities in Eqs. (IV-3), (IV-4), and (IV-5) are shown in Fig. 30. The calculations using (IV-3) and (IV-4) are done for a distance dx of 1000 Å and impact parameters z integrated from 50 to 200 Å. Here the cylinder length was taken to be 1000 Å, and three cylinder diameters were chosen for comparison--400, 470, and 700 Å. The impact parameter z = a - r was area averaged from the cylinder axis to 50 Å from the cylinder wall. In (IV-4), the plasma energy is taken to be 3.77 eV, and $\hbar\gamma$ is taken to be 0.15 eV, both of which were determined by optical data (Hageman *et al.*, 1974). For Eqs. (IV-3) and (IV-5) the frequency-dependent dielectric response is also taken from the DESY optical data, and the region $(E_<:E_>)$ covers the FWHM of the surface plasmon loss at 3.62 eV. The three points plotted with the theoretical curves in Fig. 30 are the 500-, 700-, and 900-eV data from the table, with an estimated error bar of 20 percent from baseline fitting.

The figure shows that the measured plasmon transition probability agrees fairly well with the classical predictions for a plane slab by Otto and Ferrell *et al.* but fall short of the cylindrical calculations

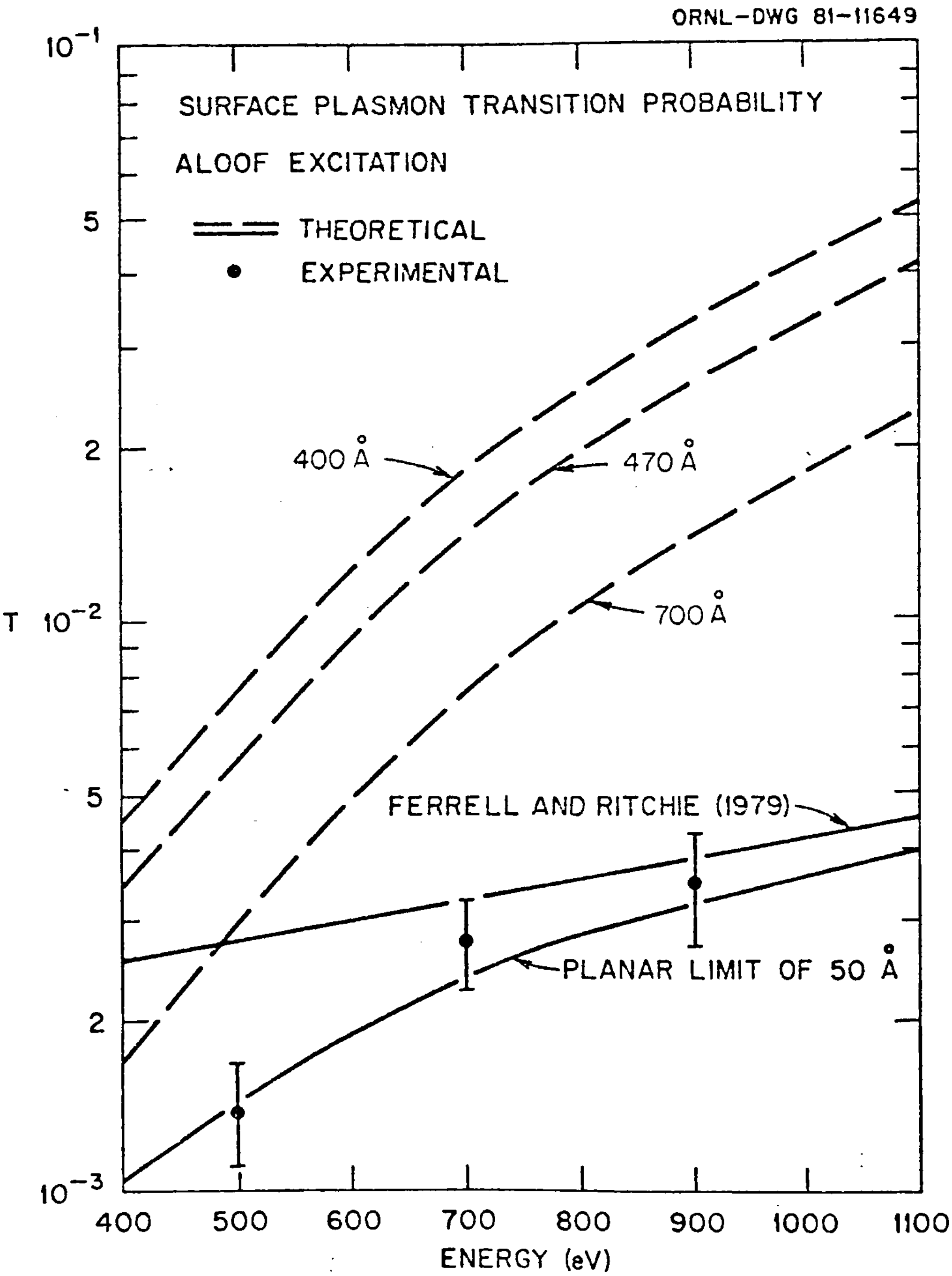

Figure 30. Experimental and Theoretical Surface Plasmon Production Probabilities (T) as a Function of Incident Electron Energy. The upper set of dashed curves correspond to cylinders with diameters of 400, 470, and 700 Å with electron trajectories integrated over radii from 0 to 50 Å from the wall. The lower curves are for an infinite plane slab with impact parameters averaged from 50 to 200 Å. In all theoretical calculations, a characteristic interaction length of 1000 Å was used. The plotted points are the experimentally determined transition rates.

by a factor of nearly five. The classical calculations all assume the dielectric to be of infinite extent, with an effective interaction distance dx of 1000 Å. Scanning electron migrographs and calculations (Figs. 25-27) show the channel cross section to be more or less conical. For this reason it is felt that only 20 to 25 percent of the channel length in this fabrication scheme interacts effectively, since the plasmon field is exponentially damped at the energies used in this study; only a small widening of the order of 100 Å would render the interaction too small to be detected. Evidence for this is evinced by bombarding holes with a diameter of 1000 Å. In this case no discernible losses were seen even though the elastic flux was five to ten times the elastic flux with the small targets. From the rejection of the spectrometer, it is concluded that the transition rate at 900 eV is less than 5×10^{-4}. In addition, the study of the larger channels eliminates grazing incidence wall scattering as a competing process. If present, the transition probability should have been one or two orders of magnitude greater than any inelastic peaks observed, and the dependence of the grazing incidence cross section should have declined as $E^{-1/2}$ (Ritchie, 1968; Bronshtein, 1977; Powell *et al.*, 1960) but did not, a direct conflict with the observed data.

A quantum mechanical derivation of the surface plasmon excitation probability for an electron translating at a velocity v a distance z above an infinite, plane slab has been carried out by Ferrell (1981). This calculation is carried out in the nonretarded limit ($v \ll c$) using a Drude dielectric function for the metal characterized by plasma frequency ω_p and damping γ. The surface plasmon field is described in terms of a harmonic oscillator Hamiltonian, and the interaction of the electron with the plasmon field is considered in terms of a shift in the zero point energy of the free state Hamiltonian. For the probability of creating one surface plasmon of energy in a time $t = \Delta X/v$, he finds:

$$\underline{P}_{10} = A(z,t)\, e^{-A(z,t)} , \qquad \text{(IV-9a)}$$

where

$$A(z,t) = \frac{\alpha\omega_{sp} t}{v/c} K_o\left(2\frac{\omega_s z}{v}\right) - \frac{\alpha\omega_s}{v/c} f(t) \qquad \text{(IV-9b)}$$

and

$$f(t) = \int_o^t dt' \int_{\frac{vt'}{2z}}^{\infty} \frac{\cos\left(2\frac{z\omega_s z}{v}\right) x\, dx}{\sqrt{1+x^2}} . \qquad \text{(IV-9c)}$$

Now t, the interaction time, can be taken as $\Delta X/v$, where ΔX is the length of the slab. The lower limit of the x-integration in (IV-9c) is then $\Delta X/2z$. With ΔX the order of 1000 Å while z is the order of 50 to 100 Å, it can be shown that the term $f(t)/t$ is much smaller than $K_o(2z\omega_p/v)$, and the second term in (IV-9b) can be neglected. In essence, we require the interaction time t to be much greater than $1/\omega_p$, the same requirement made for the classical treatments. Letting $t = \Delta X/v$ and neglecting the f(t) contribution gives

$$\underline{P}_{10} = \frac{\alpha\omega_s c\Delta X}{v^2} K_o\left(\frac{2\omega_s z}{v}\right) \exp\left[-\left(\alpha\omega_s c\Delta X/v^2\right) K_o(2\omega_s z/v)\right] . \qquad \text{(IV-10)}$$

This quantity is shown in Fig. 31 along with the data of Table I. It is interesting to note that (IV-10) shows a maximum in the surface plasmon transition rate for aloof excitations in silver at about 12 keV, the same as suggested by the small argument and asymptotic expansions of (IV-5). For the calculations of Fig. 31 the surface plasmon energy was taken to be 3.63 eV from the DESY optical data.

Another item of note in the data of Table I is the fact that the loss peaks are at 3.4, 3.5, and 3.55 eV, an average of about 3.5 eV. The accepted value for the surface plasmon excitation energy of silver is 3.63 eV, from both high-energy work (Zacharias, 1970) and optical data. Zacharias examined the energy loss incurred by transmission of a 51-keV electron beam through a thin Ag foil, as opposed to the aloof far-field excitations probed in this work. Both Zacharias and the DESY report indicate a lifetime, $\hbar\gamma$, of about 0.15 eV. It is felt that the difference of about 0.1 eV is due in part to a contamination layer (sulphide, dust, or oil) on the foil, since the current apparatus did not have the capability of *in situ* fabrication. Evidence for oxide shifting on Al and Mg reflection loss measurements is in the literature (Powell *et al.*, 1960) and has also been considered theoretically (Stern and Ferrell, 1960). A shift of 0.1 eV is well within the limits of such a mechanism. No unambiguous determination of the excitation linewidth could be made as the incident beam probe had a thermal linewidth of 0.60 eV which was further broadened at the higher incident energies.

Integration in the transition probabilities was terminated at a surface-particle distance of 50 Å since inspection of SEM micrographs of the surface shows granules of the order of 200 Å in lateral extent

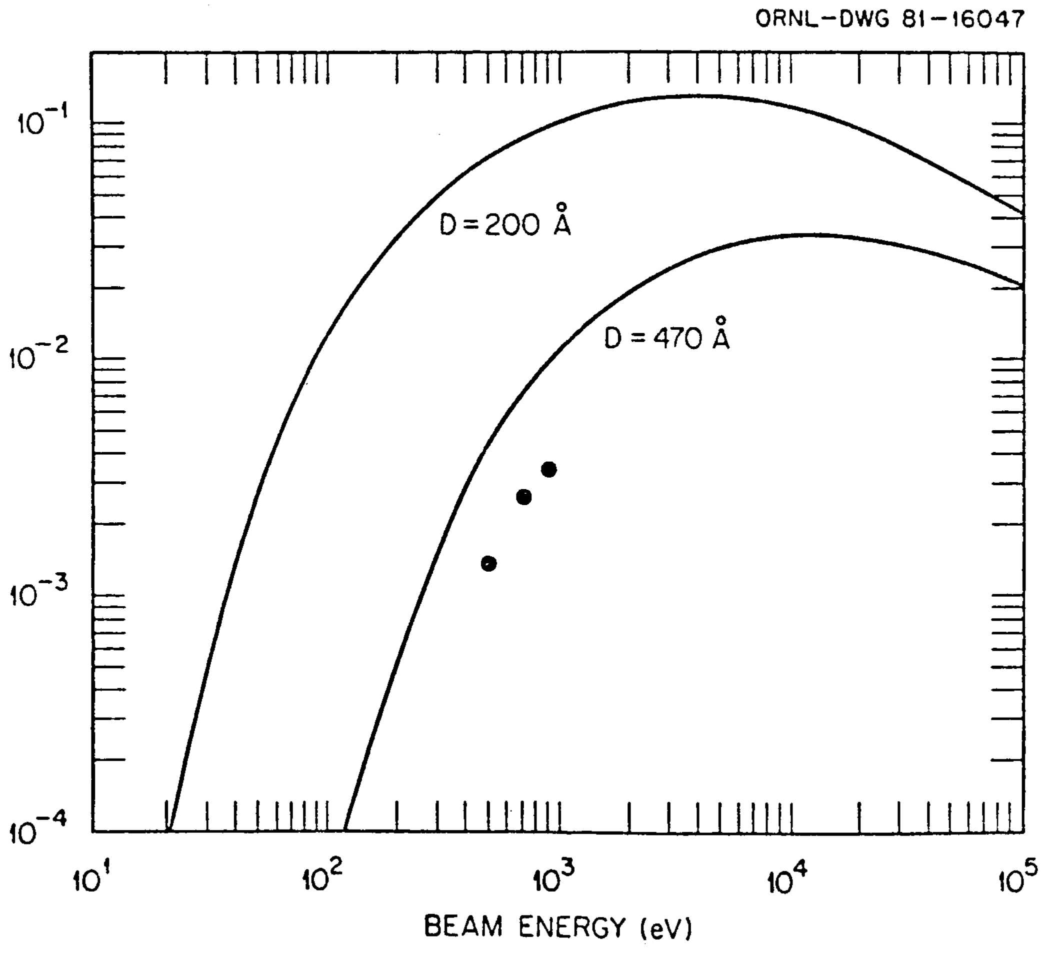

Figure 31. Surface Plasmon Production Probability for Charged Particles Translating above a Semi-Infinite Plane Slab Using Eq. (IV-10) with Channel Length of 1000 Å. The upper curve is for an equivalent cylinder diameter of 200 Å in silver, while the lower curve is for a 470 Å equivalent cylinder. The points correspond to the data in Table I.

with heights of 50 to 100 Å. It is felt that such roughness tends to trap particles approaching closer than 50 Å or to deflect them through a sufficient angle as to cause them to miss the detector, which was situated on the beam centerline.

V. SUMMARY

This work has investigated some aspects of the forces existing between macroscopic media and charged particles. To this end, the trajectories of electrons translating, under the influence of the electrical image force, near surfaces in geometries described by plane slabs and infinite cylindrical voids were discussed in Chapter II. The classical stopping power due to the nonconservative component of the image force for a charge translating close to dielectric media in these geometries was also calculated and shown to be proportional to the damping or relaxation time of the conduction electron gas in the media and to be exponentially proportional to the particle energy for velocities much less than that of light.

Since the image force between charges and dielectrics can be described in terms of excitations and decays of virtual modes in the surface plasmon field, the surface plasmon dispersion relation, in the low velocity limit, was calculated for geometries described by a single-sheeted hyperboloidal hole in a dielectric. For small-opening angles of the hyperboloid, the surface modes were shown to be entirely analogous to the longitudinal and tangential modes on a thin planar slab. In the limit that the surface curvature is much less than the plasmon wave vector, the surface plasmon frequency, ω_{sp}, was shown to converse on the planar limit of $\omega_p/\sqrt{2}$.

In Chapter III an experiment designed to probe the vacuum field of the surface plasmons was described. A thin silver foil containing thousands of small microchannels was bombarded by a thermally broadened electron beam of energy 100 to 900 eV; the beam emerging from the channels was then analyzed by an energy dispersive detector, and the surface plasmon transition probability as a function of incident energy was measured.

For electron energies of 500 to 900 eV, the surface plasmon production probability was found to increase with increasing beam energy, ranging from 1.4×10^{-3} at 500 eV to 3×10^{-3} at 900 eV. These results were compared to the classical stopping powers of Chapter II for cylinders and slabs and to a recent quantum mechanical calculation for a planar slab with the dielectric response of an ideal electron gas. It was found that the measured probabilities agreed well with planar cross sections, both classical and quantum, but were only 20 percent or so of the predicted probabilities for cylindrical voids in silver. This disparity between the cylindrical calculations and measurements was attributed to the lack of control in the foil fabrication process, producing an effective length of 20 to 25 percent of the foil thickness. The surface plasmon loss peak was measured as 3.5 eV, somewhat lower than the accepted value of 3.63 eV. This disparity was ascribed to surface contamination.

Further work could well proceed along two major lines. Since the low-velocity-dispersion relation for hyperboloids predicts a rapidly changing frequency for the low-order modes ($m = 0, 1$), an investigation of the loss energy as a function of channel-length-to-width ratio would provide evidence for the strong geometric dependence of the surface plasmon energy. Such a study would entail an increased sophistication in the fabrication of the channels. Another investigation could well probe the surface plasmon cross section as a function of electron beam energy and channel width, down to perhaps 100 Å. Quantum mechanical calculations indicate a maximum aloof transition rate at a beam energy of 12 keV for silver, while both classical and quantum models indicate an exponential dependence of the transition rate on impact parameters sufficiently close to the surface such that single-particle and hydrodynamic effects could be expected to rival the longer range collective effects.

"Better is the end of a thing than the beginning thereof."--Ecclesiastes.

LIST OF REFERENCES

LIST OF REFERENCES

Abramowitz, M., and I. A. Stegun, *Handbook of Mathematical Functions with Formulas, Graphs, and Mathematical Tables* (U. S. Government Printing Office, Washington, 1970) pp. 336-338.

Allen, J. D., Jr., J. D. Durham, G. K. Schweitzer and W. E. Deeds, *J. Electron Spectros. Related Phenom.* 8, 395-410 (1976).

Arfken, G., *Mathematical Methods for Physicists* (Academic Press, New York, 1970) p. 112.

Ashley, J. C., and L. C. Emerson, *Surf. Sci.* 41, 615-618 (1974).

Becker, R. S., V. E. Anderson, J. D. Allen, Jr., R. D. Birkhoff and T. L. Ferrell, *J. Aerosol Sci.* 11, 461 (1980).

Becker, R. S., V. E. Anderson, R. D. Birkhoff, T. L. Ferrell and R. H. Ritchie, *Can. J. Phys.* 59, 521 (1981).

Becker, R. S., T. L. Ferrell, H. H. Hubbell, Jr., and R. D. Birkhoff, submitted for publication to *The Physical Review B15*.

Birkhoff, R. D., J. D. Allen, Jr., V. E. Anderson, H. H. Hubbell, Jr., R. S. Becker, T. L. Ferrell and D. P. Spears, *Optik* 55(2), 157 (1980).

Bohm, D., and D. Pines, *Phys. Rev.* 82, 625 (1951).

Boye, D., *Drilling of Micron-Size Holes by Laser Pulses*, UCCND internal report, 1979.

Bronshtein, J. N., I. L. Krainskii and B. N. Libenson, *Sov. Phys.-Solid State* 19(4), 558 (1977).

Buchholz, H., *Z. Angew. Math. Mech.* 27, 245 (1947).

Durand, E., *Electrostatique, Tome I, II, and III* (Masson et Cie, Paris, (1964).

Ehrenreich, H., *IEEE Spectrum* 162 (March 1965).

Ferrell, T. L., Private communication (1978).

Ferrell, T. L., P. M. Echenique and R. H. Ritchie, *Solid State Commun.* 32, 419 (1979).

Ferrell, T. L., Private communication (1981).

Hageman, H. J., W. Gudat and C. Kunz, *Optical Constants from the Far Infrared to the X-Ray Region*, DESY Report SR-74/7, 1974.

Hobson, E. W., *The Theory of Spherical and Ellipsoidal Harmonics* (Chelsea Press, New York, 1965).

Kunz, C., and H. Raether, *Solid State Commun.* 1, 214 (1963).

Kunz, C., Z. *Phys.* 196, 311 (1966).

Lecante, J., Y. Ballu and D. M. Newns, *Phys. Rev. Lett.* 38, 366 (1977).

Little, J. W., T. A. Callcott and E. T. Arakawa, *Rev. Sci. Instrum.* 51, 1581 (1980).

Morse, P. M., and H. Feschbach, *Methods of Theoretical Physics* (McGraw-Hill, New York, 1953).

Otto, A., *Phys. Status Solidi* 22, 401 (1967).

Powell, C. J., and J. B. Swan, *Phys. Rev.* 115, 869 (1959).

Powell, C. J., and J. B. Swan, *Phys. Rev.* 116, 816 (1959).

Powell, C. J., and J. B. Swan, *Phys. Rev.* 118, 640 (1960).

Raether, H., "Solid State Excitations by Electrons," in *Springer Tracts in Modern Physics* (Springer-Verlag, Berlin-New York, 1965), vol. 38.

Rahman, T. S., and A. A. Maradudin, *Phys. Rev.* B 21, 504 (1980).

Ritchie, R. H., *Phys. Rev.* 106, 874 (1957).

Ritchie, R. H., and H. B. Eldridge, *Phys. Rev.* 126, 1935 (1962).

Ritchie, R. H., F. W. Garber, M. Y. Nakai, and R. D. Birkhoff, "Low Energy Electron Mean Free Paths in Solids," in *Advances in Radiation Biology* (Academic Press, Inc., New York, 1968).

Ritchie, R. H., *Phys. Lett.* 38A, 189 (1972).

Rudford, E., *Proc. R. Soc. Lond.* A127, 111 (1930).

Ruthmann, C., *Ann. Phys.* 2, 133 (1948).

Shank, C. V., and R. V. Schmidt, *Appl. Phys. Lett.* 23, 154 (1973).

Siegbahn, K. S., *Nova Actae Regia Soc. Sci. Upsaliensis* 20, 198 (1967).

Smythe, W. R., *Static and Dynamic Electricity* (McGraw-Hill, New York, 1968) 3rd ed.

Snow, C. P., *The Hypergeometric and Legendre Functions with Applications to Integral Equations of Potential Theory* (U. S. Department of Commerce, National Bureau of Standards, Washington, 1952).

Spears, D. P., J. D. Allen, Jr., V. E. Anderson, R. S. Becker, H. H. Hubbell, Jr., T. L. Ferrell, R. H. Ritchie and R. D. Birkhoff, *J. Appl. Phys.* 50, 3031 (1979).

Stern, E. A., and R. A. Ferrell, *Phys. Rev.* 120, 130 (1960).

Warmack, R. J., J. A. Stockdale and R. N. Compton, *Int. J. Mass. Spectros. Ion Phys.* 27, 239 (1978).

Yu, C. P., and K. Chandra, *J. Aerosol Sci.* 9, 175 (1978).

Zacharias, P., *Z. Phys.* 238, 172 (1970).

Ziman, J. M., *The Theory of Solids* (Cambridge Univ. Press, 1972).

APPENDIX

APPENDIX

It is of interest to relate the Legendre functions $\underline{P}^m_{-\frac{1}{2}+\mu}$ to Snow's functions $T^m_{-\frac{1}{2}+\mu}$. Snow defines the T functions as:

$$T^m_{\mu-\frac{1}{2}}(\cos\theta) = \frac{\Gamma(\frac{1}{2} + m + \mu)}{\Gamma(\frac{1}{2} - m + \mu)} \frac{\tan^m \frac{\theta}{2}}{m!} \; {}_2F_1\left(\tfrac{1}{2} + \mu, \tfrac{1}{2} - \mu, m + 1; \sin^2 \frac{\theta}{2}\right) .$$

For calculational purposes this can be expanded, using the hypergeometric Gauss series as:

$$ {}_2F_1 = \frac{\Gamma(m + 1)}{T(\frac{1}{2} + \mu)\; T(\frac{1}{2} - \mu)} \sum_{n=0}^{\infty} \frac{\Gamma(\frac{1}{2} + \mu + n)\; \Gamma(\frac{1}{2} - \mu + n)}{\Gamma(m + n + 1)\; n!} \sin^{2n} \frac{\theta}{2} .$$

The gamma functions are expanded:

$$\Gamma(n + \tfrac{1}{2} + \mu) = (n - \tfrac{1}{2} + \mu)(n - 3/2 + \mu) \;\text{---}\; (\tfrac{1}{2} + \mu)\; T(\tfrac{1}{2} + \mu)$$

$$\Gamma(n + \tfrac{1}{2} - \mu) = (n - \tfrac{1}{2} - \mu)(n - 3/2 - \mu) \;\text{---}\; (\tfrac{1}{2} - \mu)\; T(\tfrac{1}{2} - \mu)$$

$$\Gamma(m + n + 1) = (m + n)\; (m + n - 1) \;\text{---}\; (m + 1)\; T(m + 1) .$$

Rewriting in terms of product functions, the $T^m_{-\frac{1}{2}+\mu}$ are:

$$T^m_{-\frac{1}{2}+\mu}(\cos\theta) = \frac{\Gamma(\frac{1}{2} + m + \mu)}{\Gamma(\frac{1}{2} - m + \mu)} \frac{\tan^m \frac{\theta}{2}}{m!} \sum_{n=0}^{\infty} \prod_{j=1}^{n} \left[\frac{(j - \frac{1}{2})^2 - \mu^2}{j(m + j)} \sin^2 \frac{\theta}{2}\right] .$$

From Abramowitz and Stegun, AS 8.1.2, the Legendre function

$$P^\mu_\nu(z) = \frac{1}{\Gamma(1 - \mu)} \left(\frac{z + 1}{z - 1}\right)^{\mu/2} {}_2F_1\left(-\nu, \nu + 1, 1 - \mu; \frac{1 - z}{2}\right)$$

expanded around the point $z = \frac{1}{2}$. If we take $z = \cos\theta$, then

$$\frac{1 - z}{2} = \sin^2 \frac{\theta}{2}, \left(\frac{z + 1}{z - 1}\right)^{\mu/2} = \tan^{-\mu} \frac{\theta}{2} (-1)^{-\mu/2} .$$

Letting ν be $-\frac{1}{2} + \mu$ and $\mu = -m$, the Legendre function of the first kind is:

$$P^{-m}_{-\frac{1}{2}+\mu}(\cos\theta) = \frac{1}{\Gamma(m + 1)} (-1)^{+m/2} \tan^m \frac{\theta}{2}$$

$$\times \; {}_2F_1 \left(\tfrac{1}{2} - \mu, \tfrac{1}{2} + \mu, m + 1; \sin^2 \frac{\theta}{2}\right).$$

From AS 9.2.5, the functions of negative order can be related to the functions of positive order.

$$P^{-m}_{-\frac{1}{2}+\mu}(X) = \frac{\Gamma(\frac{1}{2} + \mu - m)}{\Gamma(\frac{1}{2} + \mu + m)} P^{m}_{-\frac{1}{2}+\mu}(X) ,$$

and the $P^{m}_{-\frac{1}{2}+\mu}$ are given by:

$$P^{m}_{-\frac{1}{2}+\mu}(\cos\theta) = (-1)^{+m/2} \frac{\Gamma(\frac{1}{2} + \mu + m)}{\Gamma(\frac{1}{2} + \mu - m)} \frac{\tan^m \frac{\theta}{2}}{m'}$$

$$\times \; {}_2F_1 \left(\tfrac{1}{2} - \mu, \tfrac{1}{2} + \mu, m + 1; \sin^2 \frac{\theta}{2}\right).$$

Hence:

$$P^{m}_{-\frac{1}{2}+\mu}(\cos\theta) = e^{i(m\pi/4)} T^{m}_{-\frac{1}{2}+\mu}(\cos\theta) .$$

The Radial Functions $T^{\mu}_{m-\frac{1}{2}}$ and $P^{\mu}_{m-\frac{1}{2}}$

The radial functions can also be defined in a similar fashion as that for the angle functions. Snow gives, on page 312, a definition for the $T^{\mu}_{m-\frac{1}{2}}$:

$$T^{\mu}_{m-\frac{1}{2}}(\tanh\beta) = \frac{\Gamma(\frac{1}{2} + m + \mu)\; e^{-\mu\beta}}{\Gamma(\frac{1}{2} + m - \mu)\; \Gamma(\mu + 1)}$$

$$\times \; {}_2F_1\left(m + \tfrac{1}{2},\; \tfrac{1}{2} - m,\; 1 + \mu;\; \frac{1}{e^{2\beta} + 1}\right) .$$

Consider AS 8.1.2 again, using the same expansion and circle of convergence. We let z be given by $\tanh\beta$, and:

$$\frac{1 - z}{2} = \frac{1}{e^{2\beta} + 1}, \qquad \frac{z + 1}{z - 1} = -e^{2\beta} .$$

Then the Legendre function of the first kind can be written as:

$$P^{\mu}_{m-\frac{1}{2}}(\tanh\beta) = \frac{(-1)^{-\mu/2}}{\Gamma(i - \mu)}\; e^{\mu\beta}\; {}_2F_1\left(-\nu,\; \nu + 1,\; 1 - \mu;\; \frac{1}{e^{2\beta} + 1}\right)$$

and letting μ go to $-\mu$, we have for $\nu = m - \frac{1}{2}$:

$$P^{-\mu}_{m-\frac{1}{2}}(\tanh\beta) = \frac{(-1)^{-\mu/2}}{\Gamma(\mu + 1)}\; e^{-\mu\beta}\; {}_2F_1\left(\tfrac{1}{2} - m,\; \tfrac{1}{2} + m,\; 1 + \mu;\; \frac{1}{e^{2\beta} + 1}\right).$$

Looking at the expansion for $T^{\mu}_{m-\frac{1}{2}}$, we can say:

$$T^{\mu}_{m-\frac{1}{2}}(\tanh\beta) = \frac{\Gamma(\frac{1}{2} + m + \mu)}{\Gamma(\frac{1}{2} + m - \mu)}\; (-1)^{\mu/2}\; P^{-\mu}_{m-\frac{1}{2}}(\tanh\beta) .$$

Since μ is not restricted to be integral or real, we cannot say that $P_n^{-\mu}$ is proportional to P_ν^μ, but rather that the functions are independent, as are $P_\nu^m(-X)$, $P_\nu^m(+X)$ and $P_\nu^m(X)$, $Q_\nu^m(X)$.

The Functions $T^\mu_{m-\frac{1}{2}}$, $P^{-\mu}_{m-\frac{1}{2}}$, C^μ_m, and S^μ_m

From previous derivations we can define the even and odd parts of the radial solutions by taking sums and differences as

$$T^\mu_{m-\frac{1}{2}}(\tanh\beta) \pm T^\mu_{m-\frac{1}{2}}(-\tanh\beta) .$$

Snow defines the sum to be the function $C^\mu_m(\tanh\beta)$ and the difference to be $S^\mu_m(\tanh\beta)$. The Legendre functions of the first kind can then be formed into even and odd parity solutions:

$$T^\mu_{m-\frac{1}{2}}(\tanh\beta) \pm T^\mu_{m-\frac{1}{2}}(-\tanh\beta) = \frac{\Gamma(m + \frac{1}{2} + \mu)}{\Gamma(m + \frac{1}{2} - \mu)} (-1)^{\mu/2}$$
$$\times \left[P^{-\mu}_{m-\frac{1}{2}}(\tanh\beta) \pm P^{-\mu}_{m-\frac{1}{2}}(-\tanh\beta)\right] ,$$

where

$$C^\mu_m = \frac{2^{\mu-1}}{\pi^{3\mu}} \cos(\mu - m)\pi \; e^{-\mu \ln(\cosh\beta)} \; \Gamma\left(\frac{1}{4} + \frac{m}{2} + \frac{\mu}{2}\right) \Gamma\left(\frac{1}{4} - \frac{m}{2} + \frac{\mu}{2}\right)$$
$$\times \; {}_2F_1\left(\frac{1}{4} + \frac{m}{2} + \frac{\mu}{2} , \frac{1}{4} - \frac{m}{2} + \frac{\mu}{2} , \frac{1}{2} ; \tanh^2\beta\right)$$

and

$$S_m^\mu = \frac{2^\mu}{\pi^{3/2}} \cos(\mu - m)\pi \; e^{-\mu \ln(\cosh\beta)} \tanh\beta \; \Gamma\left(\frac{3}{4} + \frac{m}{2} + \frac{\mu}{2}\right)$$

$$\times \; \Gamma\left(\frac{3}{4} - \frac{m}{2} + \frac{\mu}{2}\right) {}_2F_1\left(\frac{3}{4} + \frac{m}{2} + \frac{\mu}{2}\,,\; \frac{3}{4} - \frac{m}{2} + \frac{\mu}{2}\,,\; \frac{3}{2}\,;\; \tanh^2\beta\right) .$$

From these definitions, it can be immediately seen that C_m^μ is even in β and S_m^μ is odd in β. Using these quantities as source terms in the potential expansion, the oscillator products can be expressed in terms of even and odd parity solutions.

Relations Between $Q^m_{-\frac{1}{2}+\mu}$ and C_m^μ and S_m^μ

Using AS 8.2.7, the Legendre functions of the second kind are expressed in terms of the Legendre functions of the first kind by:

$$Q_\nu^\mu(z) = \left(\frac{\mu}{2}\right)^{\frac{1}{2}} \Gamma(\nu + \mu + 1) \; (z^2 - 1)^{-\frac{1}{4}} \; e^{i\mu\pi} \; P^{-\nu-\frac{1}{2}}_{-\mu-\frac{1}{2}}\left(\frac{z}{(z^2 - 1)^{\frac{1}{2}}}\right)$$

Let $z = i\sinh\beta$, $\nu = -\frac{1}{2} + \mu$, $\mu = m$; then

$$\frac{z}{\sqrt{z^2 - 1}} = \tanh\beta$$

and

$$Q^m_{-\frac{1}{2}+\mu}(i\sinh\beta) = \frac{\pi}{\sqrt{2}\,\cosh\beta} \; \Gamma(\tfrac{1}{2} + m + \mu) \; e^{i\pi(m-\frac{1}{4})} \; P^{-\mu}_{m-\frac{1}{2}}(\tanh\beta)$$

using

$$P_\nu^\mu(z) = P^\mu_{-\nu-1}(z) .$$

Inspecting the $T^{\mu}_{m-\frac{1}{2}}$ we can say:

$$Q^{m}_{-\frac{1}{2}+\mu}(i\sinh\beta) = \sqrt{\frac{\pi}{2\cosh\beta}}\ \Gamma(\tfrac{1}{2}+m-\mu)(-1)^{-\mu/2}(-1)^{m}$$

$$\times\ e^{-i(\pi/4)}\ T^{\mu}_{m-\frac{1}{2}}(\tanh\beta)$$

and the even and odd solutions in β are given by:

$$Q^{m}_{-\frac{1}{2}+\mu}(i\sinh\beta) + Q^{m}_{-\frac{1}{2}+\mu}(-i\sinh\beta) = \sqrt{\frac{\pi}{2\cosh\beta}}\ \Gamma(\tfrac{1}{2}+m+\mu)$$

$$\times\ (-1)^{-\mu/2}\ (-1)^{m}\ e^{-i(\pi/4)}\ C^{\mu}_{m}(\tanh\beta)$$

and

$$Q^{m}_{-\frac{1}{2}+\mu}(i\sinh\beta) - Q^{m}_{-\frac{1}{2}+\mu}(-i\sinh\beta) = \sqrt{\frac{\pi}{2\cosh\beta}}\ \Gamma(\tfrac{1}{2}+m+\mu)$$

$$\times\ (-1)^{-\mu/2}\ (-1)^{m}\ e^{-i(\pi/4)}\ S^{\mu}_{m}(\tanh\beta)\ .$$

It is of interest to note that the Legendre functions of the second kind incorporate the radial damping term $1/\sqrt{\cosh\beta}$ and can be considered to be the complete radial solution.

Relations Between the $P^{\mu'}_{m-\frac{1}{2}}(i\cot\theta)$ and $P^{m}_{-\frac{1}{2}+\mu'}(\pm\cos\theta)$

In Abramowitz and Stegun there are two expressions that can be used to convert the function of argument $i\cot\theta$ to $\pm\cos\theta$.

A&S 8.2.7

$$P^{-\nu-\frac{1}{2}}_{-\mu-\frac{1}{2}}\left(\frac{z}{\sqrt{z^2-1}}\right) = \frac{(z^2-1)^{\frac{1}{4}}\,e^{-i\mu\pi}}{\sqrt{\pi/2}\;\Gamma(\nu+\mu+1)}\,Q^{\mu}_{\nu}(z), \qquad Rz > 0$$

A&S 8.2.3

$$Q^{\mu}_{\nu}(z) = \frac{\pi/2\;e^{i\mu\pi}}{\sin[(\nu+\mu)\pi]}\left[e^{\pm i\nu\pi}\,P^{\mu}_{\nu}(z) - P^{\mu}_{\nu}(-z)\right]$$

Let $z = \cos\theta$ where $0 \leq \theta \leq \pi/2$. Then

$$\frac{z}{\sqrt{z^2-1}} = \pm i\cot\theta \geq i\cot\theta$$

since the D.E. is independent of sign. Let

$$\nu + 1/2 = -\mu' \qquad \text{and} \qquad \mu + 1/2 = -1/2 - m$$

$$\nu = -1/2 - \mu' \qquad\qquad \mu = -m\,.$$

Then

$$P^{\mu'}_{m-\frac{1}{2}}(i\cot\theta) = \frac{\sqrt{\sin\theta}\;e^{i(\pi/4)}\,e^{+im\pi}}{\sqrt{\pi/2}\;\Gamma(-\frac{1}{2}-\mu'-m)}\,Q^{-m}_{-\frac{1}{2}-m'}(\cos\theta)\,.$$

Using AS 8.2.3 we have

$$Q^{-m}_{-\frac{1}{2}-\mu'}(\cos\theta) = \frac{\pi/2\;e^{-im\pi}}{\sin[\pi(-m-\frac{1}{2}-\mu')]}\left[e^{\pm i\pi(-\frac{1}{2}-\mu')}\right.$$

$$\left.\times\; P^{-m}_{-\frac{1}{2}-\mu'}(\cos\theta) - P^{-m}_{-\frac{1}{2}-\mu'}(-\cos\theta)\right].$$

Using As 8.2.5 relating P-funtions of positive to negative codes, the integer order

$$P^{-m}_{-\frac{1}{2}-\mu'}(x) = \frac{\Gamma(\frac{1}{2} - \mu' + m)}{\Gamma(\frac{1}{2} - \mu' - m)} P^{m}_{-\frac{1}{2}-\mu'}(x)$$

$$\therefore P^{\mu'}_{m-\frac{1}{2}}(i\cot\theta) = \sqrt{\sin\theta} \frac{\sqrt{\pi/2}\, e^{i(\pi/4)} (-1)^{m+1}}{\Gamma(-\frac{1}{2} - \mu - m) \cos(\mu'\pi)} \frac{\Gamma(\frac{1}{2} - \mu' + m)}{\Gamma(\frac{1}{2} - \mu' - m)}$$

$$\times e^{\pm i\pi(\mu'+\frac{1}{2})} P^{m}_{-\frac{1}{2}-\mu'}(\cos\theta) - P^{m}_{-\frac{1}{2}-\mu'}(-\cos\theta)$$

$$= \tilde{C} \sqrt{\sin\theta} \left[e^{\pm i\pi(\mu'+\frac{1}{2})} P^{m}_{-\frac{1}{2}-\mu'}(\cos\theta) - P^{m}_{-\frac{1}{2}-\mu'}(-\cos\theta) \right] .$$

From Hobson, page 445,

$$P_{-\frac{1}{2}+ik}(\cos\theta) = 1 + \sum_{n=1}^{\infty} \left\{ \prod_{m=1}^{n} \left[\frac{4k^2 + (2m+1)^2}{(2m)^2} \right] \right\} \sin^{2n} \frac{\theta}{2}$$

$$P_{-\frac{1}{2}+ik}(-\cos\theta) = 1 + \sum_{n-1}^{\infty} \left\{ \prod_{m-1}^{n} \left[\frac{4k^2 + (2m+1)^2}{(2m)^2} \right] \right\} \cos^{2n} \frac{\theta}{2} .$$

Hence, the $\underline{P^{\mu}_{m-\frac{1}{2}}}(i\cot\theta)$ for two linearly independent solutions are $0 \leq \theta \leq \pi/2$.

VITA

Russell Scott Becker was born on June 16, 1953, in Corpus Christi, Texas. He attended the public and parochial schools there, graduating from Mary Carroll High School in June 1971.

He received an Associate of Arts degree in Physics from Del Mar College, Corpus Christi, Texas, in May 1973 and a Bachelor of Science degree in Physics from Texas A&M in May of 1975.

He enrolled in the graduate program of The University of Tennessee at Knoxville in September 1975 and received the degree of Doctor of Philosophy in March of 1982 for investigations carried out in the field of surface physics.